Modeling and Optimization of Power Management and Li-ion Batteries Health for Hydraulic-Electric Hybrid Vehicle

by

Xianke Lin

A dissertation submitted in partial fulfillment
of the requirements for the degree of
Doctor of Philosophy
(Mechanical Engineering)
in The University of Michigan
2014

Doctoral Committee:

Professor Wei Lu, Chair
Professor Margaret Wooldridge
Assistant Professor Bart Bartlett
Associate Professor Christian Lastoskie

If we knew what we were doing, it wouldn't be called research.

-Albert Einstein

Here’s to the crazy ones, the rebels, the troublemakers, the ones who see things differently. While some may see them as the crazy ones, we see genius. Because the people who are crazy enough to think they can change the world, are the ones who do.

– Steve Jobs

Acknowledgments

First and foremost, I sincerely thank Prof. Wei Lu, my advisor and committee chair, for giving me the opportunity to work on the fascinating and challenging research. His unlimited support, instruction, and encouragement are deeply appreciated. In particular, Prof. Lu has a unique ability to connect concepts to the big picture, and recommend creative topics for my research. These skills kept me on track through the research.

I am extremely thankful to my committee members, Prof. Margaret Wooldridge, Prof. Bart Bartlett and Prof. Christian Lastoskie, for asking inspiring questions and providing critical feedback. Their insightful advice has been crucial toward creating a solid foundation for the work presented in this dissertation.

Several colleagues deserve special recognition for their mentorship and friendship during my doctoral studies. I would like to thank Dr. Andrej Ivanco for helping me explore my potential and unceasing support and encouragement to my research, Dr. Lin Liu for his endless knowledge on experiments and simulation, Dr. Xiaoguang Hao for tips on TEM and SEM instruments, and Guangyu Liu for helps on the experiments. I would also like to my colleagues from the GM/UM Advanced Battery Coalition for Drivetrains for their support over the years and the congenial environment they created.

Finally, none of this would have been possible without the love and support of my family, whom I cannot possibly thank enough. They have always been my true source of inspiration and perspective.

The author would like to acknowledge the support provided by the U.S. Department of Energy and General Motor.

Table of Contents

List of Tables

List of Figures

List of Appendices

Abstract

The main goal of this work is to develop a systematic methodology to improve the range of electric vehicle and protect the battery health. Several other objectives enable achieving the main goal, including modeling, and power management optimization of hydraulic electric hybrid system, and battery degradation investigation and optimization.

In order to improve the electric vehicle range, the hydraulic hybridization of electric vehicle is proposed. Physics based models of hydraulic electric hybrid vehicle are developed and the performance is analyzed. A near optimal and vehicle implementable rule-based energy management strategy is developed for the hydraulic-electric hybrid vehicle. To further improve the range, the battery health is identified to be the key issue. Electrochemistry-based battery models are developed to investigate the degradation of the graphite/$LiMn_2O_4$ cell. This topic is motivated by the need to enhance the performance and longevity of lithium ion cells in the electric vehicle systems. In particular, the long cycle life is critical for the transportation electrification. Later, this dissertation elucidates the key degradation mechanisms in the lithium ion cells which enable opportunities to improve battery performance and health through optimal design. The whole topic is addressed in three steps.

Firstly, we propose hydraulic hybridization of electric vehicle and develop a physics based model for hydraulic-electric hybrid vehicle. In order to improve the range, power management optimization is conducted to determine the optimal control strategy for the hybrid vehicle. The all electric range is improved by 68.3% through hybridization and control optimization.

Secondly, battery health is another key issue for transportation electrification. In order to improve the battery health, we develop mathematical models for the key side reactions, and couple these side reactions to Newman's backbone model to form a degradation model. A three electrode cell is fabricated and cycled over long term to provide physical support for the modeling framework. Our degradation study shows that the capacity fade can be divided into three stages: acceleration stage (SEI growth on anode is dominant), stabilization stage (SEI growth slows down and cathode capacity fade continues), and saturation stage (cathode has poor capacity and becomes the limiting factor). Long term cycled electrodes are examined by SEM and TEM. Cathode LMO fracture is repeatedly observed and suspected to be one important degradation mechanism in the cathode. A single particle fracture model is developed to investigate capacity fade induced by cathode fracture. The study shows that fracture introduces a significant capacity loss. In a 5 um particle with fracture, the capacity loss can reach to 13.7%. The particle size is another key factor that affects the mass transportation in the particle. Larger particles lead to higher internal resistance for electron transportation; therefore, fracture-induced capacity fade is more severe than with particles of smaller size.

In the final phase, a general procedure is developed to optimize the battery health while fulfilling the energy and power requirements. The study investigates the impact of battery parameters on the battery performance, such as energy density, power density and battery health.

In total, this dissertation provides a systematic way to improve the range of electric vehicle by hydraulic hybridization and battery optimal design. The results provide insights into the effects of the hybridization on the electric vehicle performance, and also the battery parameters on the battery degradation. The methodologies developed in this dissertation can be used to

provide guidance for development of strategies for hybrid propulsion and optimal design of the battery health.

Chapter 1
Introduction

The energy economy based on fossil fuels is at a serious risk due to several factors, such as, the energy insecurity dependent on unstable import oil, and depletion of non-renewable resource[1-3]. The access to the stable energy has becomes essential to the functioning of modern economies. Deployment of renewable energy and energy efficiency, and diversification of energy sources, would bring significant energy security and economic benefits[4]. Another adverse effect of the current energy economy is the climate change. The greenhouse gases emitted from fossil fuel burning traps heat and make the planet warmer[5]. CO_2 is the primary greenhouse gas emitted from human activities and accounted for about 84% of all U.S. greenhouse gas emissions in 2011[6]. The main source of CO_2 is the combustion of fossil fuels for energy and transportation[7]. There is an urgent need to address the energy security, and climate change, which requires the use of clean energy. Transportation electrification, such as, electric vehicles (EV), can replace petroleum with renewable energy sources, and reduce the CO_2 emission, therefore helps address the energy and environmental issues. Although electric vehicles are appealing for environmental and energy security reasons, the efficiency of these electric vehicles has been known to drop from 90% to 60% during low speed or high torque [8]. High current draw during operation will also damage the battery system, and reduce the battery life[9]. One of the solutions to overcome such challenge is the hybridization of electric vehicles. Hybrid vehicles use secondary energy storage, such as, hydraulic accumulator, and a secondary power device, such as, hydraulic pump/motor. Efficient power management of the secondary

power devices provides an additional degree of freedom to operate the electric motor and battery system. However, the vehicle system becomes more complicated when it is hybridized. In this study, the potential of the hydraulic electric hybrid will be evaluated and the power management strategy will be developed.

Besides electric vehicle hybridization, long cycle life battery system is urgently needed to support the aggressive vehicle electrification. Batteries, as the energy storage system, play a crucial role in the renewable energy systems, such as wind power, solar power and transportation electrification, etc., as shown in Figure 1.1. It not only provides the energy storage for the electrified transportation, but also mitigates the intermittency of the renewable energy generation, such as wind, and solar power.

As more and more renewables come online, large scale and high efficient batteries have become more and more attractive as an energy storage option. Many different battery systems exist in the market. Figure 1.2 shows the comparison of several key battery systems[10]. It is shown that Li-ion batteries have superior specific energy and high power density. Due to the high specific energy, high efficiency, high power density, and the stable cycling performance[1], LIBs are expected to find a prominent role in the energy storage system.

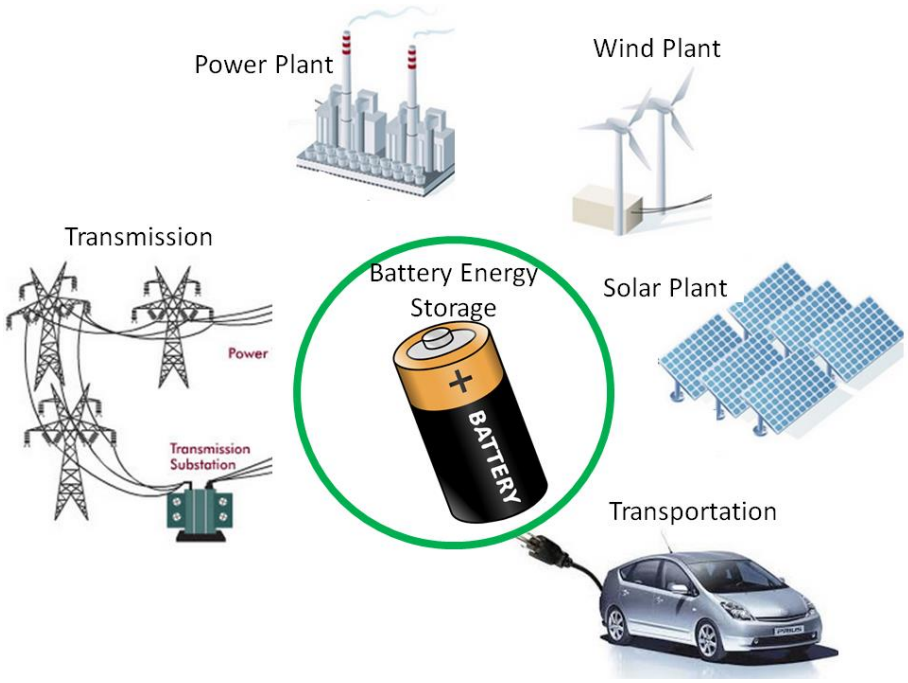

Figure 1.1 Battery's role in the energy infrastructure

Since the first commercialization by Sony in 1991, Lithium ion batteries (LIBs) have been widely used as portable power sources for consumer electronics. The growth of EV and HEV will also require the development of high performance of Li-ion batteries. However, problems of various natures of lithium ion batteries still prevent the large scale introduction of electric vehicles. One drawback of the current Li-ion technology for the automotive application is their limited cycle life. A number of causes are postulated to contribute to the capacity degradation [11-13]. Due to the complexity of the battery system, the degradation mechanisms in the Li-ion batteries remain poorly understood.

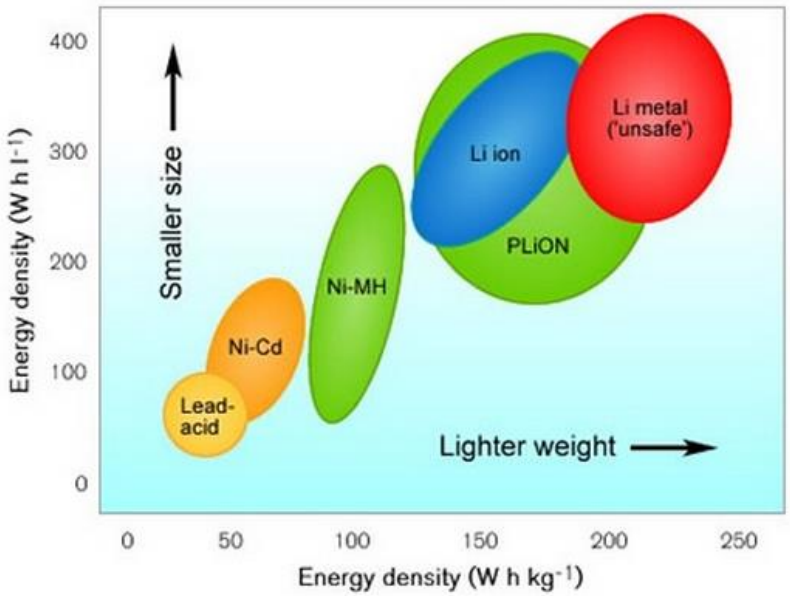

Figure 1.2 Distribution of the different electrochemical systems according to their gravimetric/volumetric energy densities [10].

In order to improve the battery design, especially the battery lifetime, this dissertation introduces innovative approaches for multiphysics/multiscale modeling, problem formation, and analysis. These approaches are applied to investigate the major degradation mechanisms in the Li-ion batteries to study the long term degradation patterns. The framework presented here integrates different degradation mechanisms together, and provides a deeper understanding of their interactions. Physical/mathematical models are developed to quantitatively study the impact of each degradation mechanism on the overall battery performance. The results reveal the dynamic evolution of the battery degradation process. Through the insight provided by the degradation analysis, potential opportunities for cycle life improvement are identified. The proposed optimal design based on degradation analysis has the potential to increase battery cycle life.

The remainder of the induction section is organized in the following five parts. First, the big picture of the research background is explained and the motivation of this dissertation is

presented. Second, a literature review is conducted, and the performance of the electric vehicle, hydraulic system and the main battery degradation mechanisms are introduced. Third, the potential challenges are identified. Forth, the contributions of this dissertation are summarized. Fifth, the dissertation organization is outlined.

1.1 Research Objective and Motivation

The main objective of this dissertation is to develop a methodology to improve the range of electric vehicle and protect the battery health. The study demonstrates the benefits of hydraulic hybridization of electric vehicle and its effects on the vehicle range and battery health. After the power management optimization, battery is identified to be the key component in the vehicle electrification. Lithium ion batteries are energy storage systems that can draw energy from the electric grid and provide propulsive energy for transportation. This functional change allows a hybrid vehicle to displace petroleum energy with multi-source electric energy. This also provides the opportunities to reduce the greenhouse gas emissions from the transportation system. However, the battery energy storage system is the weakest part in achieving this goal due to the limited lifetime. Therefore, the battery typically has to be oversized in order to meet the lifetime requirement[14], which makes the system expensive. This also provides a strong impetus for investigating the battery degradation and extending the battery lifetime.

One of the objectives of this dissertation is to develop techniques for battery cycle life improvement. The importance of this topic is not only motivated by the vision of future renewable energy infrastructure as shown in Figure 1.1, but also by the rapid growth of renewable energy all over the world as shown in Figure 1.3. In the future, renewable energy will potentially present a significant portion of the energy portfolio. In the long term, different

country is implementing technologies to increase the renewable energy productions. The policy targets for several countries over the world are included in Table 1.1.

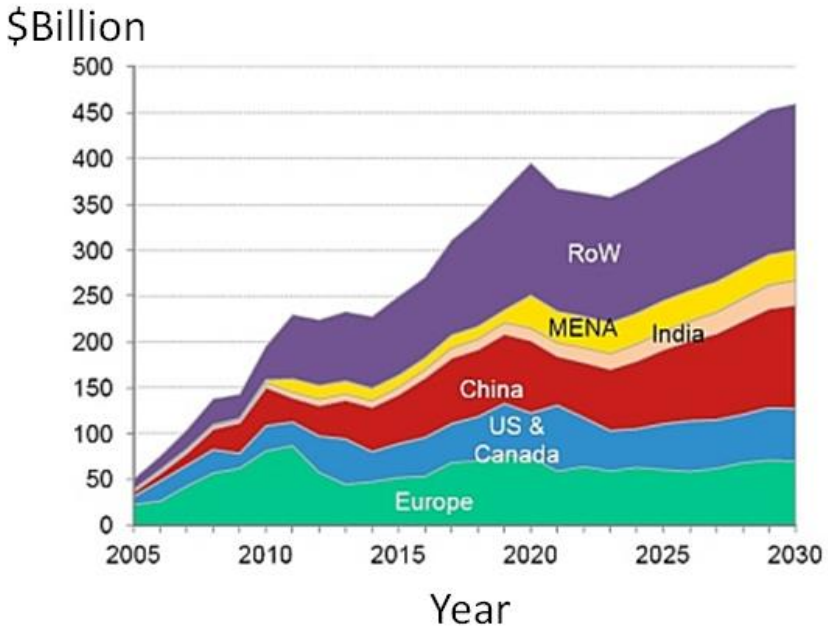

Figure 1.3 Annual Value of Renewable Energy Capacity Installed
(MENA=Middle East North Africa; RoW=Rest of the World)[15]

Due to the intermittent nature of the renewable energy sources such as, wind, solar, and tidal power, a large scale and long lifetime battery storage system is in need. A battery energy storage system is one of the critical enabling technologies to realize the future renewable energy infrastructure.

Table 1.1 Renewable Energy Targets by Country [16]

Country	**Amount (of total energy)**	**Deadline**
Australia	20%	2020
China	15%	2020
Egypt	12%	2020
European Union	20%	2020
Japan	10%	2020

In this dissertation we focus on power management optimization of the hydraulic electric hybrid vehicle to improve the range, and furthermore, we carry out optimal design of battery health to improve the battery cycle life. This research investigated the impact of different control strategies on the vehicle performance, and also the impact of battery parameters on the battery cycle life. The methodology developed in this dissertation provides design guidelines for improving the electric vehicle efficiency, extending all-electric range, and optimizing battery life therefore reduces the long term replacement costs of the expensive high capacity battery packs.

1.2 Literature Review

1.2.1 Hydraulic Hybridization

Hydraulics is a mature technology, and has been widely used in construction machinery. The hydraulic hybrid propulsion system uses fluid power to propel the powertrain. Of many hybridization options, the hydraulic hybrid has many advantages for heavy duty vehicles due to its high power density and energy conversion efficiency. The hydraulic accumulator stores high power energy via highly compressed gas like a pneumatic spring. The accumulator has higher power density compared to battery systems[17]. Thus, hydraulic accumulator is very suitable for capturing high power energy, such as, regenerative braking, and also suitable for outputting high power energy during acceleration. Due to the relatively slow chemical reaction rates, battery provides much less charge and discharge rate compared with hydraulic accumulator. Figure 1.4 shows the common energy storage system. The power density of hydraulic accumulator is more than 10 times higher than batteries[18]. However, the low energy density is the drawback of hydraulic accumulator. Therefore, combining the battery system and hydraulic accumulator

enables us to meet both high power demand and low power demand. Optimal management of battery energy and hydraulic energy in the hybrid vehicle becomes a very important issue.

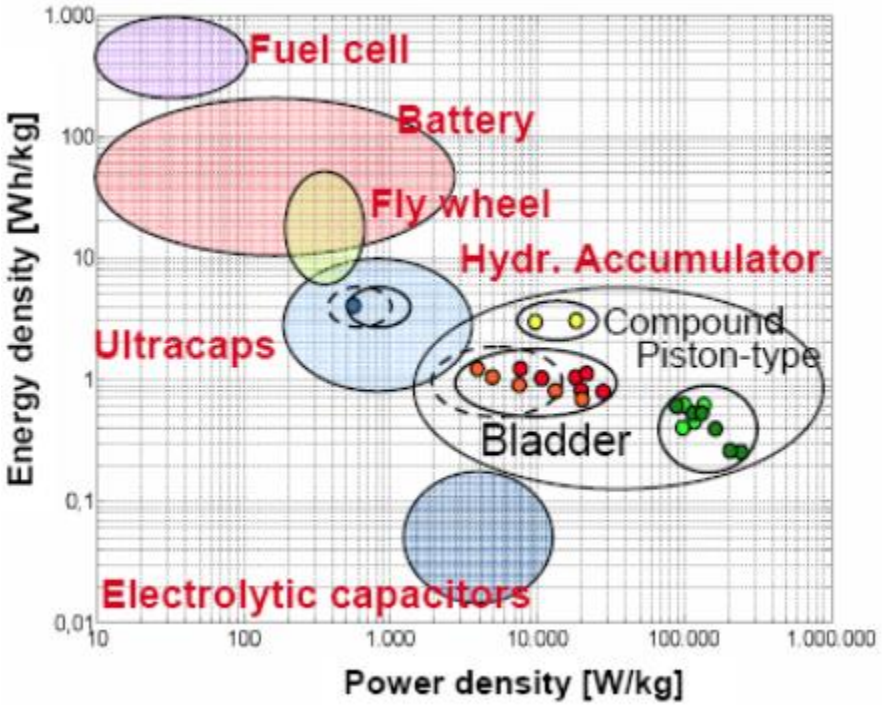

Figure 1.4 Energy vs. power density of different energy storage systems[18, 19]

A hydraulic pump/motor (P/M) can be used as the secondary power device in the hybridization of electric vehicle. The hydraulic pump/motor is used as a pump when it pumps the fluid from reservoir to the accumulator. It's used as a motor when the high pressure fluid from the accumulator flows out to the reservoir. The displacement of the PM can be changed continuously, which gives a continuous change of output torque. The efficiency of the hydraulic system is reported as high as 82% as shown in Figure 1.5.

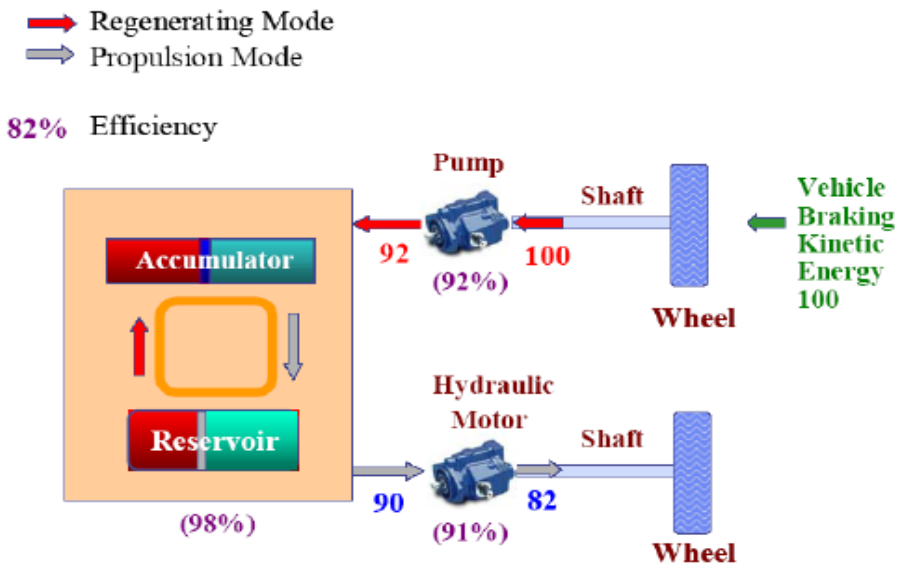

Figure 1.5 Round-trip efficiency of hydraulic hybrid vehicle system[20]

1.2.2 Li-ion Battery Fundamentals

Figure 1.6 illustrates the electrochemical process within a lithium-ion cell. A typical Lithium ion cell consists of a positive electrode (cathode) and a negative electrode (anode). A separator is used as an insulator in between two electrodes to prevent internal shorting. Cathode and anode are attached to alumina and copper current collectors respectively. Common cathode materials include $LiCoO_2$, $LiMn_2O_4$, $LiFePO_4$, etc. Anode usually uses carbonaceious material, such as, graphite, hard carbon, and petroleum coke. The porous electrode includes PVDF binder, conductive additive (carbon blacks), and active materials. The porous structure of electrode is filled with electrolyte, which is a lithium salt in an organic solvent and provides the media for lithium transportation. A common used electrolyte is $LiPF_6$ dissolved in EC/DMC 1:1 solution. When the battery is being charged, the lithium is deintercalated from the cathode electrode, diffused through electrolyte, and transferred to the anode electrode where lithium ions intercalate

into anode particles. When the battery is being discharged, the lithium is deintercalated from anode and intercalated into cathode.

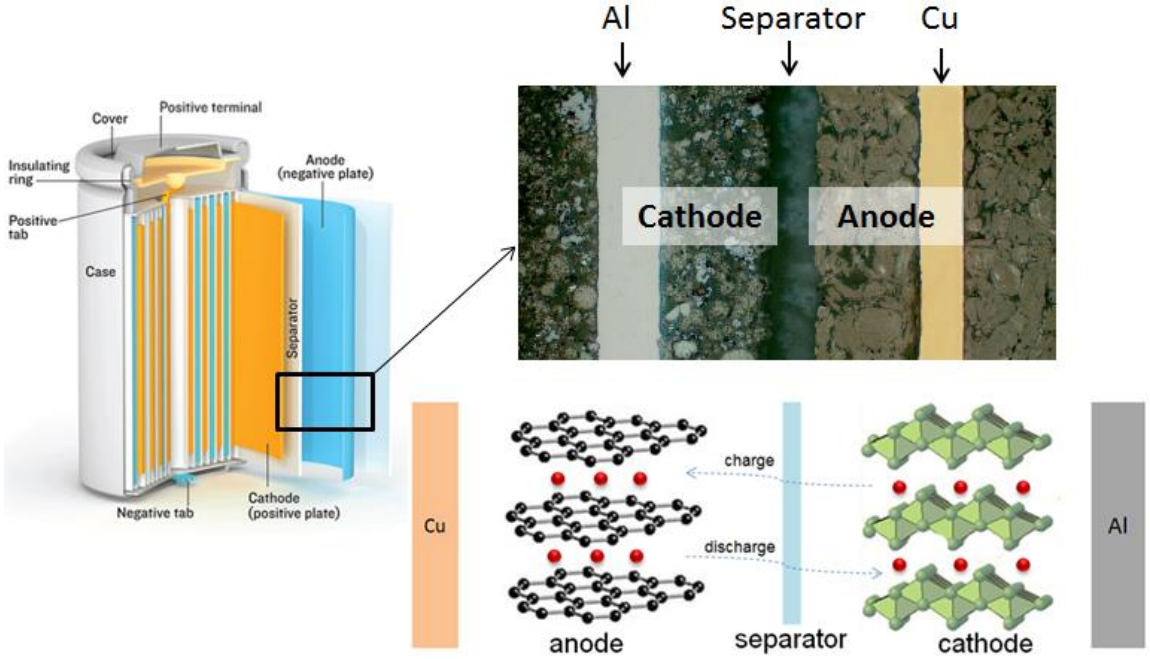

Figure 1.6 Lithium ion battery configuration [21]

Spinel lithium manganese oxide $LiMn_2O_4$, as one of the common used cathode materials, has many desirable advantages, including high rate performance, high energy density, low cost, low toxicity, and simplicity of preparation[22]. In this dissertation, $LiMn_2O_4$ is chosen as the cathode active material. As shown in Figure 1.7, $LiMn_2O_4$ has a cubic close-packing arrangement of oxygen ions at the 32e sites, the Li ions at the tetrahedral 8a sites, and the Mn^{3+} and Mn^{4+} ions at the octahedral 16d sites[23]. Generally, lithium manganese oxide has two voltage plateaus, one about 4V versus Li/Li^+ and the other about 3V versus Li/Li^+. Usually, only the 4V plateau is used in the practical applications. Compared with 3V plateau, 4V plateau is highly reversible and leads to higher specific energy[24]. The charge/discharge reaction of the lithium manganese oxide spinel occurs through extraction/insertion of lithium ions from/into the Mn_2O_4 host lattice.

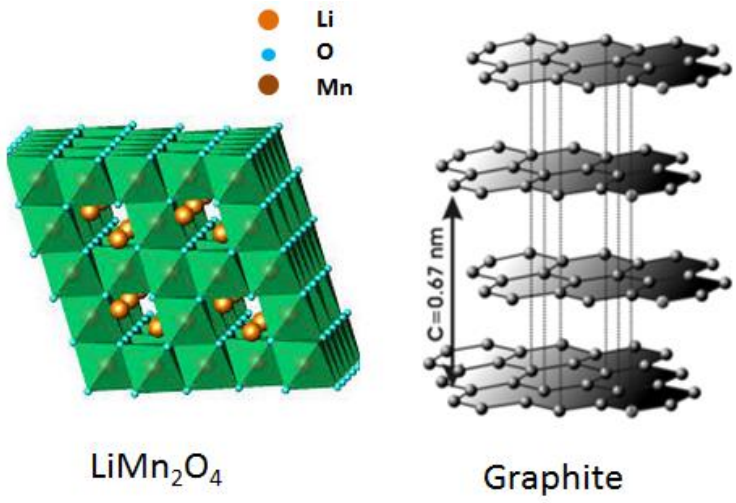

Figure 1.7 $LiMn_2O_4$ spinel structure and graphite structure

Graphite is commonly used as anode in the Lithium ion battery. As shown in Figure 1.7, graphite as a layered, planar structure. In each layer, the carbon atoms are arranged in a honeycomb lattice with separation of 0.142 nm, and the distance between planes is 0.335 nm[25].

The chemical reactions in the lithium ion batteries which have $LiMn_2O_4$ as cathode active material and graphite as anode active material can be expressed in the following equations:

Negative electrode reaction: $Li_xC_6 = C_6 + xLi^+ + xe^-$

Positive electrode reaction: $Li_{1-x}Mn_2O_4 + xLi^+ + xe^- = LiMn_2O_4$

Net reaction: $Li_{1-x}Mn_2O_4 + Li_xC_6 = LiMn_2O_4 + C_6$

1.2.3 Electrochemical Model

The most established mathematical description of porous battery electrodes is Newman's model[26], which incorporates the behavior of both solid phase via porous electrode theory and liquid phase via concentrated solution theory. This model is general enough to be applied to various active materials and electrolyte solutions with different properties and has been used in various studies. In this model, battery system is divided into three domains. As shown in Figure 1.8, the three domains include a negative electrode, separator, and a positive electrode. The

composite electrodes which consist of active material with small amount of binder and conductive additive, and electrolyte solution, are modeled using porous electrode theory.

Due to the tortuosity from the porous structure, the conductivity of the solid phase, and the diffusivity and ionic conductivity of the liquid phase need to be corrected by using Bruggeman equations as shown in the following [26].

$$k_1^{eff} = k_1(\varepsilon_1)^p \tag{1.1}$$

$$k_2^{eff} = k_2(\varepsilon_2)^p \tag{1.2}$$

$$D_2^{eff} = D_2(\varepsilon_2)^p \tag{1.3}$$

Where k_1^{eff} is the effective conductivity of solid phase, k_1 solid phase conductivity, ε_1 is active material volume fraction, ε_2 is porosity (electrolyte phase volume fraction), p is Bruggeman porosity exponent, D_2^{eff} is the effective electrolyte phase Li diffusion coefficient and D_2 is the electrolyte phase Li diffusion coefficient

The potential distribution in the solid phase is governed by Ohm's law as shown in the following equation.

$$\frac{\partial}{\partial x}\left(k_1^{eff}\frac{\partial \phi_1}{\partial x}\right) - j_{loc} = 0 \tag{1.4}$$

Where k_1^{eff} is the effective conductivity of solid phase, j_{loc} is the intercalation flux.

The potential distribution in the electrolyte is governed by the following equation

$$\frac{\partial}{\partial x}\left(k_2^{eff}\frac{\partial \phi_2}{\partial x}\right) - \frac{\partial}{\partial x}\left(k_{2D}^{eff}\frac{\partial}{\partial x}\ln c_2\right) + j_{loc} = 0 \tag{1.5}$$

Where k_2^{eff} is the effective conductivity of the liquid phase, k_{2D}^{eff} is the effective electrolyte phase Li diffusion conductivity, c_2 is the lithium concentration in the electrolyte.

The mass transportation in solid phase is governed by the diffusion law as shown in the following equation.

$$\frac{\partial(c_1)}{\partial t} = \frac{D_1}{r^2}\frac{\partial}{\partial r}\left(r^2\frac{\partial c_1}{\partial r}\right) \tag{1.6}$$

Where c_1 is the lithium concentration in the solid phase, D_1 is the lithium diffusivity of solid phase.

The mass transportation in the electrolyte is governed by the following equation.

$$\frac{\partial(\varepsilon_2 c_2)}{\partial t} = \frac{\partial}{\partial x}\left(D_2^{eff}\frac{\partial c_2}{\partial x}\right) + \frac{1-t_+^0}{F}j_{loc} \tag{1.7}$$

Where ε_2 is the porosity, D_2^{eff} is the effective electrolyte phase Li diffusion coefficient, t_+^0 is the transference number.

Reaction rate is coupled to phase potentials by the Butler-Volmer kinetic expression:

$$j_{loc} = a_s i_0\left\{\exp\left[\frac{\alpha_a F}{RT}(\eta)\right] - \exp\left[-\frac{\alpha_c F}{RT}(\eta)\right]\right\} \tag{1.8}$$

$$\eta = \phi_1 - \phi_2 - U \tag{1.9}$$

Where U is Negative/Positive electrode equilibrium potential, a_s is the active surface area per unit electrode volume, i_0 is the exchange current density, α_a, α_c, are charge transfer coefficients, R is the gas constant, T is the absolute temperature.

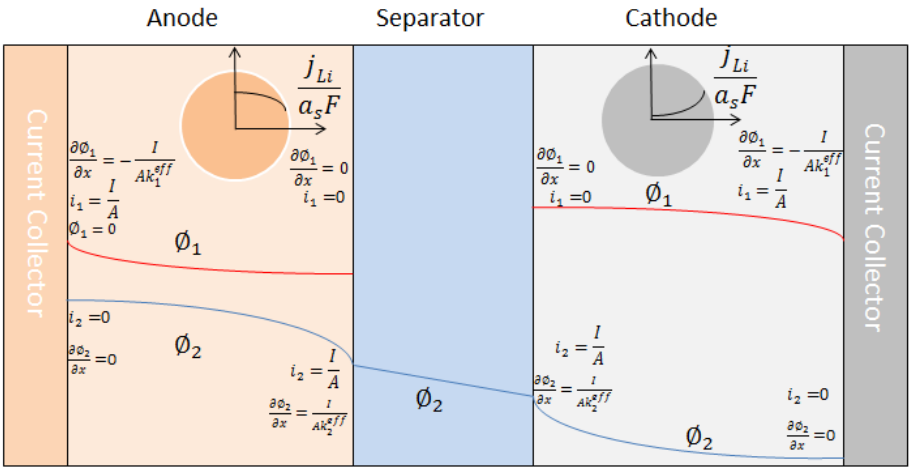

Figure 1.8 Schematic representation of the lithium ion battery model during discharge

Figure 1.8 shows the potential distributions of the solid and liquid phases during discharge, and the boundary conditions between different domains.

Newman's model has a good prediction on the battery performance compared with experiments' results[27]. It provides a good mathematical tool for battery optimal design, such as, energy density and power density design. Du *et al*. [28] developed a surrogate modeling framework based on Newman's electrochemical model to investigate the gravimetric energy density of a Li-ion cell with respect to different design parameters. Xue *et al*. [29] applied gradient-based optimization to Newman's battery model to optimize the energy density for different power requirement. Smith *et al*. [30] augmented Newman's model with thermal distribution in the Li-ion cell, and conducted power density analysis, which indicated the solid state diffusion is the limiting mechanism for the power output. Newman's model achieves great success in the battery optimization design. This model captures the key dynamics in the battery, and enables the optimization of the cells under different requirements.

However, due to the lack of degradation mechanisms, Newman's model provides no information about battery capacity fade. Battery health becomes more and more important due to the high cost of replacing large scale battery pack. It is urgently needed to enhance the battery model in order to optimize battery lifetime. Due to the complexity of the battery degradation, many different side reactions need to be considered. The following section presents a review of the major degradation mechanisms in the battery capacity fade.

1.2.4 Side Reactions

The capacity of a lithium ion battery decreases as it cycles. The capacity fade is due to many different mechanisms which are associated to different side reactions. These side reactions occur on anode, cathode, and also electrolyte. These capacity fade mechanisms are not included in the

Newman's model. Consequently, the model cannot predict the battery capacity fade during cycling. Blow, we first discuss the side reaction in the electrolyte, then the side reaction in the cathode, and finally we discuss the side reaction in the anode.

The electrolyte consists of organic solvent and Li salt. One of the most common used electrolytes in the Li-ion batteries is the mixtures of ethylene carbonates (EC), and dimethyl carbonate (DMC), and lithium hexafluorophosphate ($LiPF_6$). The high potential cathode electrodes used in the lithium ion batteries put a strict requirement on electrolyte stability. Many electrolytes used in the lithium ion batteries decompose at voltage higher than 4.5V, and form a SEI layer on the cathode surface [31, 32], which block the pores of the electrodes and lead to gas generation[12]. High voltage induced electrolyte oxidation not only introduces the SEI layer on the cathode surface, but also generates the protons[33]. The protons generated have a significant impact on Mn dissolution on the cathode surface.

During cycling, cathode electrode experiences the degradation. Lithium manganese oxide (LMO) spinel, as one of the most commonly used cathode materials, has been extensively investigated during the past 10 years. LMO spinel is a good cathode material due to its economic and non-toxic features. However, capacity degradation during cycling becomes an obstacle for its higher market share. Several degradation mechanisms, such as surface film formation, electrolyte decomposition, and Mn dissolution have been proposed for the capacity loss. Jang *et al.*[34] stated that manganese dissolution is the primary reason for capacity fade in the LMO spinal cathode. They also reported that the solvent molecules are electrochemically oxidized and that spinel dissolution is promoted by the acids generated as a result of solvent oxidation[35]. Their results revealed the important link between the generation of protons and manganese dissolution. The dissolution of Mn due to acid attack is also observed in the experiments. A long

term cycled cathode electrode was examined by SEM in this study, as shown in Figure 1.9. The cathode particle surface has clear tiny grooves, which are suspected to be caused by acid attack. In order to quantitatively study LMO degradation, Park *et al*.[36] developed a mathematical model of LMO cathode degradation based on the Mn(III) disproportionation mechanism[37]. Later, Dai *et al*.[38] proposed a capacity fade model including acid generation from two side reactions (solvent oxidation and the $LiPF_6$ decomposition); acid-promoted Mn dissolution was also studied. Although the dissolution of Mn in the LMO spinel cathode is an important factor for capacity fade, chemical analytical results indicate that capacity loss caused solely by Mn^{2+} dissolution accounts for only 34% and 23% of the overall capacity loss at 50 ℃ and room teperature, respectively[39]. Not only does Mn dissolution lead to cathode degradation, but the reduction reaction of Mn^{2+} on the negative electrode causes additional capacity fade as well [40].

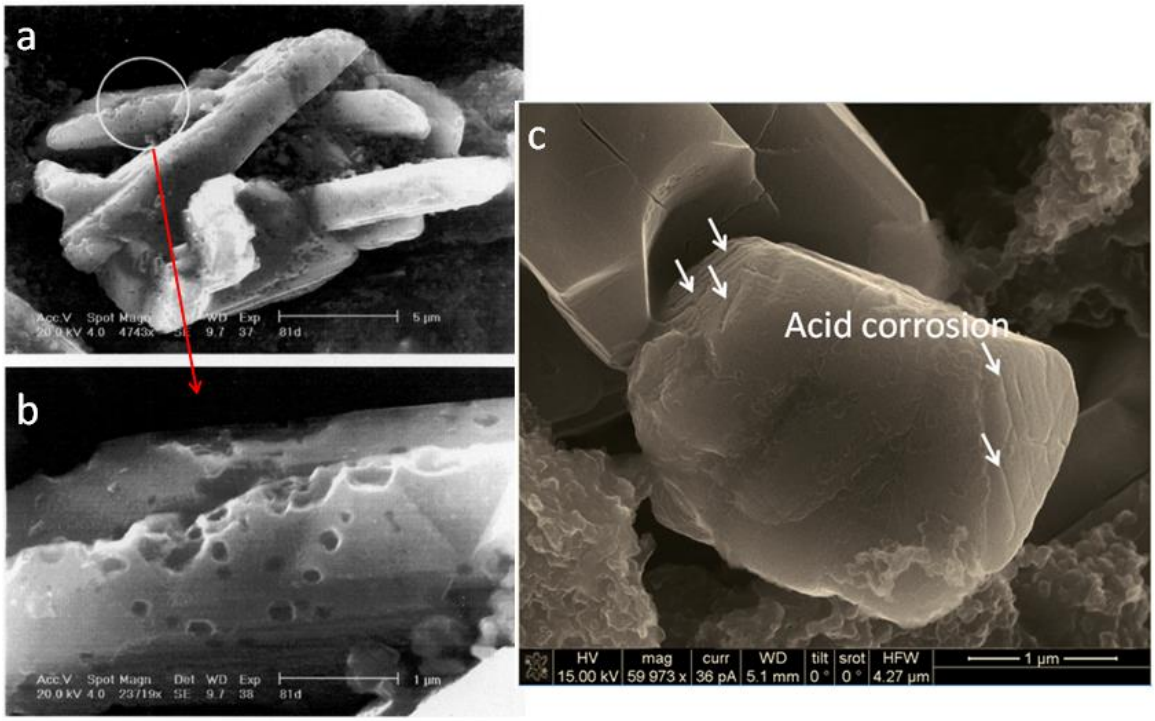

Figure 1.9 a) and b) shows the acid corrosion induced Mn dissolution of a LiMn2O4 fresh electrode left at 55 ^{o}C for 2 months [41]; c) shows the Acid attack induced Mn dissolution in a LiMn2O4 electrode after over 1000 cycles.

Another important degradation mechanism of the cathode is particle fracture due to the stress induced by Li intercalation/deintercalation. Particle fractures in the cathode electrode have been observed in experiments [42-44] after cycling as shown in Figure 1.10. There is a 6.5% volume change in the cubic phase of $LiMn_2O_4$ during cycling[45]. During Li insertion into the lattice of active material in electrodes, the lattice is expanded accordingly. The non-uniform lattice expansion due to this concentration gradient can cause non-uniform strain inside the particle. And this uneven strain results in stress. As intercalation/deintercalation continues, the particle undergoes cyclic stress load, which eventually leads to particle fracture after certain number of cycles. The particle fracture results in loss of electric contact and increase of resistance, and therefore reduces the cathode capacity.

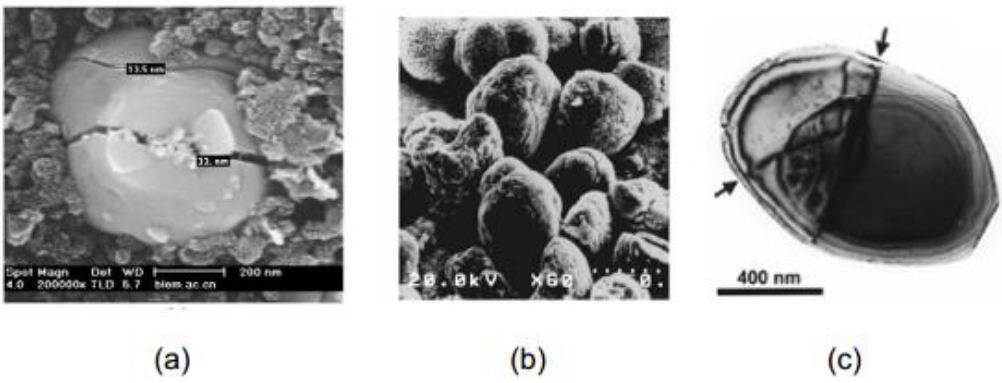

Figure 1.10 experimental observation of fracture in cathode particles: (a)$LiFePO_4$ particle fracture after 60 cycles[42]; (b) gold-codeposited $LiMn_2O_4$ electrode particles after cyclic votanmetric tests at a scan rate of 4mV/s[43]; (c)$LiCoO_2$ particles after 50 cycles[44].

On the anode, there are several side reactions occurring. It is now well known that the carbonaceous lithium-insertion electrodes experience a significant amount of irreversible capacity loss during the initial charging cycles[46]. Irreversible capacity loss during the first few cycles is thought to result from the formation of the SEI layer on the surface of the carbon. As shown in Figure 1.11, in the initial cycles, the lithium ions, electrons combine with the

electrolyte to form the SEI in the immediate vicinity of the anode[47]. Zhang *et al.*[48] used the measured the SEI thickness by elemental line scan analysis, and showed that the initial SEI film has a thickness range of 450 nm to 980 nm. In the SEI formation, Li salt is produced, such as, LiF. The SEI layer continues growing and dissolving due to the continuous reduction of the electrolyte and the reformation of the SEI layers. The process consumes the cyclable lithium ions, which leads to irreversible capacity loss in the lithium ion batteries. SEI formation can remove a significant amount of the cyclable lithium depending on the type of carbon used. For the graphitic materials such as Osaka Gas mesocarbon micobeads (MCMB) irreversible capacity is as low as 8 to 15%, whereas for the hard carbons it can be as high as 50% of the reversible capacity.[12]

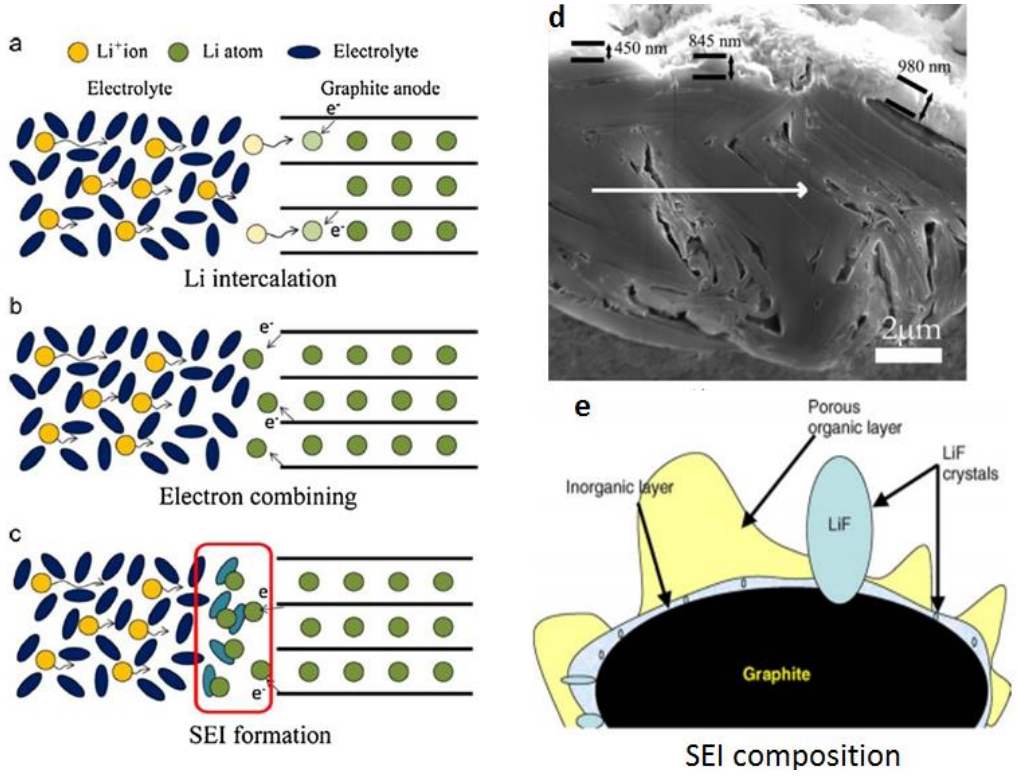

Figure 1.11 a) Li intercalation into graphite, b) electrons and Lithium ions are coupled together, c) SEI formed[47]; d) SEM image shows the cross section of the natural graphite sphere, the SEI thickness varies from 450 nm to 980 nm[48]; e) SEI composition on graphite surface[49]

Another important side reaction on the anode surface is the metallic lithium deposition[50]. The metallic lithium deposition is expected for the cells with a higher than desired initial mass ratio. Figure 1.12 shows the experimental observation of Li plating on an MCMB electrode[51]. Because of the highly reactive nature of metallic lithium, the deposited lithium on the negative electrode can quickly react with the electrolyte, and causes cyclable lithium loss and electrolyte reduction. The primary products of the deposited lithium reacting with solvent and salt molecules are Li_2CO_3, LiF, or other products [46, 52]. Lithium deposition may even occur at high current or low temperature to the cells with correct mass ratio because of the high polarization of the negative electrode. However, the most common circumstance that leads to the lithium deposition is the imbalanced cells with excess positive electrode mass.

The most likely place where metallic lithium occurs is expected to be near the electrode-separator boundary due to the more negative potential than other regions. Formation of metallic lithium not only reduces the cyclable lithium, but also is a safety hazard due to the highly reactive nature of metallic lithium and cell internal shorting.

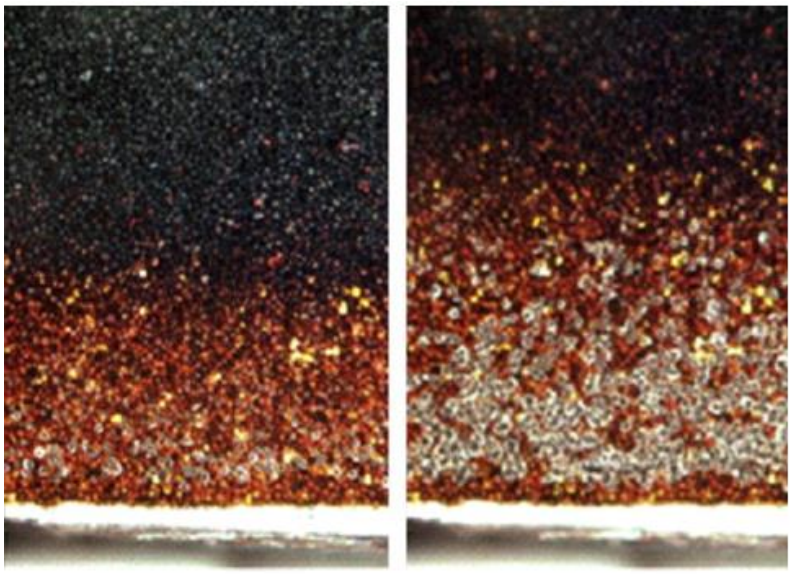

Figure 1.12 Li plating on the MCMB electrode [51]

The existence of Mn deposition has been experimentally confirmed on the anode surface by electron probe microanalysis [41, 53]. Xiao *et al*. [54] observed the Mn particle deposited on the graphite surface by TEM as shown in Figure 1.13. S. Komaba et al. [55] conducted a cycling experiment in 1 mol/dm^3 $LiClO_4$ EC/DEC solution where Mn was added before and during cycling. The graphite discharge capacity was severely decreased by Mn deposition. The Mn deposition is believed decrease the cyclable lithium ions because the manganese deposition may occur instead of lithium insertion into the anode during charging.

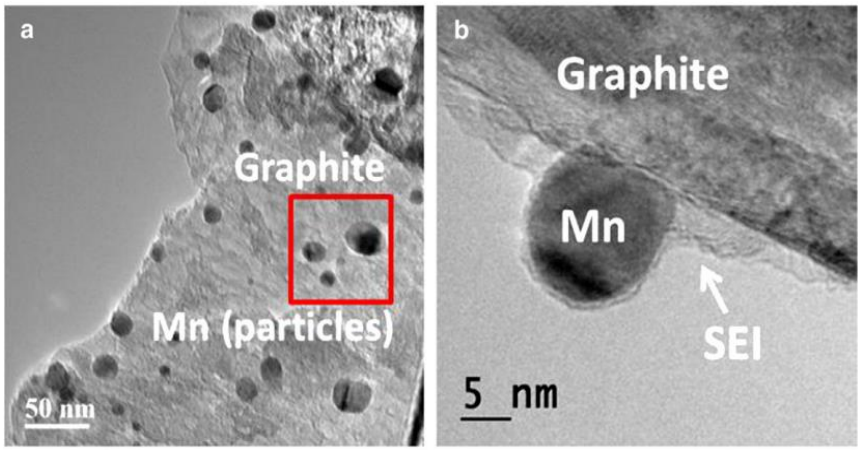

Figure 1.13 a) TEM image showing Mn nanoparticles on the graphite surface; b) Mn nanoparticle (~14 nm in diameter) deposited on the graphite surface[54]

As discussed above, the major side reactions are divided into three domains: anode, cathode, and electrolyte. Table 1.2 summarizes the main side reactions in different domains. The listed side reactions are the key ones considered in this dissertation.

Table 1.2 Key side reactions

Anode	**Electrolyte**	**Cathode**
SEI film	Solvent reduction & oxidation	Particle fracture
Lithium plating	Salt decomposition	Mn dissolution
Mn deposition		

Prior to this dissertation, battery degradation research has been largely focusing on different individual side reactions. One of our objectives is to investigate the interaction between different side reactions. Yet, the fusion of different degradation mechanisms contains several technical challenges.

1.3 Research Challenges

Hydraulic electric hybrid vehicle optimal control development and the cycle life improvement for Li-ion battery system are particularly challenging for the following reasons:

- The hydraulic electric hybrid vehicle has multiple energy source and power devices, the supervisory control to manage multiple energy source and power sources is difficult.
- The degradation mechanisms are complex, the contribution of each individual degradation mechanism to the overall battery capacity fade is unclear, and the interactions between different degradation mechanisms are poorly understood.
- The long term cycling leads to a significant amplification of small change at each individual moment. Capturing small changes is extremely difficult.
- The same battery parameters have different, or even opposite effects on different degradation mechanisms. Changing one parameter may be beneficial to one degradation mechanism, but had adverse effect on the others.
- The high computational cost and high nonlinearity of simulating a multi-physics based electrochemical model and the lack of a complete understanding of side reactions occurring in the battery system have hindered the implementation of optimization schemes in the battery design.

- Battery application requires not only the energy density and high power performance, but also the long cycle life. The multi-objective nature brings up more aspects to consider when optimal design.

1.4 Dissertation Organization

This dissertation is organized as follows. In Chapter 2, the hydraulic electric hybrid vehicle model is developed and the supervisory control is optimized in order to improve the all-electric range and battery health. In Chapter 3, the detailed system design of the hydraulic-electric hybrid vehicle is introduced. In Chapter 4, a side-reaction coupled electrochemical model is developed for the capacity fade analysis of lithium ion batteries. This side-reaction coupled electrochemical model includes the major side reactions: anode SEI growth, Mn deposition, cathode fracture, Mn dissolution, electrolyte oxidation and salt decomposition. The cell internal resistance increase due to SEI formation on the surface of anode is also included. In Chapter 5, the effects of different degradation mechanisms on capacity fade and battery performance are studied quantitatively. As a result, it is found that the degradation process of a Li-ion cell can be divided into three main stages: acceleration, stabilization and saturation. This analysis clearly explains the role and process of each degradation mechanism on the life of the battery at each stage. The three electrode cell is fabricated and cycled over long term, and the experimental results are obtained to provide the physical evidence. Cycled anode and cathode were also examed by SEM and TEM to identify the main degradation mechanisms. Cathode fracture was observed repeatedly, which leads to our further study of fracture impact on the capacity fade. In Chapter 6, a single particle fracture model is developed to study the impact of fracture on the capacity fade. The study explores the effect of SOC, and conductivity on the fracture. Chapter 7 summaries the findings from Chapter 5 and Chapter 6, based on the findings, potential ways to improve the

battery cycle life are proposed, a general procedure is developed to optimize the battery health while fulfilling the energy density and power density requirements. Chapter 8 concludes the main results of this dissertation, the new contributions to the field and the possible future research directions.

Chapter 2
Hydraulic-Electric Hybrid Vehicle Control Optimization

Limited fossil fuel reserves and global warming provide a strong driving force for developing a highly efficient and clean transportation system. This chapter presents a low-cost path for extending the range of small urban pure electric vehicles by hydraulic hybridization. Energy management strategies are investigated to improve the electric range, components efficiencies, as well as battery usable capacity. As a starting point, a rule-based control strategy is derived by analysis of synergistic effects of lead-acid batteries, high efficient operating region of DC motor and the hydraulic pump/motor. Dynamic programming (DP) is used as a benchmark to find the optimal control trajectories for DC motor and a hydraulic pump/motor. Implementable rules are derived by studying the optimal control trajectories from DP. With new improved rules implemented, simulation results show electric range improvement due to increased battery usable capacity and higher DC motor operating efficiency.

2.1 Introduction

This chapter investigates a novel concept for extending the range of small urban electric vehicles. Light-duty vehicles provide the most common transportation service. Over 85% of travel in the United States is in light-duty vehicles [56, 57]. In recent years, electric vehicle manufacturers have been speeding up the electric vehicle development. The attractiveness of light-duty EVs stem from zero direct carbon emissions, low fuel costs, and diverse energy sources including nuclear power, fossil fuels, and renewable sources such as wind, and solar

power, which can significantly reduce the dependence on oil. To achieve low cost, using the mature and simple lead-acid batteries and electric machines such as the brushed DC motor is always a good choice for manufacturers. Under these circumstances, the main goal for light-duty EVs is to extend the electric range without compromising vehicle life and while maintaining low cost.

Hydraulic hybridization is one of the effective ways to achieve range improvements through effective regeneration due to the low cost and high efficiency of the hydraulic system. Compared with an electrochemical battery, a hydraulic accumulator has more power density with less energy capacity [58, 59]. Therefore, adding a hydraulic system to an EV combines both advantages of high power density and high energy capacity. This holds a promise of significantly improving the electric range of operation, but also opens the question of how to coordinate the operation of these two energy storage systems to better satisfy the power demand and improve the overall efficiency.

The platform used in this study is a light-duty PK truck called Xebra as shown in Figure 2.1 from ZAP Jonway, a new automotive manufacturer in electric vehicles (EVs). Based on the existing EV configuration, a low-cost solution for improving the electric range is proposed as shown in Figure 2.2. To get the performance and calibration data for later vehicle modeling, this Xebra truck was tested for range and efficiency under different driving cycles at the US EPA National Vehicle and Fuel Emissions Lab. Vehicle status data such as speed, battery voltage, current, power, charging energy, and AC energy from the wall were recorded over the tests.

The Xebra has a battery pack consisting of six 12V lead-acid batteries, which can provide 4.64 kWh at 1C and costs $1,050. It takes up to 12 hours to charge the battery pack that is 100%

discharged. A 5kW brushed DC series wound motor is coupled to the wheel through the reduction gears with gear ratio 4.5:1. No regenerative braking is allowed in the stock Xebra.

The previous work [60] introduced several energy management options for Xebra. The objective of this chapter is to further investigate the energy management options for the hydraulic-electric hybrid light urban vehicle. The chapter is organized as follows. In the first part the modeling effort is presented. Then the intuitive rule based strategy is proposed, based on the analyses of the component efficiencies. In order to explore the best achievable system efficiency, Dynamic programming technique is introduced. The near-optimal control rules are extracted from the DP result to be applied in the real world.

The baseline EV uses a Lead-acid battery and a DC motor to minimize cost. Regeneration was not possible. The option to improve the range with more advanced Li-ion battery is prohibitively costly, as it almost doubles the price of a small urban vehicle. Instead, we propose integration of a compact and low-cost hydraulic regeneration system. As the only energy source in the EVs, battery usable capacity becomes an important factor to the vehicle electric range. In order to better understand the lead-acid battery performance, a high fidelity battery model is developed based on the testing data from the US EPA National Vehicle and Fuel Emissions Lab. Simulation study shows the usable capacity is highly dependent on the usage patterns. Aggressive discharging can significantly decrease battery usable capacity. A high power density hydraulic system can avoid high current demands on battery and therefore improve its usable capacity significantly.

Figure 2.1 Xebra light-duty pickup truck from ZAP Jonway.

2.2 Hydraulic Electric Hybrid System

Based on the stock Xebra PK truck, hydraulic system was designed and added to the stock Xebra in order to improve the vehicle electric range. The hydraulic system consists of a 45cc bent-axis pump motor with variable displacement, a 23 L hydraulic accumulator with maximum pressure of 344 bars and a 30 L hydraulic oil tank. The hydraulic Pump Motor (PM) shaft is coupled to the DC motor shaft in parallel through a gear reduction to achieve the gear ratio 2.9:1 from PM shaft to wheel shaft. The configuration of the Hydraulic-Electric Hybrid Vehicle (HEHV) is shown in Figure 2.2. The parameters for electric and hydraulic components are listed in Table 2.1.

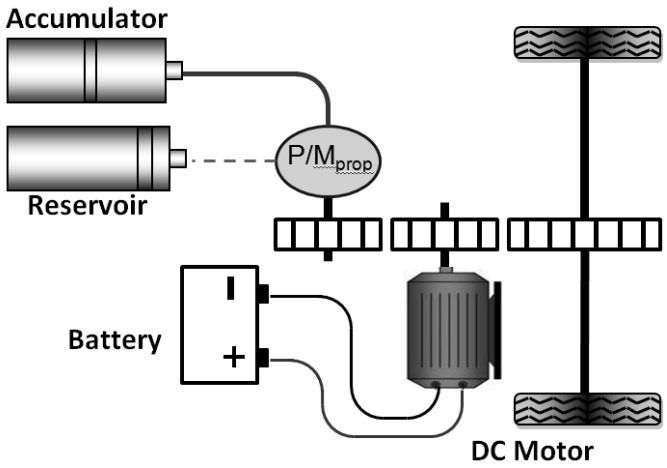

Figure 2.2 Hydraulic-Electric Hybrid Vehicle (HEHV) Parallel Configuration.

Table 2.1 Components Parameters.

DC motor Power Nom.	**5.0 kW**
Battery Capacity @ 1C	4.64 kWh
Battery Mass	199 kg
Final Drive Ratio	4.5:1
PM to wheel Ratio	2.9:1
Pump Motor	45 cc/rev
Accumulator Vol.	23 L
Max. Pressure	344 bars
Oil Tanks Vol.	30 L
Hybrid Vehicle Mass	895 kg

2.3 Vehicle system modeling

The dynamometer tests conducted at the US EPA NVFEL provided a rich set of data for the system modeling and calibration. A baseline EV model was first developed and used as a platform for the further hybridization and energy management strategy study. This baseline model consists of battery model, driver model, DC motor model, DC slave controller, and vehicle dynamic model. The preview was added to the driver model to reduce the velocity overshoot. A physics-based DC series wound motor model was developed as the primary power source [5]. The DC motor model is accurate under certain conditions, however, magnetic flux saturation and losses due to commutator switching have a significant impact on the mutual inductance factor. A 3D map was derived from the testing data to predict the mutual inductance factor under varying speed and torque. The testing data from US EPA NVFEL covers most typical driving styles from aggressive stop-go to moderate cruising, and also includes standard UDDS driving cycle, where the maximum speed was limited to 35mph to match the Xebra specifications. The baseline model was calibrated and validated with a variety of data collected under different driving cycles.

After validating the baseline EV model with actual testing data, hydraulic system was added to build the hybrid model. The hydraulic pump motor model is based on Wilson's equations [61].

The model accounts for both volumetric and torque losses in the pump motor, the volumetric losses include laminar leakage loss, turbulent leakage and the loss due to fluid compressibility. Torque losses include losses due to fluid viscosity and mechanical friction. The hydraulic accumulator is modeled based on the Benedict-Webb-Rubin (BWR) equations [61]. The hydraulic accumulator model can predict both the pressure and temperature change during discharging and charging. More details about the DC motor, hydraulic pump motor, vehicle dynamics, driver model are available in references [60]. The whole HEHV model is shown in the Figure 2.3.

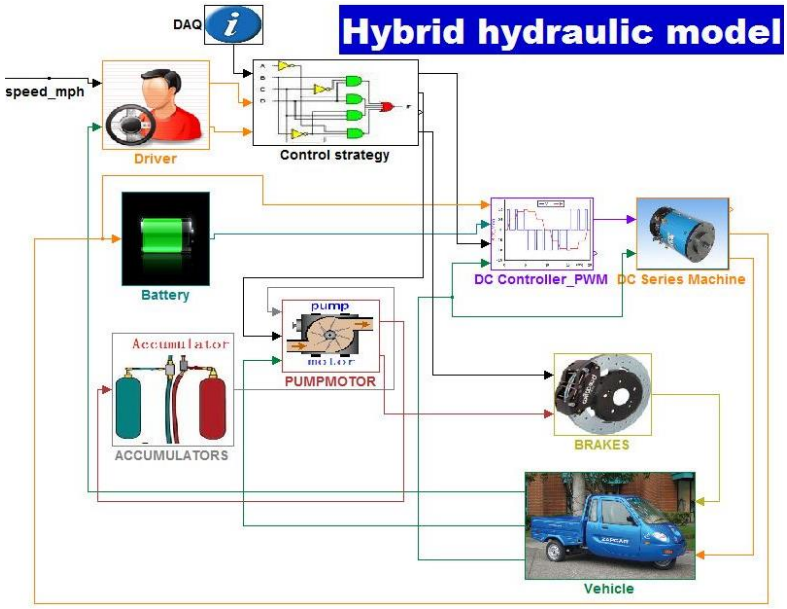

Figure 2.3 Hydraulic-Electric Hybrid Vehicle (HEHV) Simulation Model.

2.3.1 Enhanced Battery SOC Estimation

Battery state-of-charge (SOC) is vital in the evaluation of the energy saving in this study. The battery capacity is usually specified for a certain discharge time of n hours, for example, C_n =200 Ah means that 200 Ah is delivered if discharged at such a rate that the discharge time is n hours. The discharge rate can be calculated by Eq. (2.1)

$$I_n = \frac{C_n}{n}, \tag{2.1}$$

According to Peukert's findings [62], the relationship between battery usable capacity C_{n1} and the discharge rate I_{n1} can be expressed as Eq. (2.2)

$$C_{n1} = C_n \left(\frac{I_n}{I_{n1}}\right)^{pc-1}, \tag{2.2}$$

Where C_{n1} is the usable capacity that the battery will deliver if the discharged at such a rate that the discharge time is n1 (h). pc is the "Peukert coefficient" (usually between 1 and 2) unique to a battery of a certain make and model [62].

Peukert's findings show the impact of different constant discharge rates on the battery usable capacity. Eq. (2.2) can be used to calculate the usable capacity under constant discharging. However, due to the non-uniform power demand over the driving cycle, the discharging current varies all the time through the driving cycle, which causes troubles to use Peukert's equation to calculate the usable capacity. Inaccurate usable capacity estimation leads to poor SOC prediction. An enhanced battery model was later developed in order to improve the SOC estimation under varying discharging rate.

As a starting point, a simplified equivalent circuit model (shown in Figure 2.4) for lead-acid pack was used based on the equivalent circuitry introduced by M. Ceraolo [63].

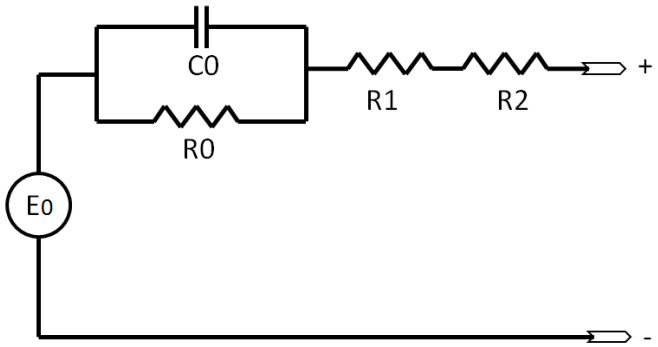

Figure 2.4 Simplified equivalent circuit model for the lead-acid battery pack. [63]

The governing equations are shown in Eqs. (2.3), (2.4), (2.5), (2.6), (2.7). More details are available in the reference [60].

$$E_0 = E_{00} - K_E(1 - SOC), \tag{2.3}$$

$$C_0 = \frac{\tau_1}{R_1}, \tag{2.4}$$

$$R_0 = -R_{00} \ln SOC\ , \tag{2.5}$$

$$R_1 = R_{10} \frac{\exp[A_{11}(1 - SOC)]}{1 + \exp(A_{12} I/I*)}, \tag{2.6}$$

$$R_2 = R_{20}[1 + A_2(1 - SOC)]\ , \tag{2.7}$$

The modeled electromotive force, capacitance, and resistances are represented by E0, C0, R0, R1, and R2, respectively. These variables are dependent upon parameters which were tuned to fit test data. The detailed parameters are shown in Table 2.2.

Table 2.2 Battery Parameters.

E_{00}	**78.2 V**
K_E	7.56
τ_1	60.082 s
R_{00}	0.027958 Ohm
R_{10}	0.13605 Ohm
A_{11}	-10.694
A_{12}	-3.8789
R_{20}	0.02569 Ohm
A_2	-0.3005

The above equivalent circuit model is very accurate in constant discharging, but has a poor capability to estimate SOC under varying discharge. To solve this problem, an enhanced SOC estimation algorithm is introduced to the battery model [64].

The SOC in the above model is calculated by Eq. (2.8).

$$SOC = 1 - \frac{Q}{C}, \tag{2.8}$$

Where C is the battery nominal capacity, Q is the total amount of energy (Ah) discharged. Because the usable capacity changes under different discharging patterns, the C should also be changed accordingly. Rather than changing the denominator C, the enhanced SOC algorithm adjusts the numerator Q according to the discharging patterns. Eq. (2.9) is used to calculate the Q_e under different discharge patterns.

$$Q_e = \int_0^T \alpha(i) i(t) dt - Q_{reg}, \tag{2.9}$$

Q_{reg} is a term introduced for Ah reactivated by electrolyte diffusion during pauses. Alpha is the penalty factor for different current. More details are available in the reference [60].

2.3.2 Battery Tests

Battery discharging data was recorded over different driving cycles (including 3 acceleration cycles with different acceleration rates, 3 steady state cycles with different steady speeds), as shown in Figure 2.5.

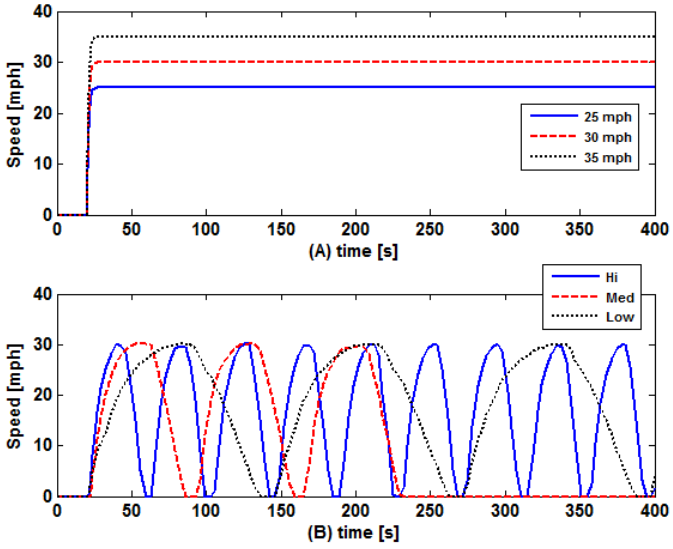

Figure 2.5 A) Steady state cycles, and B) acceleration cycles.

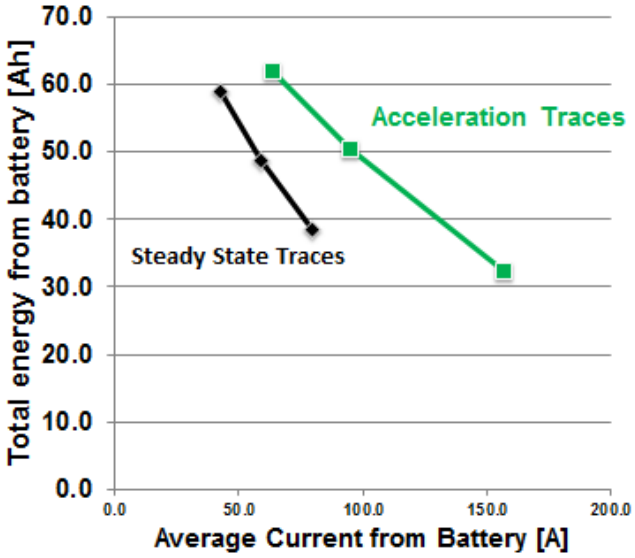

Figure 2.6 Battery Available Capacities under Acceleration Cycles.

In Figure 2.6, compared with steady state traces, the acceleration traces have many pauses between accelerations. Energy is reactivated by electrolyte diffusion during pauses, which leads to more usable energy from the battery. In both steady state and acceleration traces, the total energy from the battery increases as the average current from the battery decreases. And, higher discharge rate also causes the loss of conductivity between adjacent particles in the active material matrix, which leads to uneven current distributions and higher stress on the cell [65, 66]. This increased stress will likely lead to shorter the battery life.

Therefore, in order to get more energy from the lead-acid battery and protect the battery health, one of the objectives of the preliminary rule based control strategy is to keep the battery discharge rate as low as possible.

2.4 Preliminary rule-base control strategy developments

2.4.1 Pure electric drive analysis

One of the reasons to hybridize the pure electric vehicle is the inefficient performance of a baseline DC motor. After calibrating the DC motor to the testing data, an efficiency map was obtained based on DC motor model. It indicates severe efficiency penalties at low RPM's. Figure

2.7 shows the visitation points of the DC motor scattered on the DC motor efficiency map over UDDS driving cycle, where 120A is about the half of the maximum DC motor current.

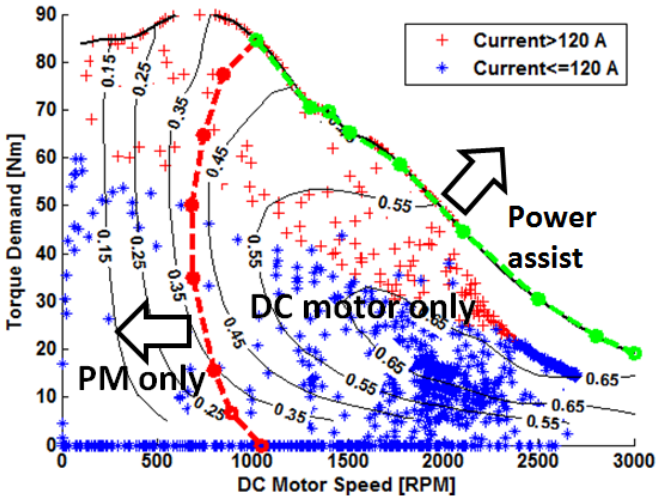

Figure 2.7 DC motor visitation points & proposed preliminary rules.

In the Figure 2.7, on the left side of red curve, the operating points are in the low efficiency zone or high current. In this region, the battery suffers and the DC motor is working inefficiently. In contrast, the hydraulic pump motor has a very significant advantage under the high torque demand and low speed circumstances. Hydraulic pump motor has a very high efficiency with high displacement which means high torque output. A hydraulic pump motor overall efficiency 3D map (as shown in Figure 2.8) was obtained based on the pump motor model which has been calibrated with the testing data. This 3D efficiency map clearly shows that the displacement is the dominant factor that affects the efficiency which means the high torque demand leads to high displacement, and therefore high efficiency. Considering both efficiency of DC motor and hydraulic pump motor, it's quite clear that replacing the DC motor with hydraulic pump motor during high torque and low speed is a perfect match to improve the overall efficiency.

Based on the above analysis, the most intuitive control strategy is proposed. The primary goal of this control strategy is to move the DC motor operating points to the more efficient

region. Figure 2.7 illustrates the basic power split idea on the DC motor efficiency map. The whole DC motor efficiency map is divided into 3 regions. On the left side of the red curve is the low speed region, where only hydraulic pump motor provides all the torque demand as long as there is energy in the accumulator. In case there is not enough energy in the accumulator, DC motor increases the output torque to satisfy the torque demand in the low speed region.

Between the red curve and the green curve, the DC motor replaces the hydraulic pump motor to satisfy the torque request alone. Once the torque demand exceeds the green curve (maximum torque curve) hydraulic pump motor supplies the excess torque. Because the braking energy is "cost free", this control strategy is trying to use regenerative braking whenever possible.

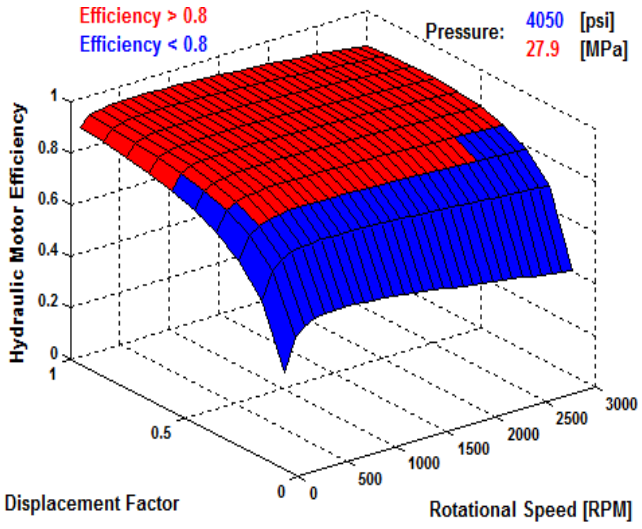

Figure 2.8 Hydraulic pump motor efficiency map.

This control strategy can lower the battery current during acceleration (low speed region). And instead of using DC motor at low RPM's, hydraulic motor can significantly improve the energy conversion efficiency and reduce the current drawn from battery.

Due to the limited power of the 5 kW DC motor, the stock Xebra can only reach 35 mph. The maximum speed of the UDDS cycle is limited to 35 mph to match the maximum speed of Xebra. The simulation evaluates the effectiveness of the control strategy in achieving energy

savings by evaluating the battery SOC at the end of a single driving cycle. More energy savings and higher battery remaining SOC after one driving cycle means longer electric range. It's also more convenient to apply dynamic programming to one driving cycle with fixed length. After incorporating the rule-based control strategy into the vehicle model, the simulation results are generated as shown in Figure 2.9.

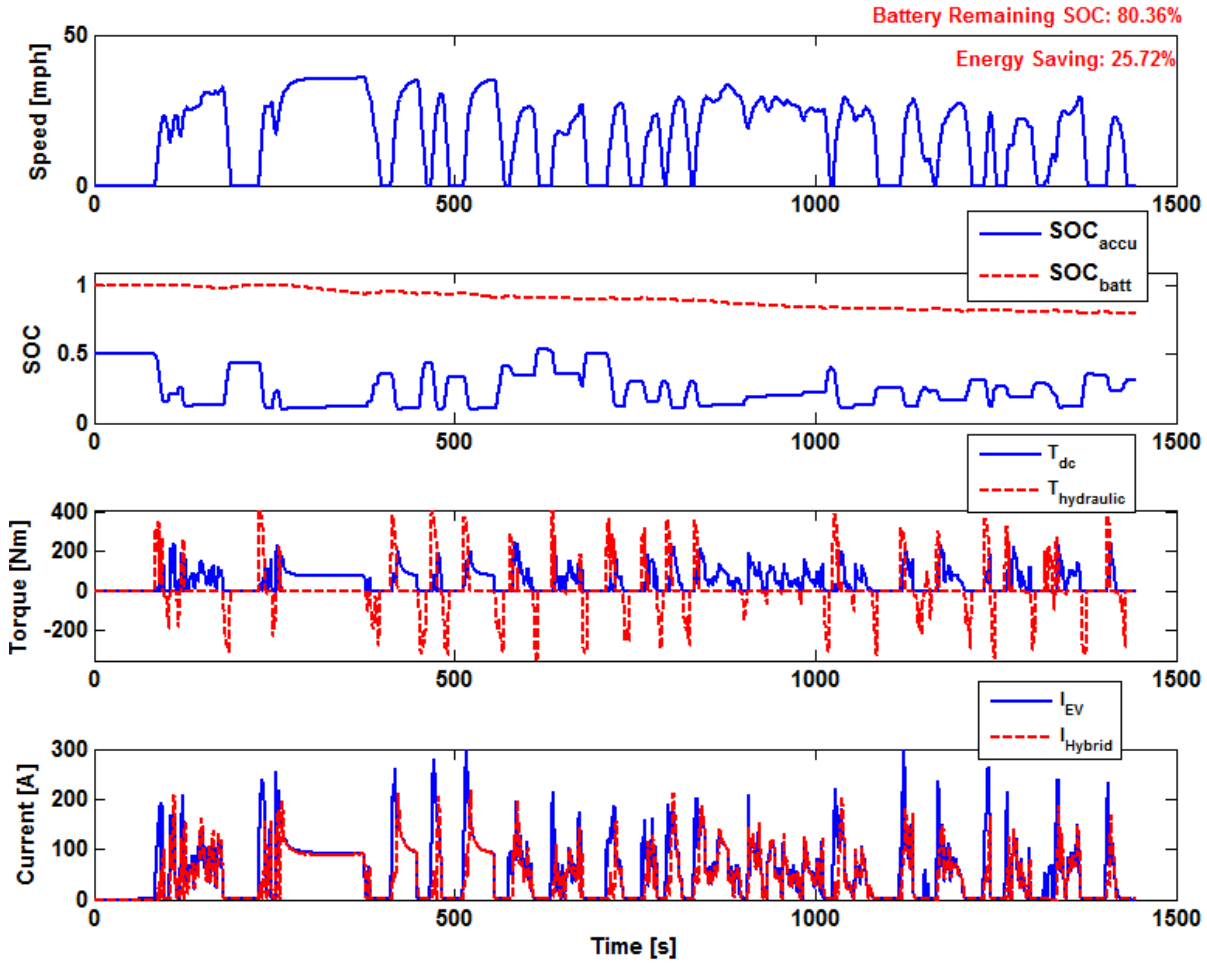

Figure 2.9 Preliminary rule--based control strategy simulation results over UDDS

DC motor torque, hydraulic PM torque, hydraulic accumulator SOC and battery current trajectories show the control actions based on the preliminary rule-based controller over the UDDS cycle. The torque trajectories in Figure 2.9 show that PM is almost used at the beginning of acceleration (low speed), however for some high torque demand in the low speed, which

exceeds the maximum available torque from hydraulic PM, DC motor provides extra toque to overcome high torque demand. A comparison between EV mode and Hybrid mode (preliminary rule-based) is presented in Table 2.3. Overall, the energy consumption is reduced by 25.72% which is mainly attributed to the regenerative braking, efficient DC motor operation, and increased usable capacity of the battery pack due to lower discharge currents. By repeating the UDDS cycles until the battery is depleted, the electric range is obtained for both EV only mode and Hybrid mode. The preliminary rule-based control strategy enables HEHV to achieve 64.75 % range improvement.

Table 2.3 Results comparison: EV, and preliminary rule (PR).

	EV	**PR**	**Improvement**
Energy Consumption (MJ)	5.72	4.25	-25.70%
Remaining $SOC_{batt.}$	67.95%	80.36%	+12.41%
Electric range	13.25	21.83	+64.75%

2.5 Optimization of rule-based control strategy using dynamic programming

2.5.1 Dynamic programming problem formulation

The simulation results from preliminary rule-based control strategy show significant improvement after hybridization and also bring up question about the best achievable energy saving under current hardware configuration. Dynamic Programming (DP) technique was chosen as an effective way to determine the optimal control actions for this control problem. In the past, DP has been successfully applied to replace the Rule-based control strategy for hybrid electric vehicles [67, 68]. In order to find and tentatively reapply the optimal control strategy for HHEV, an optimization problem is formulated and solved by dynamic programming algorithm.

Since the high fidelity model is not suitable for DP analysis (curse of dimensionality), the original high fidelity model is simplified to reduce the computation cost. The details of the simplification are described below.

The simplified vehicle dynamics model which consists of the rolling resistance (tire), rotating friction and the aerodynamic resistance can be approximated by Eq. (2.10)

$$T_d = (v > 0) \cdot f_0 + f_1 \cdot v + f_2 \cdot v^2 + M \cdot a, \tag{2.10}$$

Where v and a are the speed and the acceleration of the driving cycle (UDDS) at time *t*. *M* is the mass of the vehicle.

The simplified DC motor is based on efficiency map as shown in Figure 2.7. The efficiency map is obtained based on the testing data from the US EPA National Vehicle and Fuel Emissions Lab. The DC motor efficiency is a function of motor torque and speed. The DC motor is only outputting positive torque; therefore no regenerative brake is done by DC motor. The governing equations are shown below.

$$T_{dc} = T_d \cdot R_{split}, \tag{2.11}$$

$$\eta_{dc} = f(T_{dc}, \omega_{dc}), \tag{2.12}$$

$$P_{dc} = T_{dc} \cdot \omega_{dc} \cdot \eta_{dc}, \tag{2.13}$$

Where T_{dc} is the DC motor torque, T_d is the total torque demand, R_{split} is the power split ratio (control action u) between DC motor and hydraulic PM.

The hydraulic pump motor is modeled based on the efficiency map shown in Figure 2.8. The governing equations for pump motor are shown below.

$$T_{PM} = T_d \cdot (1 - R_{split}), \tag{2.14}$$

$$D_{PM} = \frac{T_{PM}}{\Delta P \cdot \eta_{PM}}, \tag{2.15}$$

$$\eta_{PM} = f(T_{PM}, \omega_{PM}, D_{PM}), \tag{2.16}$$

$$P_{PM} = T_{PM} \cdot \frac{\omega_{PM}}{\eta_{PM}}, \tag{2.17}$$

Where T_{PM}, D_{PM}, η_{PM}, P_{PM} are the PM torque, displacement, efficiency, and power respectively.

Hydraulic accumulator pressure is calculated based on SOC by Eq. (2.18)

$$\Delta P = SOC_{accu} \cdot \left(P_{max} - P_{pre}\right) + P_{pre}\,, \tag{2.18}$$

Where ΔP, P_{max}, and P_{pre} are the accumulator pressure, maximum pressure, and pre-charged pressure respectively.

The complicated battery model shown in the Figure 2.4 can be simplified to an efficiency map based model for the dynamic programming. The efficiency map for the lead acid battery is obtained by running the high fidelity model in Figure 2.4 under different SOC and discharging power conditions. The efficiency map is shown in Figure 2.10. The battery SOC and discharging efficiency are calculated by Eq. (2.19), (2.20)

$$SOC_{batt} = 1 - \frac{Q_{dis}}{Q_{full}}\,, \tag{2.19}$$

$$\eta_{batt} = f(P_{batt}, SOC_{batt})\,, \tag{2.20}$$

Where Q_{dis}, Q_{full}, P_{batt}, and η_{batt} are the battery discharged energy, full energy capacity, discharging power, and efficiency respectively.

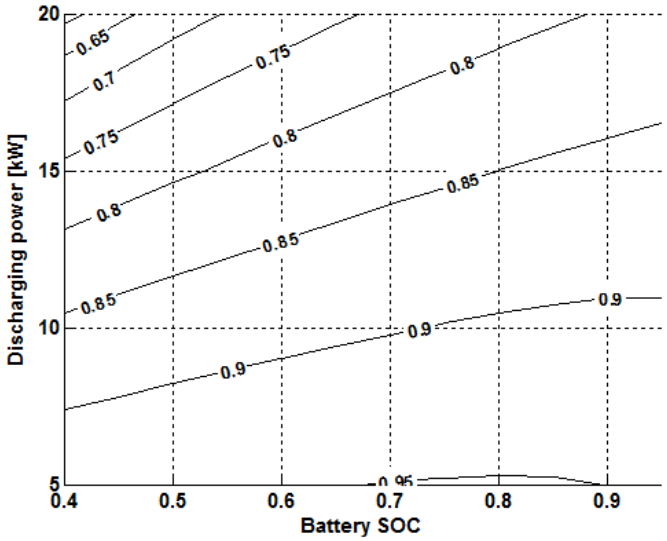

Figure 2.10 Energy efficiency maps of the lead acid battery for discharging.

Minimizing the energy consumption (battery power output) over the UDDS cycle is selected as the objective function in dynamic programming. The objective function is defined by the Eq. (2.21):

$$\min J = min_u \sum_{k=0}^{k=N-1} L\big(x(k), u(k)\big) \ , \tag{2.21}$$

Where L is the energy drawn from battery over a time segment, N is the driving cycle length. x and u are the vectors of state variables (battery SOC, accumulator SOC, etc..) and control signal (power split ratio) respectively. In order to match the final value of accumulator SOC with the initial value, and get higher final battery SOC as much as possible, a penalty term Eq. (2.22) is introduced:

$$P = \alpha(SOC_{accu.}(N) - SOC_{accu.}(0))^2 + \beta(SOC_{batt.}(N)) \ \ , \tag{2.22}$$

Therefore the final objective of the optimization problem can be expressed as Eq. (2.23).

$$\min J = min_u \sum_{k=0}^{k=N-1} L\big(x(k), u(k)\big) + P, \tag{2.23}$$

Based on the simplified model, a generic DP function introduced by Sundström and Guzzella [69], is used to searches for the optimal control actions over the UDDS driving cycle. The optimal states and control trajectories are shown in Figure 2.11.

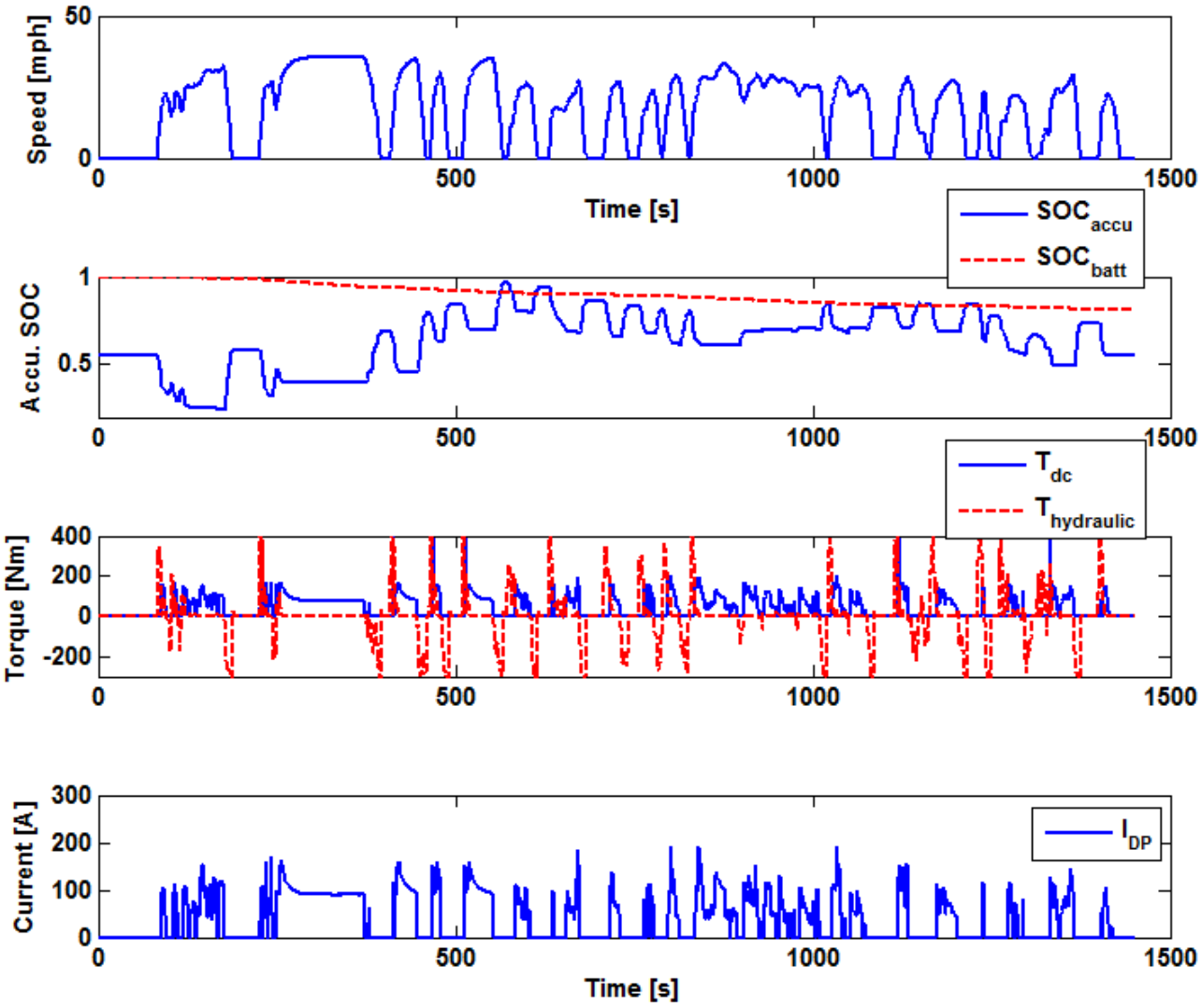

Figure 2.11 Dynamic Programming results under UDDS

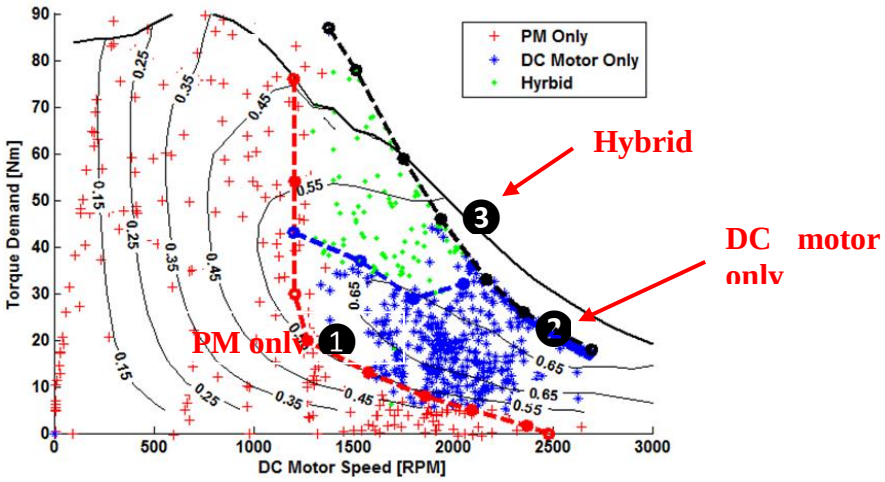

Figure 2.12 Visitation points in DP forward Simulation (Simplified model) & lines defining operating modes for the new rules

Figure 2.12 depicts the visitation points of the simplified model after running through the UDDS driving cycle using the optimal control law from the DP. The visitation figure clearly shows that DP tends to move all the DC motor operating points to the region 2 in Figure 2.12, where the efficiency is highest, and PM is working in the region 1, where the speed is low. When the torque demand and speed are both high in region 3, DC motor and PM are used simultaneously. Three curves are extracted from visitation points in Figure 2.12 to form the new control rules. The red curve called PM only curve defines the region where running PM is preferred. The blue curve called DC motor upper limit defines the DC motor running region. In the region 3, the hybrid mode is engaged and torque from the DC motor and the hydraulic motor are blended together. This new extracted rules should be able to capture the main features of the DP optimal results.

2.5.2 Summary

After implementing the DP improved rules (extracted from DP) into the high fidelity model, additional results are generated and shown in Figure 2.13. Compared with the preliminary rules (in Figure 2.7) which run DC motor above 45% efficiency curve, the improved control strategy

(in Figure 2.13) tends to operate the DC motor in a narrower region with higher efficiency (above 55%) which explains the energy savings listed in Table 2.4. Overall, the improved rules extracted from DP tend to operate the DC motor mainly in the high efficiency region; however, due to the depletion of hydraulic energy, DC motor is also occasionally used in hybrid mode outside of the desired area, such as the upper left corner, and the center bottom area in Figure 2.13.

Even though Dynamic Programming is searching for the optimal control actions over a pre-defined driving cycle UDDS, the simulation result from DP in Figure 2.13 reveals a general and efficient way to operate the whole system. Therefore, the extracted rules are also expected to achieve near optimal performance over different driving cycles.

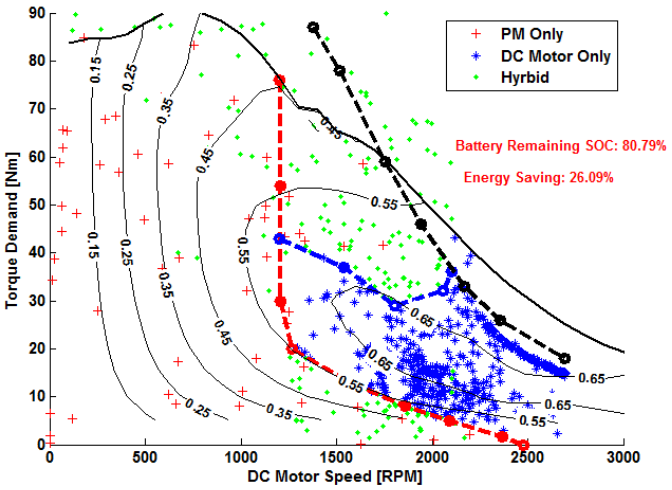

Figure 2.13 Visitation points based on improved rules over UDDS (High fidelity model)
The DP improved rule-based control strategy achieves lower energy consumption and higher remaining SOC, compared to preliminary rules (Table 2.4). The electric range is obtained by repeating the UDDS cycles until battery is depleted.

Table 2.4 Results comparison: EV, PR, Improved Rules.

Configuration	**EV**	**HEHV (Preliminary Rules)**	**HEHV(Improved Rules)**
Energy Consumption	5.72 MJ	4.25 MJ (-25.70%)	4.22 MJ (-26.22%)
Remaining Battery	67.95%	80.36% (+12.41%)	80.79% (+12.84%)
Electric range	13.25	21.83 miles (+64.75%)	22.3 miles (+68.30%)

2.6 Conclusions

Based on the EV model and Hydraulic Electric Hybrid Vehicle model, an energy management problem was formulated with the objective to lower the energy consumption. As a starting point, a preliminary rule-based (PR) control strategy was proposed based on the analysis of the DC motor efficiency and the battery characteristics. The PR control was a simple and intuitive strategy; nevertheless it enabled significant improvements of the system efficiency and increased the electric range. A secondary benefit was achieved by reduced battery peak loads and likely extended battery life.

In order to explore the best achievable energy saving, an optimization problem was formed and solved by Dynamic Programming algorithm. Based on the forward simulation results, optimal rules are extracted from the optimal control trajectory. Results show that the additional energy consumption improvement is mainly from the more efficient DC motor operation. Based on this study, the near optimal and vehicle implementable rule-based energy management strategy was developed for the Hydraulic-Electric Hybrid Vehicle. The next challenge will be to implement designed control strategy into the real vehicle, and this effort is underway.

ACKNOWLEDGMENTS

The authors wish to acknowledge the technical and financial support of the UM Center for Excellence in Engineering through Hybrid Technology by the US Environmental Protection Agency, Office of Transportation and Air Quality.

NOMENCLATURE

EPA	United States Environmental Protection Agency
EV	Electric Vehicle
NVFEL	National Vehicle And Fuel Emissions Lab, Us Epa
$SOC_{accu.}$	Hydraulic Accumulator SOC

$SOC_{batt.}$	Lead-Acid Battery SOC
UDDS	Urban Dynamometer Drive Schedule
PR	Preliminary Rules
HEHV	Hydraulic Electric Hybrid Vehicle

Chapter 3
Hydraulic-Electric Hybrid Vehicle System Design

3.1 Introduction

In previous chapter, control strategy is optimized for the hydraulic-electric hybrid vehicle. The electrical range is improved significantly by hydraulic hybridization and control optimization. In this chapter, the detailed system design of the hydraulic-electric hybrid vehicle is introduced. The following sections show the details of the system design which includes the hydraulic system design, electric system design, and control code development.

3.2 Hydraulic System Design

3.2.1 Hydraulic system layout

The schematic diagram of the hydraulic-electric hybrid vehicle is shown in Figure 2.2. The hydraulic system is connected to the DC motor in a parallel configuration through a gear box. All the hydraulic components are connected together by hydraulic hoses as shown in Figure 3.1. The hydraulic system consists of hydraulic accumulator, hydraulic pump motor, oil reservoir, pressure sensors, low pressure manifold, oil filters and hydraulic valves.

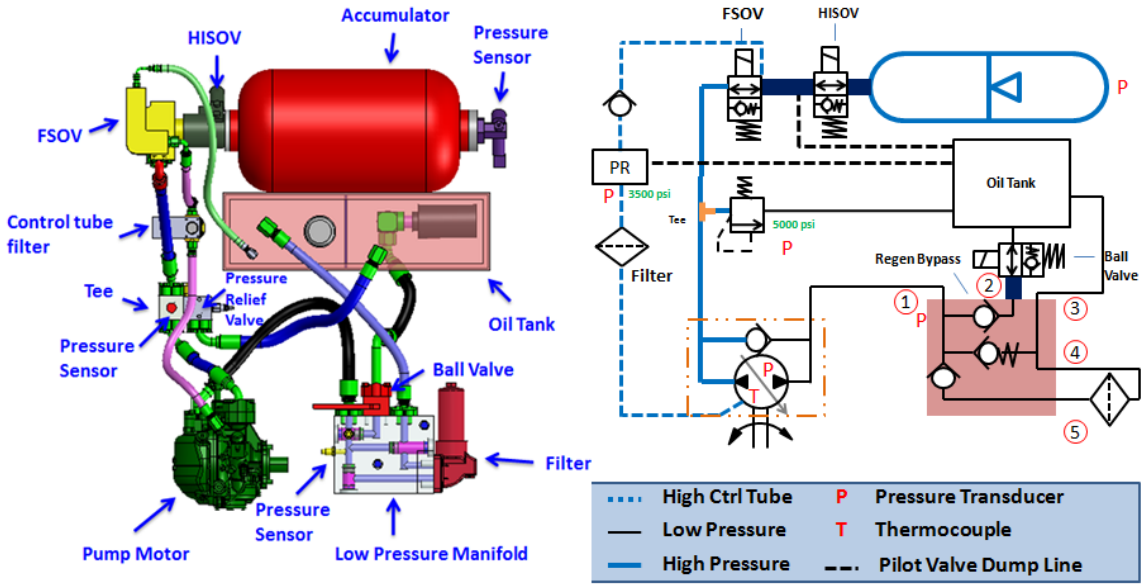

Figure 3.1 Hydraulic assembly in 3D (left) and hydraulic system layout (right).

The accumulator is mainly used to store the energy. The oil is pressurized into the accumulator by hydraulic pump. The hydraulic accumulator used here is a bladder-type accumulator and its components are shown in Figure 3.2. A nitrogen gas pressure sensor is installed on the one end of the hydraulic accumulator to monitor the pressure insider the accumulator and HISOV (High pressure shut off valve), and FSOV (Fast shut off valve) are installed on the other end of the accumulator to open or close the accumulator.

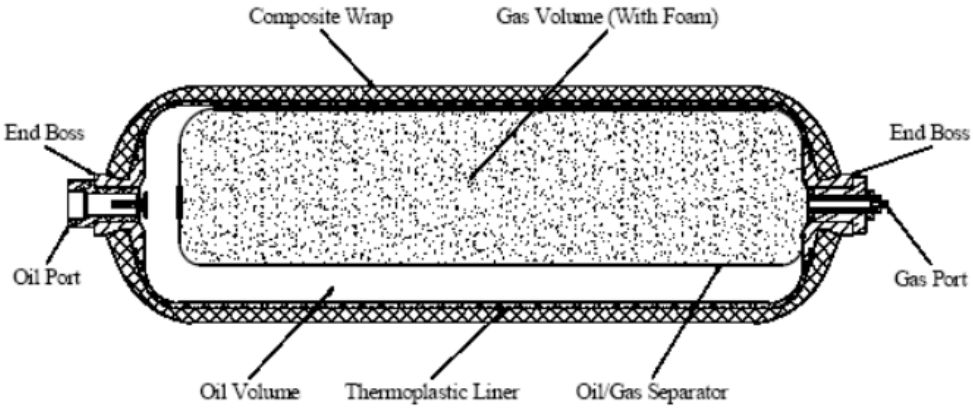

Figure 3.2 Bladder-type accumulator and its components [70]

Between the FSOV and HISOV, there is a small pilot high pressure hose. The pilot hose provides necessary high pressure oil for the pump motor displacement actuator during pump motor operation.

The high pressure line starts from the outlet of hydraulic accumulator, through HISOV, FSOV, and then goes to the high pressure union. The union connects the high pressure hose from hydraulic accumulator, the inlet port of hydraulic pump motor, and high pressure relief valve. The purpose of relief valve is to release the high pressure oil directly to the oil tank when the pressure of the oil exceeds certain dangerous level.

The hydraulic pump motor used in this study is a variable displacement bent axis type hydraulic pump motor as shown in Figure 3.3. It has a rotating cylinder containing parallel prisons arranged radially around the cylinder center line. The pump motor shaft is arranged at a variable angle to the cylinder axis. The shaft includes a flange with a mechanical connection to each piston. In pump mode, as the shaft rotates the pistons the hydraulic oil is sucked from the inlet port and pushed out from outlet put. In the motor mode, the high pressure oil pushes the pistons, and the shaft is therefore spun.

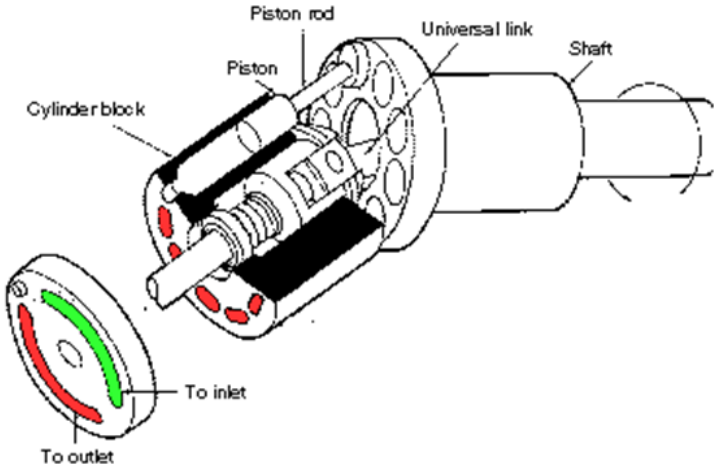

Figure 3.3 Bent-axis hydraulic pump motor[19]

The hydraulic pump motor used in this study has three main ports. The first port is the high pressure inlet port which connects to the high pressure oil line. The second port is the outlet port which connects to the low pressure manifold. And the third port is the actuator port which connects to the high pressure line from the oil port between HISOV and FSOV. The high pressure oil goes to the third port to enable the displacement control. The pump motor is installed on the reduction gear box as shown in Figure 3.4.

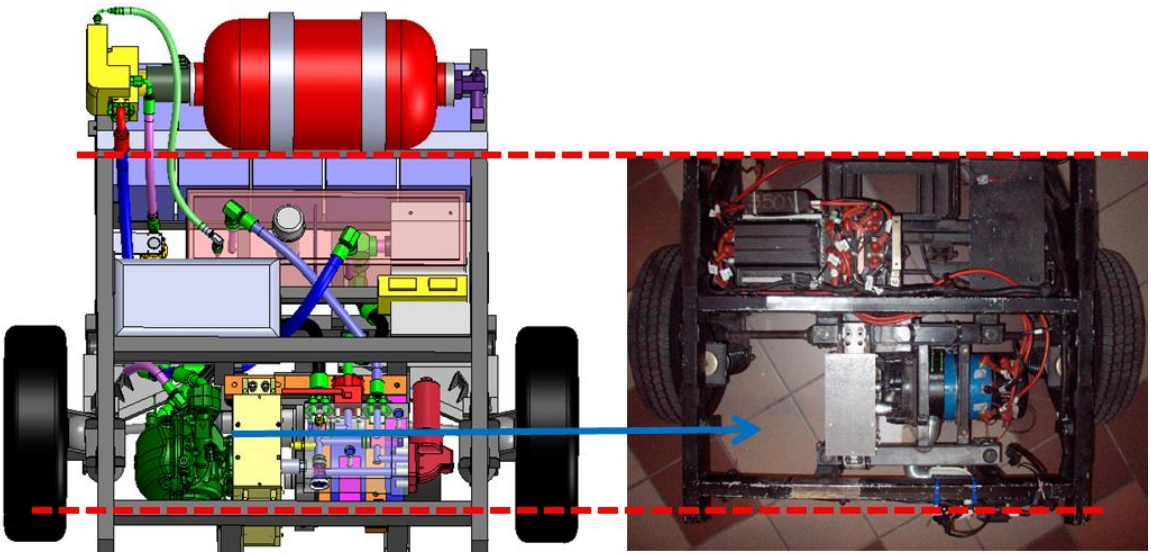

Figure 3.4 Hydraulic pump motor installation

There are two oil filters in the system. The first filter is in the line from accumulator to the pump motor actuator port. It cleans the oil going into the pump motor actuator. And the other filter is installed on the low pressure manifold, which cleans the oil from the pump motor to the oil tank.

Low pressure manifold is designed to include check valves and filter on the low pressure side of pump motor. The detailed design of the manifold is shown in Figure 3.5. The manifold contains 3 check valves, 1 pressure sensor and 1 oil filter.

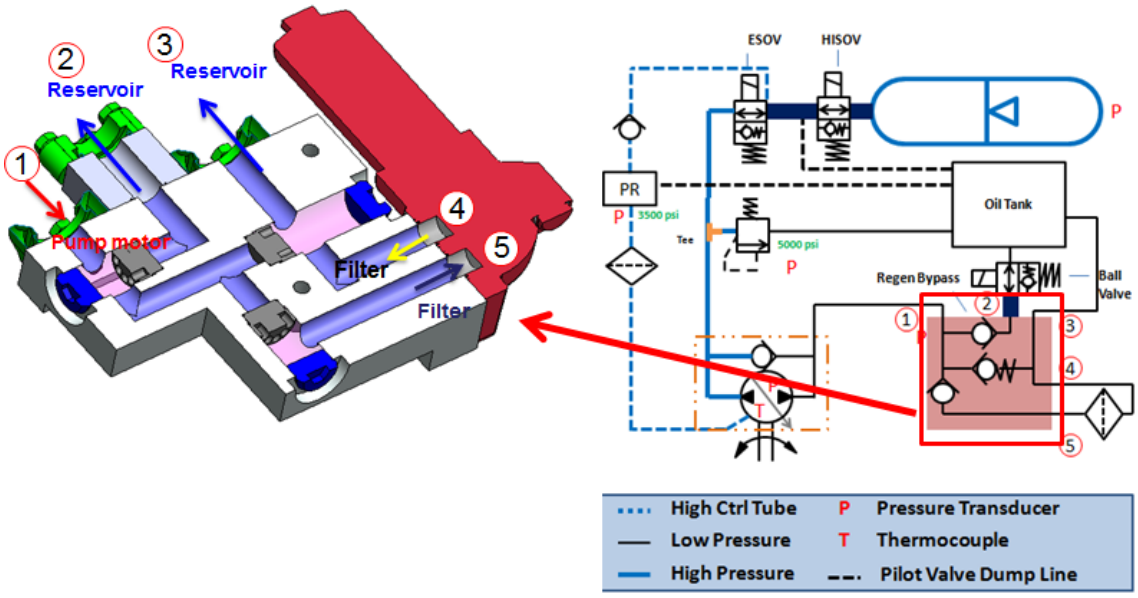

Figure 3.5 Low pressure hydraulic manifold

The oil tank is specially designed as shown in Figure 3.5. It has 3 inlet ports connecting to pilot valve, low pressure manifold, and pressure relief valve. One outlet port is on the bottom of the oil tank. A inner filter is installed on the suction port.

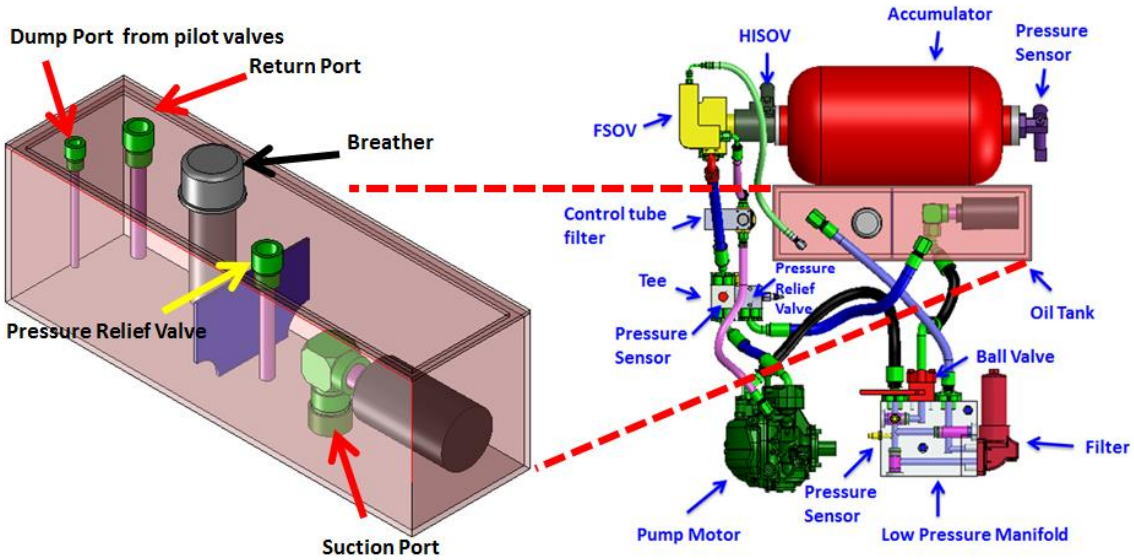

Figure 3.6 Oil tank design

The oil tank is designed to be placed in between battery pack and the stock DC motor controller as shown in Figure 3.7.

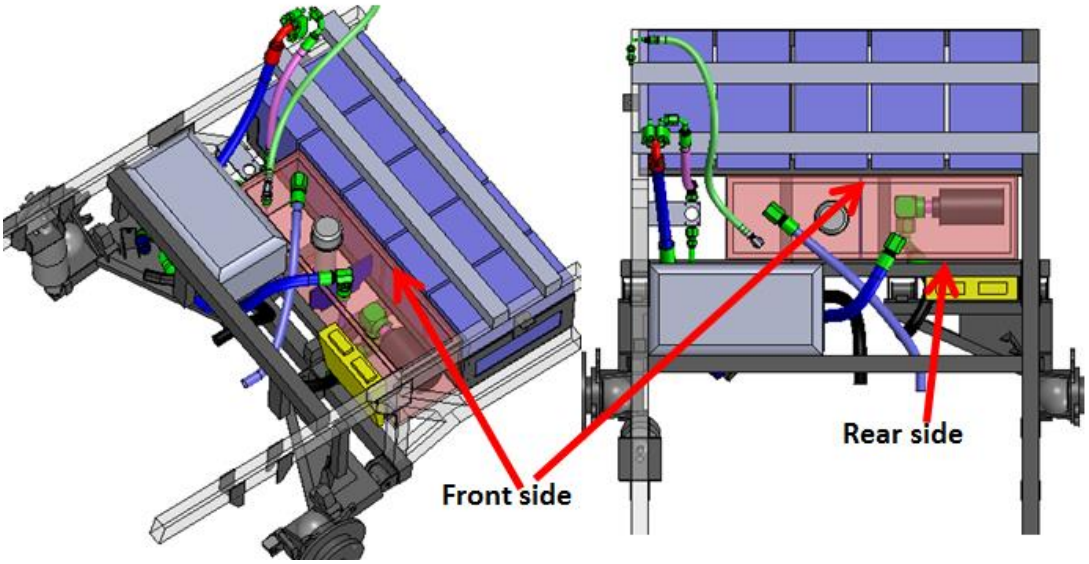

Figure 3.7 Oil tank position

A reduction gear box is designed to gain the right gear ratio between DC motor and hydraulic pump motor. As shown in Figure 3.8, the pump motor is installed on the reduction gear box.

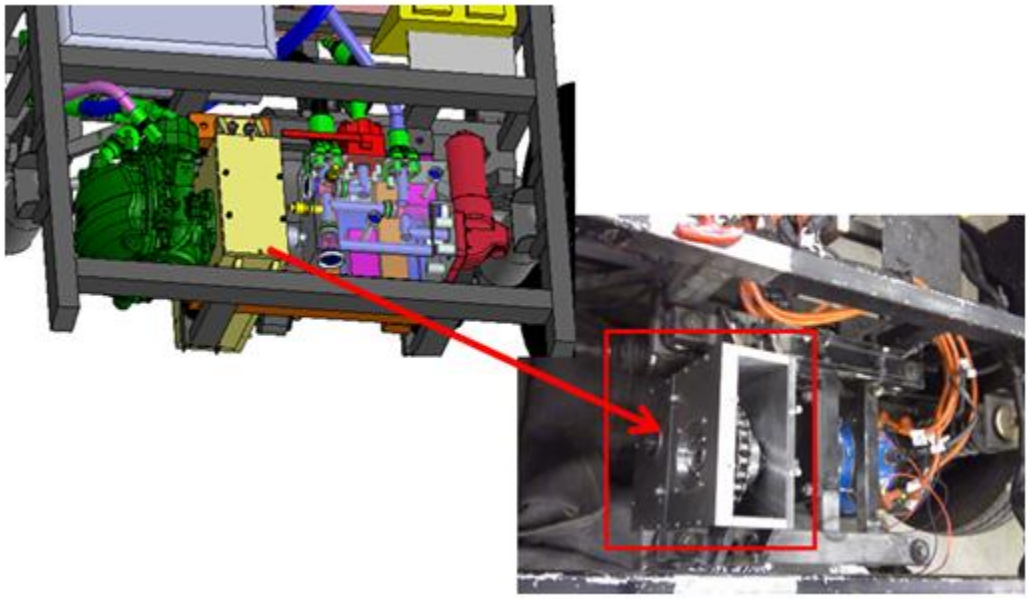

Figure 3.8 Pump motor and reduction gear box

After the hydraulic system is designed, the parts are assembled together as shown Figure 3.9.

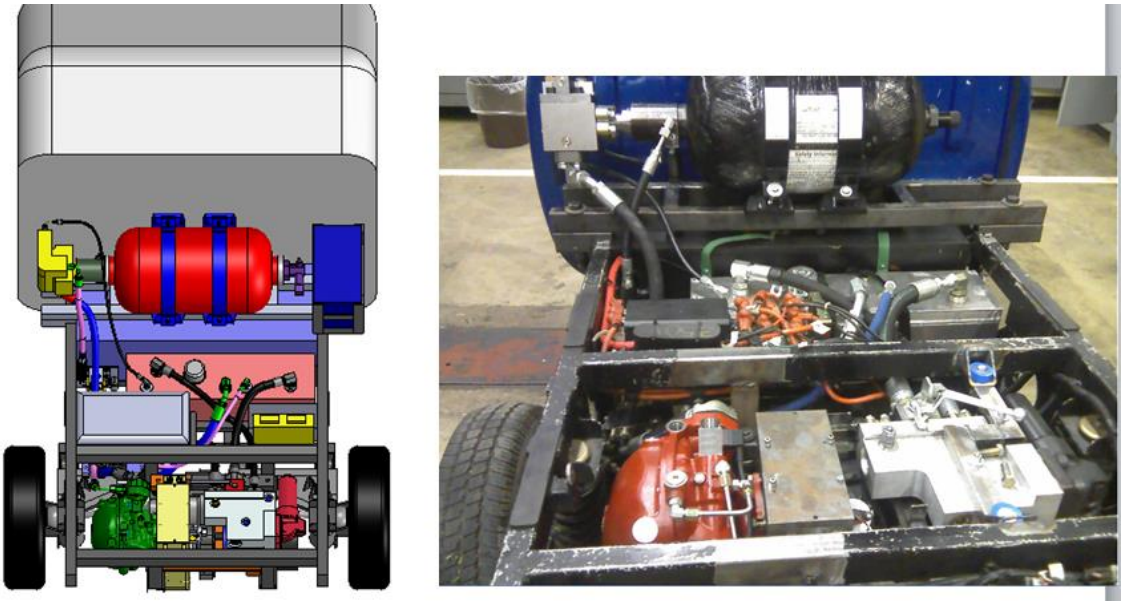

Figure 3.9 Hydraulic system after packaging

The energy capacity of the hydraulic accumulator depends on several factors, such as, accumulator size, pre-charge pressure, maximum pressure, etc. In order to better utilize the capacity of the accumulator and save space for the vehicle, the energy capacity of the accumulator under different pre-charge pressure, and accumulator sizes is investigated.

As shown in Figure 3.10, the left Y axis shows the energy capacity of the accumulator, and the bottom X axis shows different pre-charge pressure. The maximum pressure in the accumulator is fixed to be 5000 psi due to the safety concern. Different energy capacities are plotted with different colors. The right Y axis shows the kinetic energy of the vehicle, and the upper X axis shows the vehicle speed. The volume of the hydraulic accumulator used in this study is chosen to be 6 gallon which has enough energy capacity to capture the kinetic energy from the vehicle at 35 mph (maximum speed).

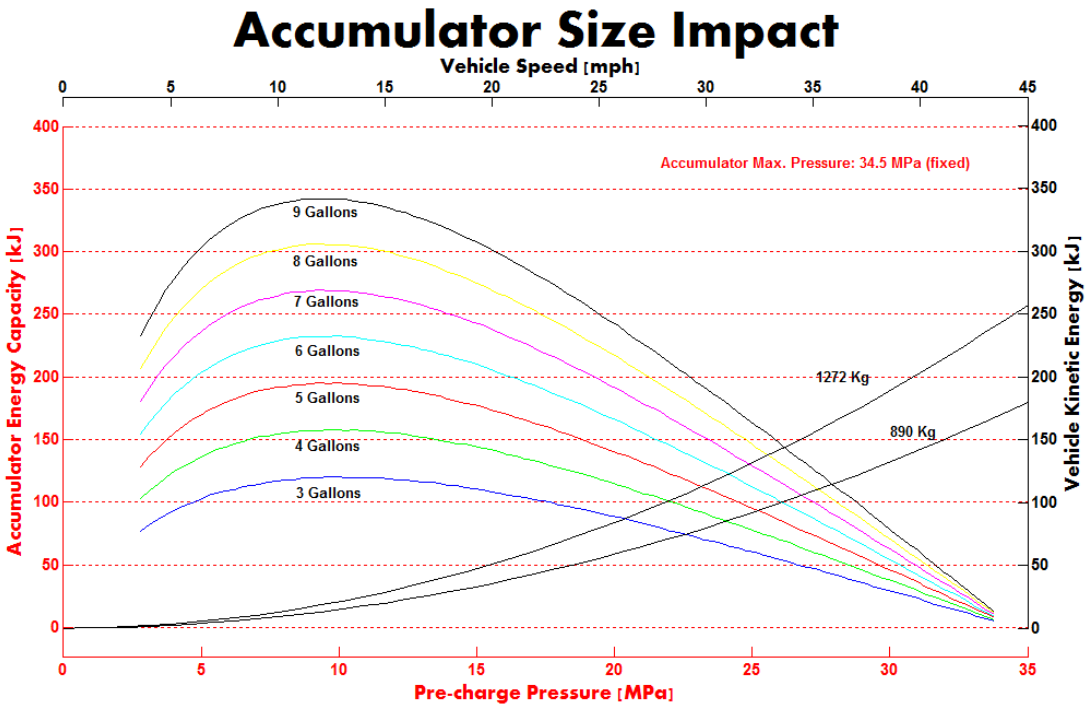

Figure 3.10 Accumulator energy capacity and vehicle kinetic energy

3.2.2 Hydraulic operating modes

The hydraulic system is connected to the existing propulsion system. During the acceleration and brake, hydraulic system is used to assist DC motor to launch or vehicle brake system to go regenerative brake. The central controller monitors the pressure in the hydraulic system and vehicle status, and controls the hydraulic system during different events. In the following section, different events are introduced and the control sequences in different events are explained.

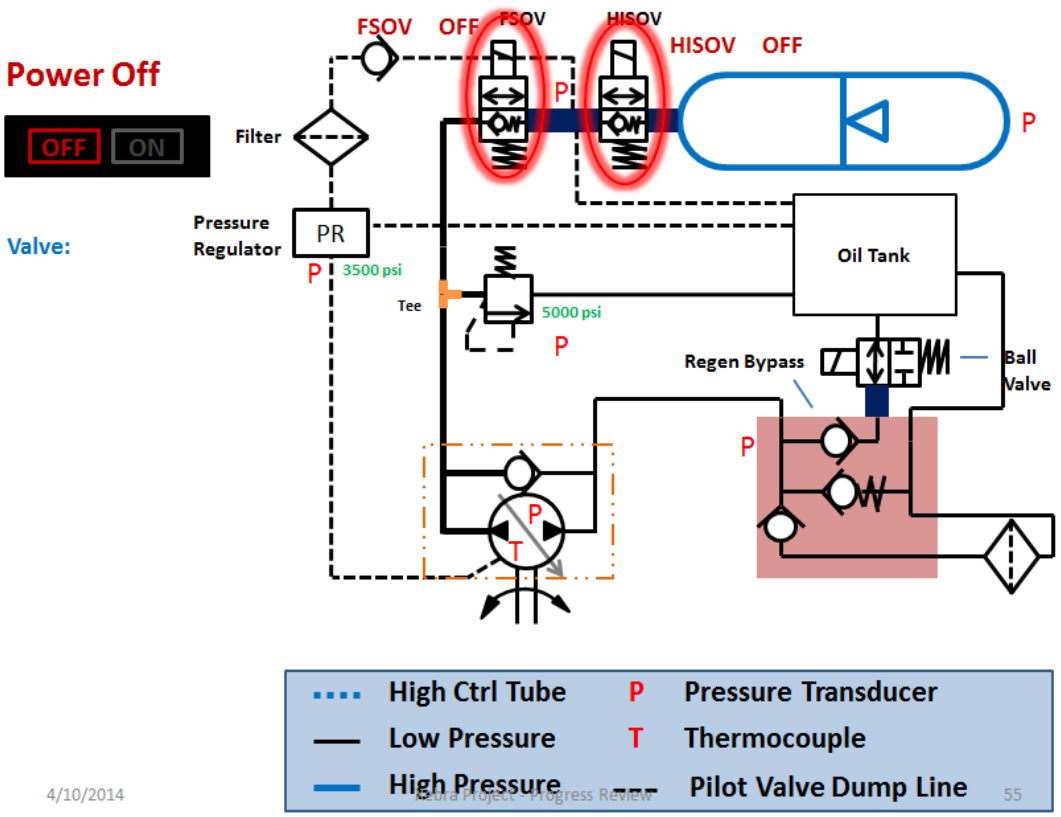

Figure 3.11 Power off mode

Figure 3.11 shows the hydraulic system status in the power off mode. In the power off mode, the vehicle is turned off. And FSOV and HISOV for the accumulator are also shut off to close the accumulator. All the hydraulic lines become low pressure. The hydraulic pump motor is not controllable during power off mode due to lack of pressure to the actuator. The vehicle wheel can spin freely, because the pump motor has a build-in idling bypass check valve. The residual oil in the pump motor will circulate through the bypass channel inside the pump motor if the vehicle wheel is rotating.

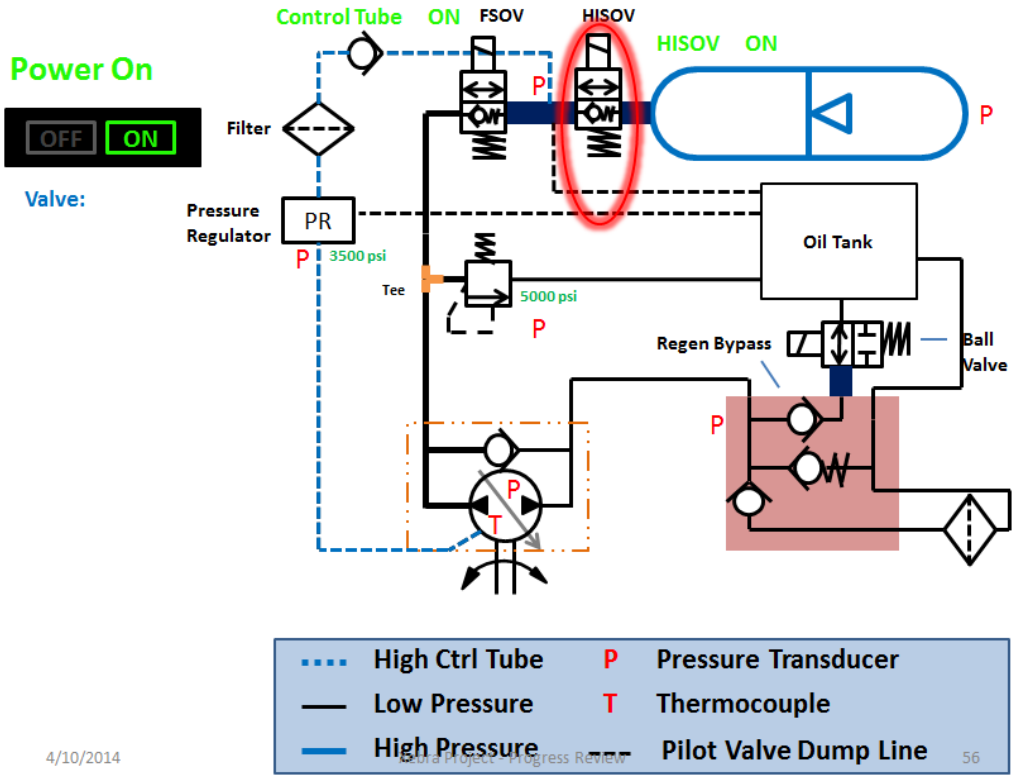

Figure 3.12 Power on mode

When the power is just turned but not driven yet, the HISOV is switched on as shown in Figure 3.12. The high pressure oil comes out from the accumulator, and goes to the pilot line which is directly connected to the actuator port of the pump motor. Therefore, the pump motor displacement can be controlled. The controller can send out command to set the displacement of the hydraulic pump motor based on the throttle pedal. During power on stage, the throttle pedal is not pressed yet, the controller will send 0 displacement signal to the pump motor. Therefore, the hydraulic pump motor will have 0 displacement which means neutral of the hydraulic system.

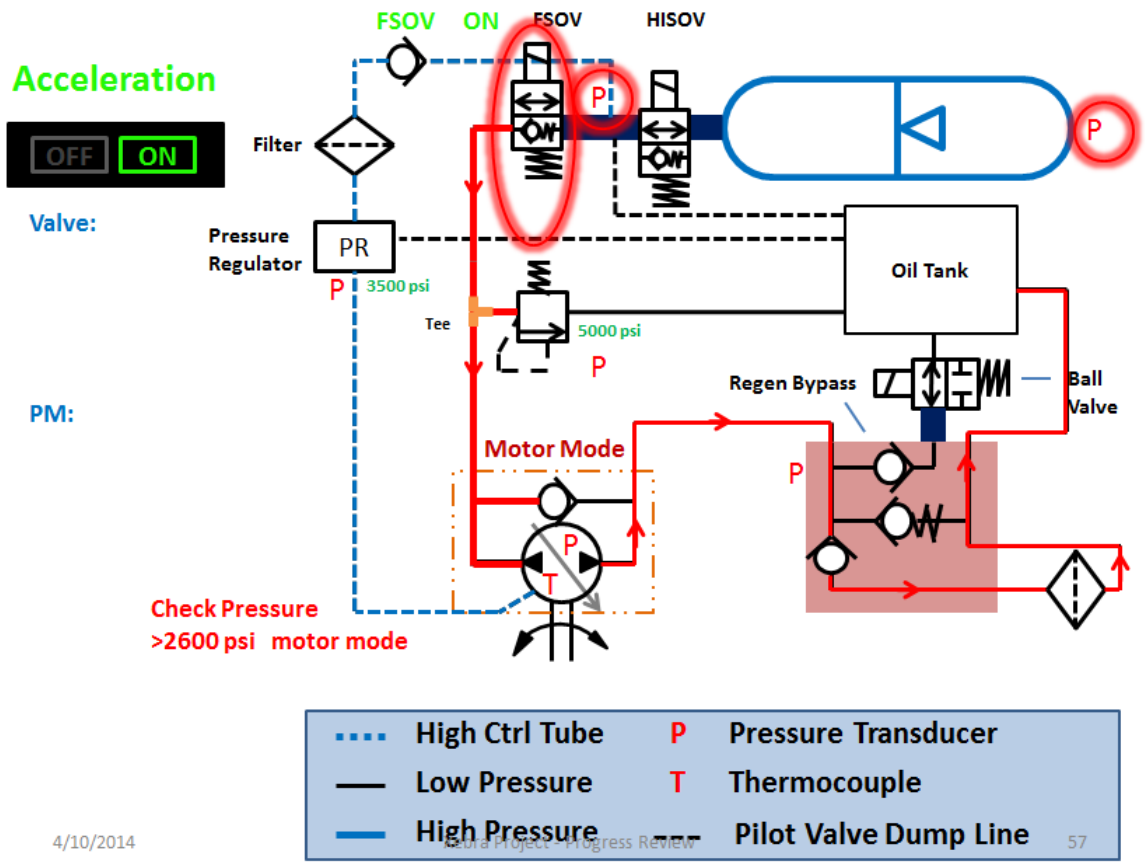

Figure 3.13 Acceleration mode

When the driver presses the throttle pedal, the vehicle starts to accelerate. The controller will send out the signal to switch on the FSOV. The high pressure oil goes through HISOV and FSOV to the hydraulic pump motor. The hydraulic pump motor is working under motor mode. The hydraulic motor outputs the torque through the gear box to the wheel. The oil comes out from the hydraulic motor and goes to the low pressure manifold. The filter installed on the manifold will clean the oil before the oil goes to the oil tank.

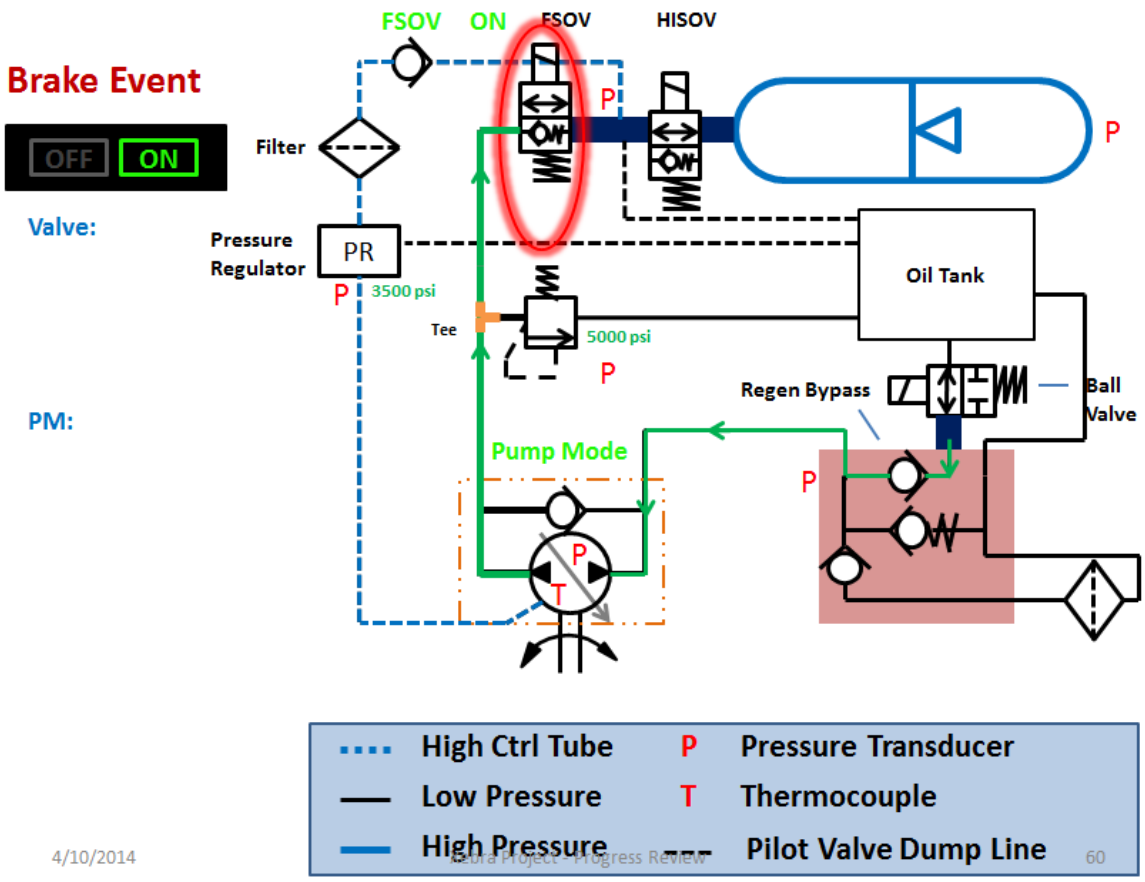

Figure 3.14 Regenerative brake mode

When the driver presses the brake pedal, the controller sends out the signal to set the pump motor to be negative displacement, which means the hydraulic pump motor enters pump motor. The oil will be pumped from low pressure oil tank to the high pressure accumulator. The pressure difference applied on the hydraulic pump will generate a brake torque to the wheel. The pumped oil is stored in the accumulator for the next acceleration.

All the hydraulic valves, pump motor, and sensors are connected to the central controller. The central controller sends out the commands in each event based on the measurements of vehicle speed, accumulator pressure, throttle pedal position and brake pedal position.

3.3 Electric System Design

3.3.1 Stock electrical system

The electric system in the stock vehicle is shown in Figure 3.15. The existing electric system includes high voltage (72V) power from the battery pack and low voltage power (12V) from 1 battery under the hood. The 12V circuitry sends out the control signals to the 72V circuitry. The throttle pedal is a special potential meter. The voltage signal from the potential meter is fed to the DC motor controller which will adjust 72V power to the DC motor through PWM.

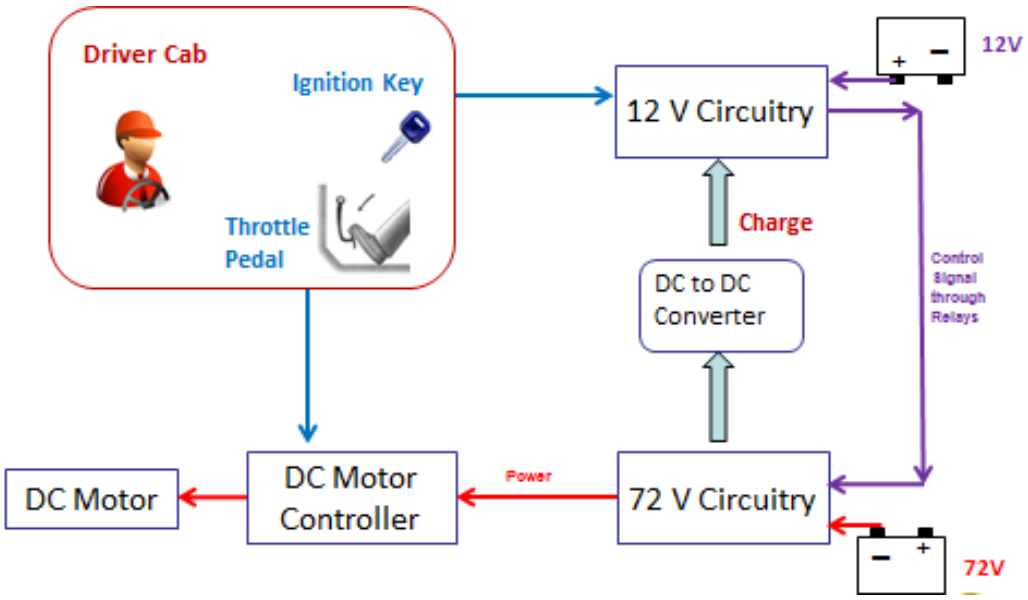

Figure 3.15 Electric system in the stock vehicle

3.3.2 Modified electric system

In order to integrate the new hydraulic system to the stock vehicle, the existing electrical system is modified as shown in Figure 3.16. The Pi M460 controller is used as the central controller for the hybrid vehicle. The 12V circuitry provides the power to the M460 controller.

The controller collects all the signals from different sensors, such as throttle pedal, key position, vehicle speed, pressure in hydraulic system, and sends out the commands to different actuators in hydraulic system and electric system.

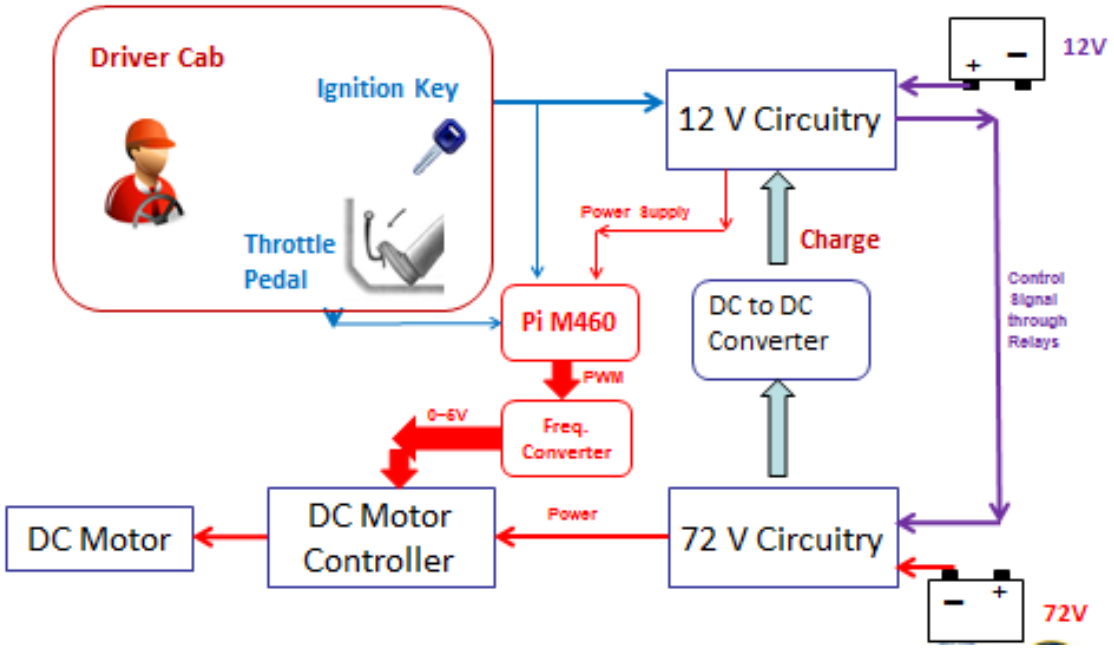

Figure 3.16 Modified electric system

3.4 Control System Design

3.4.1 Code architecture and SIL setup

The control system is developed in the software in the loop environment. The hybrid vehicle model developed in the previous chapter is used as the baseline for the control code development. In order to test the code in Matlab Simulink, the existing hybrid vehicle model is augmented with details, such as, hydraulic pressure sensors, valves, and actuators.

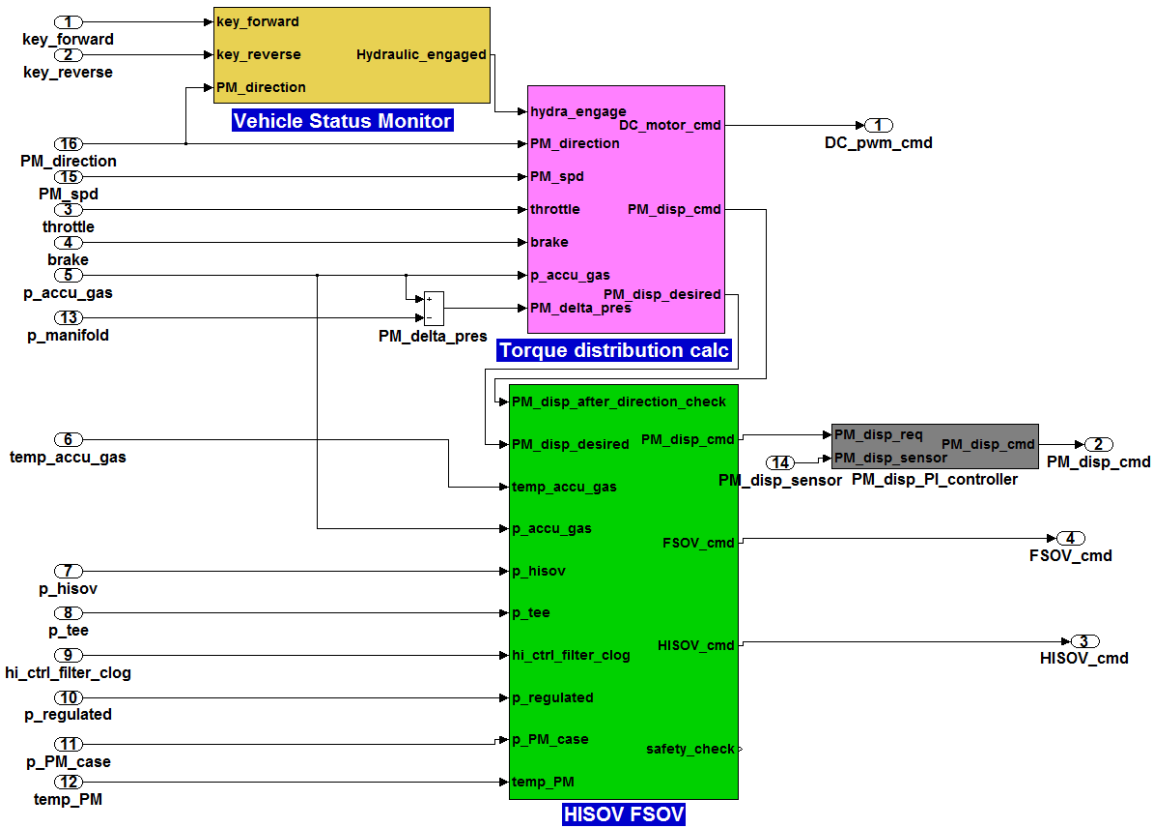

Figure 3.17 Control system in Simulink

The control system has three main modules. The first module is the vehicle status monitor. This module is responsible for monitoring the key position, such as, forward or reverse modes. The vehicle status monitor module determines the whether or not to engage the hydraulic system. The information from the status monitor module is sent to the toque distribution calculation module. This module is used to calculate the torque distribution between DC motor and hydraulic pump motor. The third module is the output signal processing module for the HISOV and FSOV. The calculated torque distribution message will be passed to this module, and the signals for HISOV and FSOV will be sent out from this module.

The torque distribution calculation module is the most important part in the control system. It includes the effects of different factors on the hydraulic pump motor displacement and DC

motor command. As shown in Figure 3.18, the module calculates the torque distribution for DC motor and hydraulic pump motor based on the input from throttle pedal, brake pedal and signals from pressure and speed sensors.

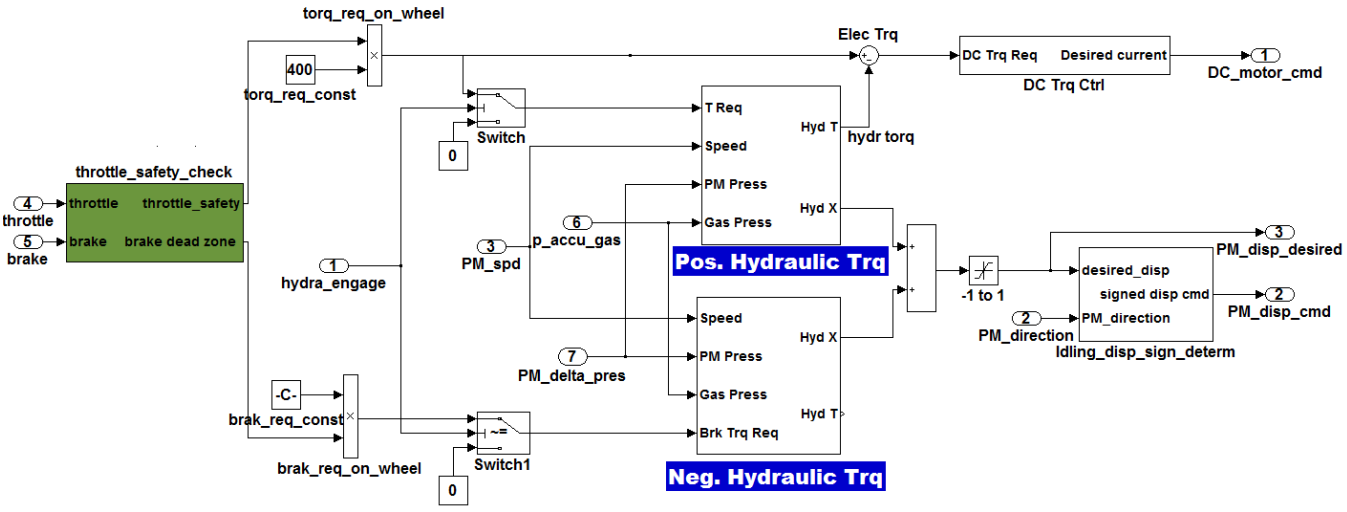

Figure 3.18 Torque distribution calculation

3.5 Summary

This chapter introduces the hardware design of hydraulic-electric hybrid vehicle. It includes the hydraulic system design, electric system design and control system design. The hydraulic system is first designed. Based on the hydraulic system, the operating modes are developed. The existing electric system in the stock vehicle is studied, and modified in order to integrate the hydraulic system to the stock vehicle. The control system is developed in software in the loop environment, and failure modes are tested before implementation.

Chapter 4
Side Reaction Coupled Degradation Model Development

4.1 Introduction

A substantial amount of work has gone into understanding capacity fade through experiments and theoretical/numerical studies [71-80]. Ramadass *et al*.[81] carried out a complete capacity fade analysis for the Sony 18650 cells after hundreds of cycles. They divided the capacity fade into rate capability loss as well as primary and secondary active material losses. However, they proposed no model to quantitatively explain the capacity fade due to different mechanisms. Safari *et al*.[82] proposed a multimodal physics-based aging model to predict the capacity fade for Li-ion batteries. They assumed that capacity fade stems mainly from solid electrolyte interphase (SEI) growth on the anode, and that lithium ion consumption during SEI growth was the main contributor to cycling degradation. Zhang *et al*.[13] developed a single-particle model which they calibrated against the cycling data to study the parameter trajectories. They suggested that there were probably different stages of capacity fade in the lithium ion battery. However, they proposed no degradation model to quantitatively study the degradation process.

The studies above have attempted to elucidate capacity fade by focusing on specific mechanisms, not by regarding all the key mechanisms together. Because each mechanism is coupled to each other, it is important to consider all of them and their interactions simultaneously. In this way, the whole life of a battery cell can be predicted, and its pattern can be analyzed. From this point of view, an attempt is made in this study to develop a physics-based model to predict the capacity fading process. There is a number of degradation mechanisms associated with cell degradation[12]. The most known processes leading to capacity fade in the Li-ion

batteries are SEI growth and manganese deposition on the anode electrode, as well as manganese dissolution, electrolyte oxidation and salt decomposition on the cathode electrode. Quantifying all these degradation processes will improve prediction of cell capacity during operations.

The battery system considered in this study is a graphite/LMO full cell, which consists of a 150 μm anode, a 30 μm separator and a 110 μm cathode in 1 M $LiPF_6$ ethylene carbonate (EC) / dimethyl carbonate (DMC) electrolyte. In order to explore the long-term degradation pattern, each side reaction is coupled to the electrochemical cell-level model. This model consists of two levels: the particle level and cell level. The particle-level modeling describes side reactions on both anode and cathode electrodes. The cell-level electrochemical model based on porous-electrode theory describes the lithium ion transportation process during charge and discharge[83]. The two levels are coupled through the local reaction current based on charge conservation.

4.2 Model Development

The following sections introduce details of the modeling work and are divided into three parts. The first part introduces side reactions on the anode surface, which are mainly responsible for the cyclable lithium ion loss. The second part focuses on the side reactions on the cathode, which lead to the active material loss and capacity fade of the cathode. Finally, the side reactions are coupled to a cell-level electrochemical model for studying cell degradation.

4.2.1 Part I: modeling of side reaction at anode

Several side reactions occur on the surface of the anode particles. Examples of these include SEI formation, metallic manganese deposition[55] and the reduction of a small amount of H+ generated from solvent oxidation and salt decomposition[38]. A particle-level model is developed to describe the side reactions when the SEI layer is growing. The impact of the SEI layer on the side reactions is included in the model. As shown in Figure 4.1, the anode particle is

covered by a thin SEI layer which can vary from a few nm[84] to hundreds nm [48] depending on the cycling conditions and the compositions of the system.

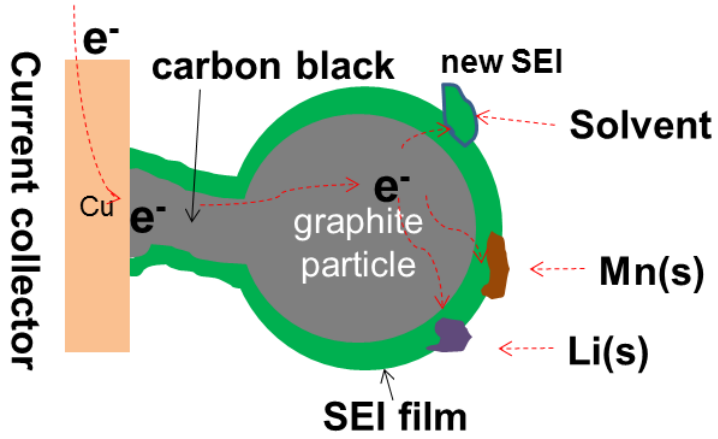

Figure 4.1 A schematic diagram of side reactions on anode, including SEI formation, Mn deposition, and Li plating

In a fresh cell the SEI layer is not yet formed, so the side reaction rate is controlled only by Butler-Volmer equations which consider the reactant concentration and electric potential[85]. As the SEI grows thicker, the side reactions are slowed down because the electrolyte diffusion through the SEI film to the graphite surface is limited[82]. The SEI film growth curves from numerical simulations based on detailed chemistry model[86] and solvent-diffusion model[82], and also the experimental measurements based on spectroscopic ellipsometry[87] clearly show a decaying SEI growth rate as SEI film thickness increases. The decaying growth rate with respect to the thickness of the SEI film can be well approximated by an exponential decay function of

$$R(\delta) \approx e^{-\lambda\delta}, \tag{4.1}$$

where $R(\delta)$ is the limiting factor which ranges from 0 to 1, δ is the thickness of the SEI layer and λ is the limiting coefficient.

The side reation rates limited by the SEI layer can be expressed by

$$i_{side} = R(\delta) \cdot i^{*}_{side} = e^{-\lambda_{side}\delta} \cdot i_0^{side} \left\{ \exp\left[\frac{\alpha_a^{side} nF}{RT}(\phi - \phi_{eq})\right] - \exp\left[-\frac{\alpha_c^{side} nF}{RT}(\phi - \phi_{eq})\right] \right\}, \tag{4.2}$$

where i_{side} is the side reaction limited by the SEI layer, i_{side}^{*} is the original side reaction rate without SEI limitation, λ_{side} is the limiting coefficient of the side reaction, i_0^{side} is the exchange current density, α_a^{side} is the anodic charge transfer coefficent, α_c^{side} is the cathodic charge transfer coeffcient, n is the number of electrons involved in the reaction, F is the Faraday constant, R is the gas constant, T is the absolute temperature, ϕ is the electric potential and ϕ_{eq} is the equlibirum potential for the side reaction.

SEI formation

There is continuous SEI formation reaction between the lithiated graphite and the electrolyte solvent[88, 89]. This continuous SEI growth leads to a gradual consumption of the cyclable lithium and an increase in electrode impedance upon cycling[90, 91].

The electrolyte reduction reactions occurring on the graphite surface are very similar to those on the lithium metal[92]. Aurbach *et al.*[92] stated that the lithium ethylene dicarbonate $(CH_2OCO_2Li)_2$ and ethylene gas resulting from a one-electron reduction process of EC are the dominant products in the SEI formation. Yang *et al.*[93] investigated the SEI film composition in an EC-based electrolyte using Fourier transform infrared and mass spectroscopy. They observed that the passive SEI film consists of chiefly $(CH_2OCO_2Li)_2$. Wang *et al.*[94] carried out the high level density functional calculations, and concluded that the reductive decomposition of EC initially proceeds through an ion-pair intermediate. It then homiletically cleaves via an 11.5 kcal/mol barrier to generate a radical anion, which undergoes a secondary reaction by barrier-free self-dimerizing. Based on the above findings, Safari *et al.*[82] developed the SEI growth model in which lithium ethylene dicarbonate $(CH_2OCO_2Li)_2$ is considered to be the main

component of the SEI layer and the SEI formation process is expressed in the following equations.

$$EC + e^{-}(graphite) \rightarrow EC^{-} \tag{4.3}$$

$$EC^{-} + EC^{-} \rightarrow (O_2CO)^{-}(CH_2)_2(O_2CO)^{-} + C_2H_4 \uparrow \tag{4.4}$$

$$EC^{-} + EC + e^{-}(graphite) \rightarrow (O_2CO)^{-}(CH_2)_2(O_2CO)^{-} + C_2H_4 \uparrow \tag{4.5}$$

$$(O_2CO)^{-}(CH_2)_2(O_2CO)^{-} + 2Li^{+} \rightarrow Li^{+}(O_2CO)^{-}(CH_2)_2(O_2CO)^{-}Li^{+} \tag{4.6}$$

The reaction rate of the radical anion formation process at the interface of the graphite and the electrolyte, i_{SEI}^{*} , is expressed by [82]

$$i_{SEI}^{*} = -Fk_{SEI}c_{EC}\exp[-\frac{\alpha_c^{SEI}F}{RT}(\phi_1 - \phi_2)], \tag{4.7}$$

where k_{SEI} is the reaction rate constant of SEI, c_{EC} is the solvent concentration, α_c^{SEI} is the cathodic charge transfer coeffcient, $\phi_1$is the solid-phase potential, and ϕ_2 is the solution-phase potential.

As mentioned above, as the SEI grows thicker, the reaction rate slows down. The modified SEI side reaction rate, i_{SEI} , is given by

$$i_{SEI} = R(\delta) \cdot i_{SEI}^{*} = -e^{-\lambda_{SEI}\delta}Fk_{SEI}c_{EC}\exp[-\frac{\alpha_c^{SEI}F}{RT}(\phi_1 - \phi_2)]. \tag{4.8}$$

The growth rate of the SEI layer due to the accumulation of lithium ethylene dicarbonate is related to the side-reaction current density by [82]

$$\frac{d\delta}{dt} = -\frac{i_{SEI}}{2F}\frac{M_{SEI}}{\rho_{SEI}} \tag{4.9}$$

where t is time, M_{SEI} is the molecular weight of SEI, and ρ_{SEI} is the SEI density.

Overcharge phenomena

Lithium deposition as one important side reaction is expected to occur in the lithium ion battery under abuse conditions, such as adverse charging conditions, accidental overcharging or

low temperature charging[95, 96]. Lithium deposition not only lead to the cyclable lithium loss, but also is considered as a safety hazard due to the high reactive nature of metallic lithium with electrolyte [97, 98].

The main side reaction on the negative electrode surface during overcharge is given by the following equation.

$$Li^+ + e^- = Li(s) \tag{4.10}$$

Pankaj *et al.*[50] proposed a deposition model to describe the charge transfer kinetic controlled lithium deposition process in a Butler Volmer expression

$$j_{Li\_dep0} = -i_{0,Li\_dep}\left\{\exp\left[\frac{\alpha_{c,Li\_dep}F}{RT}(\phi_1-\phi_2)\right] - \exp[-\frac{\alpha_{c,Li\_dep}F}{RT}(\phi_1-\phi_2)]\right\} \tag{4.11}$$

Pankaj further simplified the reaction rate equation to a cathodic Tafel expression based on the assumption that the deposition reaction is considered to be irreversible or the amount of lithium deposited is very small and reacts quickly with the solvent. The simplified equation is shown below.

$$\mathrm{j}_{Li\_dep0} = -i_{0,Li\_dep}\exp\left[-\frac{\alpha_{c,Li\_dep}F}{RT}(\phi_1-\phi_2)\right] \tag{4.12}$$

The lithium deposition is also considered to be affected by the SEI thickness[95]. As the SEI get thicker, the lithium deposition is reduced due to the difficulty in getting electrons. The limitation effect is introduced to the reaction rate, the modified equation is shown below.

$$j_{Li\_dep} = \mathrm{R}\cdot\mathrm{j}_{\mathrm{Li\_dep0}} = -k_{eff}\frac{1}{\delta}i_{0,Li\_dep}\exp\left[-\frac{\alpha_{c,Li\_dep}F}{RT}(\phi_1-\phi_2)\right] \tag{4.13}$$

Manganese deposition and acid reduction

The deposition of Mn particles on the lithium metal after cycling was confirmed through EDX analysis[41, 99]. Komaba *et al.*[40] conducted cycling experiments in 1 M $LiClO_4$

EC/DEC solution where Mn was added before and during the cycling. The discharge capacity will severely decrease due to Mn^{2+} reduction on the anode surface. The Mn deposition is believed to decrease the cyclable lithium ions because manganese deposition consumes electrons that are supposed to be coupled to lithium ions during the intercalation process. This side reaction is expressed by

$$Mn^{2+} + 2e^{-} \rightarrow Mn(s), \tag{4.14}$$

which implies that Mn deposition on the graphite anode will reduce the amount of cyclable lithium ions in the cell.

Because the reaction is controlled by electrical charge transfer, the Mn deposition process follows the Butler Volmer expression[38], in the form of

$$i^{*}_{Mn\_dep} = -Fk_{Mn\_dep}c_{Mn^{2+}} \exp\left[-\frac{\alpha_c^{Mn\_dep}2F}{RT}(\phi_1 - \phi_2)\right], \tag{4.15}$$

where $i^{*}_{Mn\_dep}$ is the Mn deposition rate, k_{Mn_dep} is the reaction rate constant, $c_{Mn^{2+}}$ is the Mn^{2+} concentration, and $\alpha_c^{Mn\_dep}$ is a cathodic charge transfer coeffcient in the process.

The Mn deposition is also considered to be affected by the SEI thickness. As the SEI grows thicker, the Mn deposition rate should decrease, giving

$$i_{Mn\_dep} = R(\delta) \cdot i^{*}_{Mn\_dep} = -e^{-\lambda_{Mn\_dep}\delta}Fk_{Mn\_dep}c_{Mn^{2+}} \exp\left[-\frac{\alpha_c^{Mn\_dep}2F}{RT}(\phi_1 - \phi_2)\right]. \tag{4.16}$$

The protons generated from electrolyte oxidation and salt decomposition could also be consumed at the anode surface via [12]

$$H^{+} + e^{-} \rightarrow \frac{1}{2}H_2(g). \tag{4.17}$$

The reaction is controlled by electrical charge transfer and the reaction rate can be expressed by

$$i_{H_2} = R(\delta) \cdot i^*_{H_2} = -e^{-\lambda_{H_2}\delta} F\, k_{H_2} c_{H^+} \exp\left[-\frac{\alpha_c^{H_2} F}{RT}(\phi_1 - \phi_2)\right], \tag{4.18}$$

where k_{H_2} is the reaction rate constant, c_{H^+} is the H^+ concentration, and $\alpha_c^{H_2}$ is a cathodic charge transfer coeffcient.

When the cell is being discharged, the potential difference $\phi_1 - \phi_2$ is large, giving a very small reaction rate. Therefore, we assume that there is no reduction/oxidation reactions for H^+ and Mn^{2+} during discharge[38].

4.2.2 Part II: modeling of side reaction at cathode

Important side reactions in the cathode electrode include electrolyte oxidation, salt decomposition, Mn dissolution [100, 101], and cathode particle fracture[42, 102, 103]. Further, these side reactions are coupled with each other. The protons generated as a result of solvent oxidation and salt decomposition play a key role in Mn dissolution.[35] The generated protons attack the active material on the cathode surface. This Mn dissolution process can be expressed by [35, 38, 104]

$$4H^+ + 2LiMn_2O_4 \rightarrow 2Li^+ + Mn^{2+} + \frac{3}{2}Mn_2O_4 + 2H_2O. \tag{4.19}$$

The reaction rate is controlled by the proton concentration in the cathode because of the high content of LMO in the cathode and the small concentration of protons. Part of Mn^{2+} forms composites such as MnF_2 in the SEI layer on the cathode surface,[100] the dissolved Mn^{2+} is hypothesized to be a fraction of the reaction product, and is expressed by

$$i_{Mn\_dis} = f_{Mn\_dis} i_{Mn\_react} = f_{Mn\_dis} F k_{dis} c_{H^+}, \tag{4.20}$$

where i_{Mn_dis} is the Mn dissolution rate, f_{Mn_dis} is the fraction coefficient, i_{Mn_react} is the reaction rate, and k_{dis} is the reaction rate constant for the acid attack on the active material.

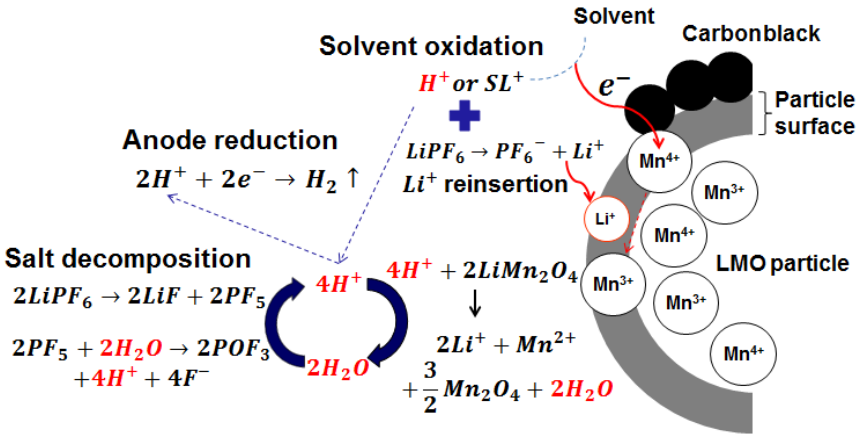

Figure 4.2 Side reactions on cathode, including salt decomposition, solvent oxidation, and Mn dissolution

The protons originate from two main sources. The first source is solvent oxidation,[35, 38, 104]

$$Solvent \xrightarrow{oxidation} SL_o + H^+(or\ SL^+) + e^-, \tag{4.21}$$

where SL_o and SL^+ represent the solvent oxidation products. The reaction is controlled by electrical charge transfer, and the solvent oxidation rate per volume, j_{oxid} , can be expressed by the Butler-Volmer equation[38]

$$j_{oxid} = a_c i_0^{sol}\left\{\exp\left[\frac{\alpha_a^{sol}F}{RT}\eta_{oxid}\right] - \exp\left[-\frac{\alpha_c^{sol}F}{RT}\eta_{oxid}\right]\right\}, \tag{4.22}$$

$$\eta_{oxid} = \phi_1 - \phi_2 - U_{oxid}^{eq}, \tag{4.23}$$

where a_c is the surface area per unit volume for the solvent oxidation, i_0^{sol} is the exchange current density, α_a^{sol} is the anodic charge transfer coefficient, α_c^{sol} is the cathodic charge transfer coefficient, and $U_{oxid}^{eq}$is the equilibrium potential of the side reaction.

An anodic Tafel expression can be used to describe the rate if the decomposition reaction is considered irreversible, where

$$j_{oxid} = a_c i_0^{sol}\exp\left(\frac{\alpha_a^{sol}F}{RT}\eta_{oxid}\right). \tag{4.24}$$

The proton generation rate per volume by solvent oxidation is assumed to be a fraction of the oxidation current,

$$j_{H^+}^{oxid} = f_{H^+} \cdot j_{oxid} \,, \tag{4.25}$$

where f_{H^+} is a fraction coefficient.

The surface area for the solvent reaction should be adjusted according to the carbon content since solvent oxidation occurs mostly on the surface of the conductive carbon black.[105] We assume that a_c is related to the carbon content X_c% (weight percentage) by

$$a_c = \frac{X_c}{X_c^{ref}} a_c^{ref} \,, \tag{4.26}$$

where X_c^{ref} represents the carbon content for a preset value, and a_c^{ref} is the value of a_c corresponding to the preset carbon content, X_c^{ref} .

The other source for the proton is the decomposition of $LiPF_6$, [101]

$$LiPF_6 \rightarrow LiF + PF_5, \tag{4.27}$$

where the product PF_5 reacts with water to form HF, namely

$$PF_5 + H_2O \rightarrow POF_3 + 2HF. \tag{4.28}$$

The proton production rate per volume due to $LiPF_6$ decomposition is given by[101]

$$j_{H^+}^{salt} = Fk_{decom}(c_{H_2O})^2 c_{LiPF_6}, \tag{4.29}$$

where k_{decom} is the reaction coefficient, $c_{H_2O}$is the water concentration in the electrolyte, and $c_{LiPF_6}$is the $LiPF_6$ concentration in the electrolyte. Due to the high ionization of $LiPF_6$, the concentration c_{LiPF_6} can be approximated by c_{Li^+}.

The effect of the potential on the transport of Mn^{2+} and H^+ is neglected due to the extremely low concentrations of these species. Therefore, the migration term is neglected, and only the diffusion law applies in the mass conservation of H^+ and Mn^{2+}.[38]

The overall reaction and diffusion process is summarized in Figure 4.2. The mass conservation for H^+ is expressed by

$$\varepsilon_2^{pos}\frac{\partial c_{H^+}}{\partial t} = \nabla\cdot\left(D_{H^+}^{eff}\nabla c_{H^+}\right) + \frac{1}{F}\left(j_{H^+}^{oxid} + j_{H^+}^{salt} - 4a_s^{pos}i_{Mn\_react}\right), \quad \text{positive electrode} \tag{4.30}$$

$$\varepsilon_2^{sep}\frac{\partial c_{H^+}}{\partial t} = \nabla\cdot\left(D_{H^+}^{eff}\nabla c_{H^+}\right) + \frac{j_{H^+}^{salt}}{F}, \quad \text{separator} \tag{4.31}$$

$$\varepsilon_2^{neg}\frac{\partial c_{H^+}}{\partial t} = \nabla\cdot\left(D_{H^+}^{eff}\nabla c_{H^+}\right) + \frac{1}{F}\left(j_{H^+}^{salt} + a_s^{neg}i_{H_2}\right), \quad \text{negative electrode} \tag{4.32}$$

$$\text{Boundary conditions: } \left.\frac{\partial c_{H^+}}{\partial x}\right|_{x=0} = \left.\frac{\partial c_{H^+}}{\partial x}\right|_{x=L} = 0, \tag{4.33}$$

where ε_2 is the electrolyte phase volume fraction, $D_{H^+}^{eff}$ is the effective diffusivity of H^+, a_s^{pos} and a_s^{neg} are the active surface area per unit electrode volume on the postive (pos) electrode and negative (neg) electrode, respectively, and L represents the cell thickness including the anode, seperator and cathode.

The mass conservation for Mn^{2+} in the electrolyte is expressed by:

$$\varepsilon_2^{pos}\frac{\partial c_{Mn^{2+}}}{\partial t} = \nabla\cdot\left(D_{Mn^{2+}}^{eff}\nabla c_{Mn^{2+}}\right) + \frac{1}{F}a_s^{pos}i_{Mn\_dis}, \quad \text{positive electrode} \tag{4.34}$$

$$\varepsilon_2^{sep}\frac{\partial c_{Mn^{2+}}}{\partial t} = \nabla\cdot\left(D_{Mn^{2+}}^{eff}\nabla c_{Mn^{2+}}\right), \quad \text{separator} \tag{4.35}$$

$$\varepsilon_2^{neg}\frac{\partial c_{Mn^{2+}}}{\partial t} = \nabla\cdot\left(D_{Mn^{2+}}^{eff}\nabla c_{Mn^{2+}}\right) + \frac{1}{F}a_s^{neg}i_{Mn\_dep}, \quad \text{negative electrode} \tag{4.36}$$

$$\text{Boundary condition: } \left.\frac{\partial c_{Mn^{2+}}}{\partial x}\right|_{x=0} = \left.\frac{\partial c_{Mn^{2+}}}{\partial x}\right|_{x=L} = 0, \tag{4.37}$$

where $c_{Mn^{2+}}$is the concentration of Mn^{2+} and $D_{Mn^{2+}}^{eff}$ is the effective diffusivity.

The mass conservation for H_2O in the electrolyte is expressed by

$$\varepsilon_2^{pos}\frac{\partial c_{H_2O}}{\partial t} = \nabla\cdot\left(D_{H_2O}^{eff}\nabla c_{H_2O}\right) + \frac{1}{F}\left(2a_s^{pos}i_{Mn\_react} - j_{H^+}^{salt}\right), \quad \text{positive electrode} \tag{4.38}$$

$$\varepsilon_2^{sep}\frac{\partial c_{H_2O}}{\partial t} = \nabla\cdot\left(D_{H_2O}^{eff}\nabla c_{H_2O}\right) - \frac{j_{H^+}^{salt}}{F}, \quad \text{separator} \tag{4.39}$$

$$\varepsilon_2^{neg}\frac{\partial c_{H_2O}}{\partial t} = \nabla\cdot\left(D_{H_2O}^{eff}\nabla c_{H_2O}\right) - \frac{j_{H^+}^{salt}}{F}, \quad \text{negative electrode} \tag{4.40}$$

$$\text{Boundary condition: } \left.\frac{\partial c_{H_2O}}{\partial x}\right|_{x=0} = \left.\frac{\partial c_{H_2O}}{\partial x}\right|_{x=L} = 0, \tag{4.41}$$

where $D_{H_2O}^{eff}$ is the effective diffusivity of H_2O.

The Mn dissolution-induced active material loss alone cannot explain the overall capacity loss. Xia *et al*.[39] reported that the measured capacity losses caused by Mn dissolution are only 34% and 23% of the overall capacity loss at 50 ℃ and room teperature, respectively. It is suspected that the other loss of the overall capacity is due to the Mn dissolution-induced contact-resistance increase, particle structure distortion and LMO particle isolation from the conductive nework[106].

In our study, contact-resistance increase and active material loss are modeled based on the volume fraction change of the LMO cathode. Accounting for the acid-induced Mn dissolution, the volume fraction of the solid phase, ε_1, at the cathode is given by[38]

$$\frac{\partial \varepsilon_1^{pos}}{\partial t} = -\frac{a_s^{pos} i_{Mn\_react}\bar{V}}{F}\ , \tag{4.42}$$

where $\bar{V}$is the molar volume of LMO.

The effective conductivity of the solid phase, k_1^{eff}, relates to the volume fraction by

$$k_1^{eff} = k_1(\varepsilon_1)^p, \tag{4.43}$$

wherei $k_1$is the solid phase conductivity, and p is the Bruggeman porosity exponent.

As disccused above, cathode capacity fade stems from Mn dissolution-induced active material loss, contact-resistance increase, particle structure distortion and particle isolation. The active material loss and contact-resistance increase can be reflected in the cell level model by Eq. (4.42) and Eq. (4.43). However, in order to reflect the capacity fade due to particle structure distortion and particle isolation in the cell level model, a term called usable volume fraction,

$\varepsilon_{usable}^{pos}$, is introduced here. The solid phase volume fraction, ε_1^{pos}, accounts for all the active and inactive (isolated and distorted due to stress induced by intercalation/deintercalation) particles in the solid phase, while the usable volume fraction, $\varepsilon_{usable}^{pos}$, accounts for only the connected active particles in the solid phase and therefore can reflect the capacity fade due to particle isolation and structure distortion. Normally, $\varepsilon_{usable}^{pos}$, is smaller than ε_1^{pos} except at the initial state where they have the same value.

The change of the usable volume fraction is hypothesised to be propotional to the change of the solid phase volume fraction, namely

$$\varepsilon_{usable0}^{pos} = \varepsilon_{1,ini}^{pos} \text{ at } t=0, \tag{4.44}$$

$$\frac{d\varepsilon_{usable}^{pos}}{dt} = k_{iso}\frac{d\varepsilon_1^{pos}}{dt}, \tag{4.45}$$

where k_{iso} is a coefficient.

As a LMO particle becomes isolated from the conductive network or distorted due to Mn dissolution, the effective capacity per unit electrode volume decreases. The maximum concentration of Li per unit electrode volume also decreases,

$$c_{el,\max}^{pos} = \varepsilon_{usable}^{pos} c_{1,max}^{pos}, \tag{4.46}$$

$$c_{el}^{pos} = \varepsilon_1^{pos} c_1^{pos}, \tag{4.47}$$

where $c_{el,\max}^{pos}$ is the maximum amount of lithium per unit electrode volume, $c_{1,max}^{pos}$ is the maximum lithium concenctration in the solid phase, c_{el}^{pos} is the amount of lithium per unit electrode volume, and c_1^{pos} is the lithium concenctration in the solid phase. Therefore, the state of charge (SOC) of the electrode can be calculated by

$$SOC^{pos} = c_{el}^{pos}/c_{el,\max}^{pos}. \tag{4.48}$$

The lithium concentration in the electrode decreases as Mn dissolution induced particle distortion and isolation increases.

4.2.3 Part III: Side reaction coupled cell level electrochemical model

In order to investigate the impact of the side reactions on the cell performance, the degradation mechanisms introduced in previous sections will be integrated into cell level model. As shown in Figure 4.1, a typical lithium ion cell consists of two porous composite electrodes, an ionic conductive separator and copper and aluminum current collectors. Newman's porous composite electrode model[27] is used here as the basic cell level framework. The cell level model consists of three domains: the negative composite electrode, the separator, and the positive composite electrode. The composite electrodes consist of active material (Li_xC_6 for the anode, $Li_yMn_2O_4$ for the cathode), electrolyte solution ($LiPF_6$ 1M EC/DMC) and a small amount of conductive additive (carbon black) and binder (PVDF). The mass and charge are conserved in the cell. The total lithium intercalation and deintercalation current per volume, j_{loc} , is taken into account by the Butler-Volmer equation,

$$j_{loc} = a_s i_0 \left\{ \exp\left[\frac{\alpha_a F}{RT}\left(\eta - \frac{R_{SEI}}{a_s} j_{loc}\right)\right] - \exp\left[-\frac{\alpha_c F}{RT}\left(\eta - \frac{R_{SEI}}{a_s} j_{loc}\right)\right]\right\} \tag{4.49}$$

$$\eta = \phi_1 - \phi_2 - U \tag{4.50}$$

$$R_{SEI} = k_{res}\delta \tag{4.51}$$

where j_{loc} is the local reaction current, a_s is the active surface area per unit electrode volume, i_0 is the exchange current density, α_a is the anodic charge transfer coefficent, α_c is the cathodic charge transfer coeffcient, R_{SEI} is the resistance of the SEI layer, U is the open-circuit potential, and k_{res} is the SEI resistivity.

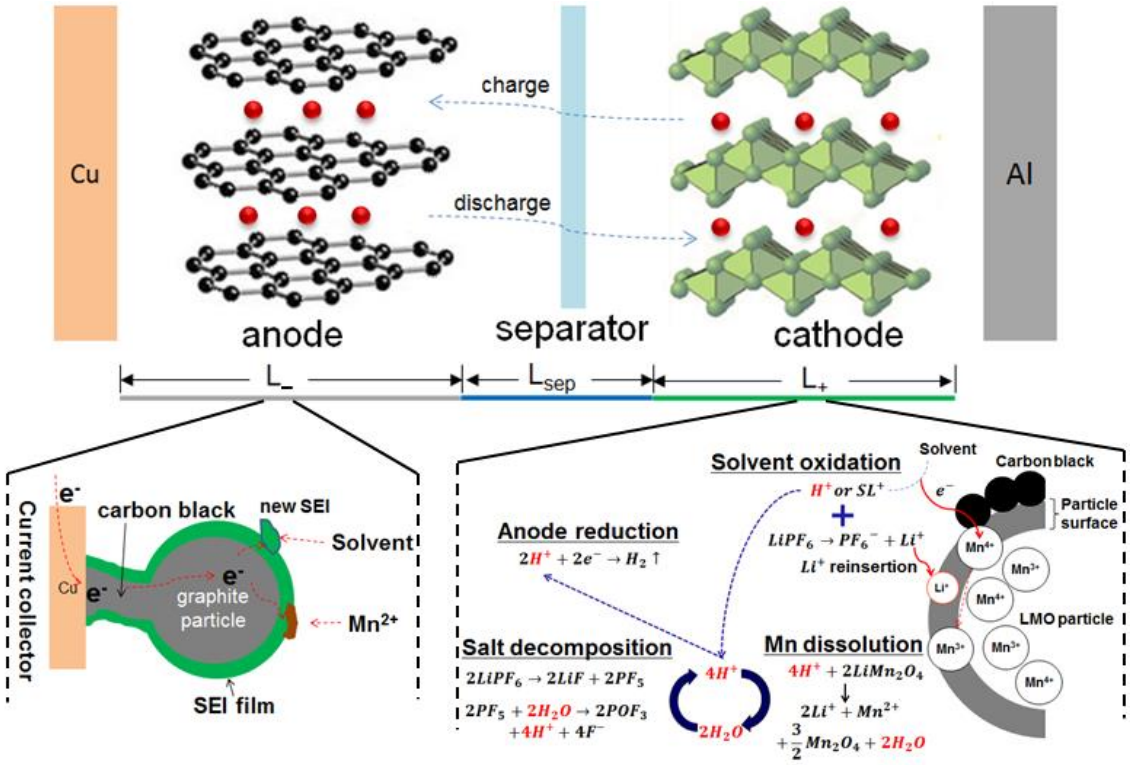

Figure 4.3 A schematic diagram of side reactions coupled with the cell level framework. The left bottom corner illustrates the side reactions on anode, including SEI formation and Mn deposition. The right bottom corner illustrates side reactions on cathode, including salt decomposition, solvent oxidation, and Mn dissolution.

In order to couple the side-reaction particle-level model to Newman's cell level model, the side-reaction induced cyclable lithium loss should be added or subtracted from the lithium intercalation or deintercalation. On the anode, the side reactions are coupled to the cell level model through the following equations:

$$j_{Li} = j_{loc} - j_{side} \tag{4.52}$$

$$j_{side} = a_s^{neg}(i_{SEI} + i_{H_2} + i_{Li\_dep} + i_{Mn\_dep}) \tag{4.53}$$

where j_{Li} is the current density of lithium intercalation or deintercalation, i_{SEI} is the lithium loss due to SEI growth, i_{H_2} is the lithum loss from the hydrogen gas, and i_{Mn_dep} represents the lithium loss by Mn deposition.

On the cathode, the side reactions are coupled to the cell level model by

$$j_{Li} = j_{loc} + 2a_s^{pos} i_{Mn\_react} - j_{oxid} \tag{4.54}$$

where i_{Mn_react} is lithum loss due to acid attack and j_{oxid} is lithium reinsertion due to electrolyte oxidation.

Table 4.1 summarized the equations used in the degradation model. The side reaction equations are divided into the anode side and cathode side.

Table 4.1 An overview of equations employed in the degradation model

Cell level modeling		Boundary conditions
	Charge	
Electrolyte phase	$\frac{\partial}{\partial x}\left(k_2^{eff}\frac{\partial \phi_2}{\partial x}\right)-\frac{\partial}{\partial x}\left(k_{2D}^{eff}\frac{\partial}{\partial x}\ln c_2\right)+j_{loc}=0$	$\left.\frac{\partial \phi_2}{\partial x}\right\|_{x=0}=\left.\frac{\partial \phi_2}{\partial x}\right\|_{x=L}=0$
Solid phase	$\frac{\partial}{\partial x}\left(k_1^{eff}\frac{\partial \phi_1}{\partial x}\right)-j_{loc}=0$	$-k_1^{eff}\left.\frac{\partial \phi_1}{\partial x}\right\|_{x=0}=k_1^{eff}\left.\frac{\partial \phi_1}{\partial x}\right\|_{x=L}=\frac{I}{A}, \left.\frac{\partial \phi_1}{\partial x}\right\|_{x=L_-}=\left.\frac{\partial \phi_1}{\partial x}\right\|_{x=L_-+L_{sep}}=0$
	Species	
Electrolyte phase		
$\frac{\partial(\varepsilon_2 c_2)}{\partial t}=\frac{\partial}{\partial x}\left(D_2^{eff}\frac{\partial c_2}{\partial x}\right)+\frac{1-t_+^0}{F}j_{loc}$ (Anode and Separator)		$\left.\frac{\partial c_2}{\partial x}\right\|_{x=0}=\left.\frac{\partial c_2}{\partial x}\right\|_{x=L}=0$
$\frac{\partial(\varepsilon_2 c_2)}{\partial t}=\frac{\partial}{\partial x}\left(D_2^{eff}\frac{\partial c_2}{\partial x}\right)+\frac{1-t_+^0}{F}j_{loc}+\frac{(2a_s^{pos}i_{Mn\_react}-j_{oxid})}{F}$ (Cathode)		
Solid phase	$\frac{\partial(c_1)}{\partial t}=\frac{D_1}{r^2}\frac{\partial}{\partial r}\left(r^2\frac{\partial c_1}{\partial r}\right)$	$\left.\frac{\partial c_1}{\partial r}\right\|_{r=0}=0, D_1\left.\frac{\partial c_1}{\partial r}\right\|_{r=R_s}=-\frac{j_{Li}}{a_s F}$

Side reaction modeling	Equations
Anode SEI growth	$i_{SEI}=R(\delta)\cdot i_{SEI}^{*}=-e^{-\lambda_{SEI}\delta}Fk_{SEI}c_{EC}\exp[-\frac{\alpha_c^{SEI}F}{RT}(\phi_1-\phi_2)]$
Anode Manganese deposition	$i_{Mn\_dep}=R(\delta)\cdot i_{Mn\_dep}^{*}$ $=-e^{-\lambda_{Mn\_dep}\delta}Fk_{Mn\_dep}c_{Mn^{2+}}\exp\left[-\frac{\alpha_c^{Mn\_dep}2F}{RT}(\phi_1-\phi_2)\right]$
Anode hydrogen gas	$i_{H_2}=R(\delta)\cdot i_{H_2}^{*}=-e^{-\lambda_{H_2}\delta}F\,k_{H_2}c_{H^+}\exp\left[-\frac{\alpha_c^{H_2}F}{RT}(\phi_1-\phi_2)\right]$
Cathode Mn dissolution	$i_{Mn\_react}=Fk_{dis}c_{H^+}$
Cathode electrolyte oxidation	$j_{oxid}=a_c i_0^{sol}\exp\left(\frac{\alpha_a^{sol}F}{RT}\eta_{oxid}\right)$
Cathode salt decomposition	$j_{H^+}^{salt}=Fk_{decom}(c_{H_2O})^2 c_{LiPF_6}$

Table 4.2 summarized the battery model parameters. The meanings of the parameters in Newman models can be found in the reference[27].

Table 4.2 Cell level model parameters

Parameter	Negative electrode	Separator	Positive electrode
Electrode thickness (m)	150×10^{-6}	30×10^{-6}	110×10^{-6}
Particle radius R_s (m)	12.5×10^{-6}		8.5×10^{-6}
Active material volume fraction ε_1	0.471		0.297
Polymer and conductive filler volume fraction ε_3	0.172		0.259
Porosity (electrolyte phase volume fraction) ε_2	0.357	1	0.444
Solid phase conductivity k_1 (S/m)	100		3.8
Effective conductivity of solid phase k_1^{eff}(S/m)	$k_1^{eff} = k_1(\varepsilon_1)^p$		$k_1^{eff} = k_1(\varepsilon_1)^p$
Maximum solid phase concentration $c_{1,max}$ (mol/m^3)	26390		22860
Solid phase Li diffusion coefficient D_1 (m^2/s)	3.9×10^{-14}		1×10^{-13}
Initial electrolyte concentration (mol/m^3)	1000	1000	1000
Li transference number t_+^0	0.363	0.363	0.363
Electrolyte phase ionic conductivity k_2 (S/m)[c]	$k_2(c_2)$ curve		
Effective electrolyte phase ionic conductivity k_2^{eff}(S/m)	$k_2^{eff} = k_2(\varepsilon_2)^p$		
Electrolyte phase Li diffusion coefficient D_2 (m^2/s)	7.5×10^{-11}	7.5×10^{-11}	7.5×10^{-11}
Effective electrolyte phase Li diffusion coefficient D_2^{eff}(S/m)	$D_2^{eff} = D_2(\varepsilon_2)^p$		
Effective electrolyte phase Li diffusion conductivity k_{2D}^{eff}(A/m)	$k_{2D}^{eff} = \frac{2RTk_2^{eff}}{F}(1 - t_+^0)(1 + \frac{d \ln f_-^+}{d \ln c_2})$		
Electrolyte activity coefficient f_-^+	1	1	1
Bruggeman porosity exponent p	1.5	1.5	1.5

Charge transfers coefficient α_a, α_c	0.5	0.5
Reaction rate coefficient k_0 (m/s)	2×10^{-11}	2×10^{-11}
Exchange current density i_0 (A/m^2)	$Fk_0{c_2}^{\alpha_a}(c_{1,max} - c_{1,s})^{\alpha_a}{c_{1,s}}^{\alpha_c}$	
Active surface area per unit electrode volume a_s (1/m)	$\frac{3\varepsilon_1}{R_s}$	$\frac{3\varepsilon_{usable}^{pos}}{R_s}$
Faraday constant F (C/mol)	96485.3415	
Initial electrode SOC (fresh cell)	0.01	0.99
Negative electrode equilibrium potential U_(V) [c]	U_$(c_{1,s}/c_{1,max})$ curve	
Positive electrode equilibrium potential U$_+$(V) [c]		U$_+(c_{1,s}/c_{1,max})$) curve

[c] Curves in Appendix

Table 4.3 lists the key parameters for the side reactions. More details on the parameters can be found in the reference[38, 82].

Table 4.3 Parameter of side reactions

Parameter	Value	Parameter	Value
k_{SEI}	6×10^{-10} m/s	α_a^{sol}	0.5
c_{EC}	4541 mol/m^3	U_{oxid}^{eq} [a]	4.1 V
λ_{SEI} [a]	1.2×10^7 1/m	f_{H^+} [a]	15%
α_c^{SEI}	0.5	X_c [a]	10%
M_{SEI}	0.162 kg/mol	X_c^{ref} [a]	10%
ρ_{SEI}	1690 kg/m^3	$a_c^{ref} i_0^{sol}$ [a]	10 A/m^3
k_{Mn_dep} [a]	80×10^{-9} m/s	k_{decom} [a]	7.13×10^{-10} m^6/mol^{2}s
$\alpha_c^{Mn\_dep}$	0.5	$D_{H^+}^{eff}$ [a]	$10 \times 10^{-11} \varepsilon_2{}^p$ m^2/s
λ_{Mn_dep} [a]	3×10^6 1/m	$D_{Mn^{2+}}^{eff}$ [a]	$5 \times 10^{-11} \varepsilon_2{}^p$ m^2/s
k_{H_2} [a]	2.07×10^{-8} m/s	$D_{H_2O}^{eff}$ [a]	$3 \times 10^{-11}\ \varepsilon_2{}^p$ m^2/s
λ_{H_2} [a]	2×10^5 1/m	$\bar{V}$	1.4×10^{-4} m^3/mol
$\alpha_c^{H_2}$	0.5	k_{iso} [a]	8
k_{dis} [a]	2×10^{-9}m/s	k_{res} [a]	3×10^4 Ω m
f_{Mn_dis} [a]	40%		

[a]Assumed values

The calibration and validation of the above parameters are introduced in 5.3.5.

4.2.5 Numerical implementation

The mathematical model described in previous sections is a multi-scale model. In this dissertation, a 1D geometry is used to model the cell level dynamics, and a 2D geometry is used to model the particle level dynamics. The 1D geometry consists of three sequentially connected lines to represent the positive electrode, the separator and the negative electrode, respectively. And the 2D geometry which consists of two rectangles to denote the solid phase in the electrodes[107]. Figure 4.4 shows the configuration of the combined 1D cell level and pseudo 2D particle level model.

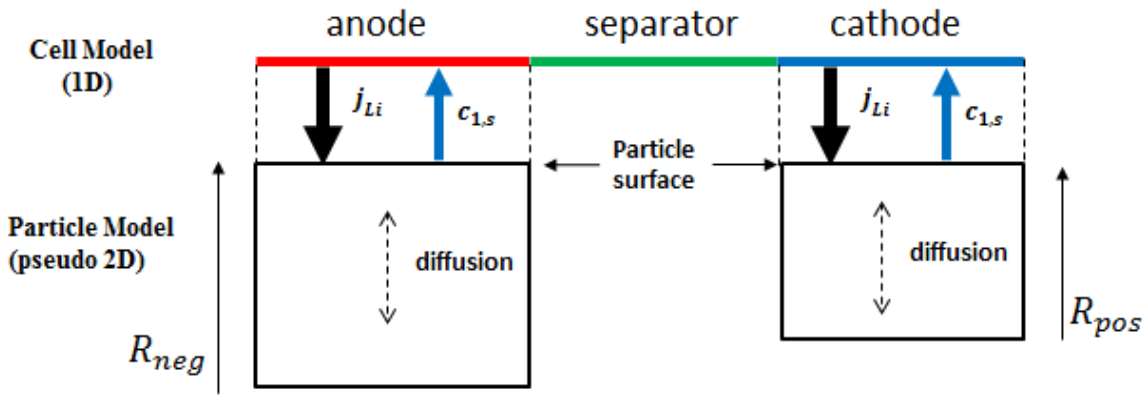

Figure 4.4 Pseudo 2D model for side reaction coupled degradation model, the top 1D geometry consists of three segments which denote the anode electrode, the separator and the cathode electrode. The bottom two rectangles represent the solid phases of the anode and cathode. The Li intercalation/deintercalation flux is extracted from the 1D cell model and projected on the top boundary of the 2D geometry. The Li concentration on the top boundary of the 2D geometry is projected on the 1D domain as the particle surface concentration of Li [107].

Cell level variables are solved in the 1D geometry, such as, the Li-ion concentration of the binary electrolyte, the potential distribution in the electrolyte, the potential distribution in the solid phase and the pore wall flux (flux between electrolyte and solid phase). The electric potential on the left end of the anode electrode is set to 0V as the electric ground. At the right

end of the cathode electrode, the current density is specified. The pore wall flux calculated from 1D domain is projected on the top boundary of the 2D geometry by using linear extrusion in COMSOL Multiphysics. After receiving the flux from 1D domain, Li concentration in the solid phase is calculated in the 2D domain, and the particle surface concentration which is on the top boundary of the 2D geometry is projected back to the 1D domain for equilibrium potential calculation in 1D domain. The coupling between 2 domains is done by linear extrusion in COMSOL Multiphysics.

The vertical coordinate in the 2D geometry represents the radial direction of the electrode particles. The lithium diffusion is along the radial direction of the particle; therefore, the diffusion in the 2D geometry happens only in Y direction (up-down direction). The diffusion of the Lithium in the X direction (left-right direction) is ignored by setting the corresponding diffusion coefficient to zero.

4.3 Summary

This chapter utilizes first-principle physics to develop degradation model for lithium ion batteries. In the discourse on degradation model development, different side reactions on both anode and cathode electrode are introduced. The mathematical expressions to describe each side reactions are derived. Later, the combination of these individual side reactions and the coupling between degradation mechanisms and cell level model are elaborated. Newman's battery model is used as a backbone model. Side reactions are added to this backbone model by using a 1D and 2D combined model. This model will be utilized in the subsequent chapters to investigate the battery degradation patterns over long term cycling, and also to conduct optimal design of battery lifetime.

Chapter 5
Degradation Pattern Analysis and Experimental Comparison

5.1 Introduction

In previous chapter, a degradation model is developed by taking into account the major degradation mechanisms on both anode and cathode. This model enables us to investigate the long term degradation patterns for Li-ion battery. This degradation pattern analysis is a critical step toward battery performance improvement. Several studies have considered the battery degradation analysis [108-113] by focusing on specific mechanisms, not by regarding all the key mechanisms together. Because batteries' lifetimes are affected by the combined effect of different degradation mechanisms[114], it is important to consider their interactions and their impact on the overall battery performance simultaneously. In this chapter, the dynamic process of cell degradation and the effects of each different degradation mechanism on battery capacity fade during cycling are investigated using the developed model. After the degradation pattern analysis, three electrode coin cells are fabricated and cycled over a long period of time in order to investigate how the overall capacity fade is affected by the individual electrode capacity and the cyclable lithium. SEM and TEM measurements are employed to provide further physical evidence of degradation mechanisms at cathode and anode before and after long term cycling. A water-glass model was then proposed to describe the whole degradation process based on the result from both model prediction and long term cycling data.

The following sections show the details of capacity fade during cycling and the analysis of capacity fade based on the degradation mechanisms described in previous Chapter, and also the details of the experimental results.

5.2 Degradation Pattern Analysis

5.2.1 Capacity fade during cycling

In order to investigate the overall degradation pattern, the simulation study is conducted to cycle the Li-ion cell over 900 cycles. The cycling condition is simulated based on constant current/constant voltage (CCCV): the cell is charged with 1C rate until the cutoff voltage of 4.1 V. Next, the voltage is held until the current drops down to 0.1C. Next, the cell is discharged to 3.4 V at 1C, held at 3.4 V until the current drops down to 0.1C.

In order to trace cyclable lithium loss through the whole cell life from factory assemblage to cell failure, the simulation starts from the fresh cell condition, in which the cell is composed of an empty graphite anode and a fully liathiated LMO cathode. The initial SOCs of the negative electrode and the positive electrode are set to 0.01 and 0.99, respectively, in order to represent the fresh state of the cell.

Figure 5.1 shows the discharge capacity fade during cycling from our model prediction. The capacity degradation of the cell can be divided into three stages: acceleration, stabilization and saturation. Spotnitz studied the cycle life data from many manufacturers[78]. These data showed that the rate of capacity fade was initially high, but slowed down quickly. After several hundreds of cycles the rate of capacity fade started a rapid increase. This degradation pattern is consistent with the degradation stages reported by our model.

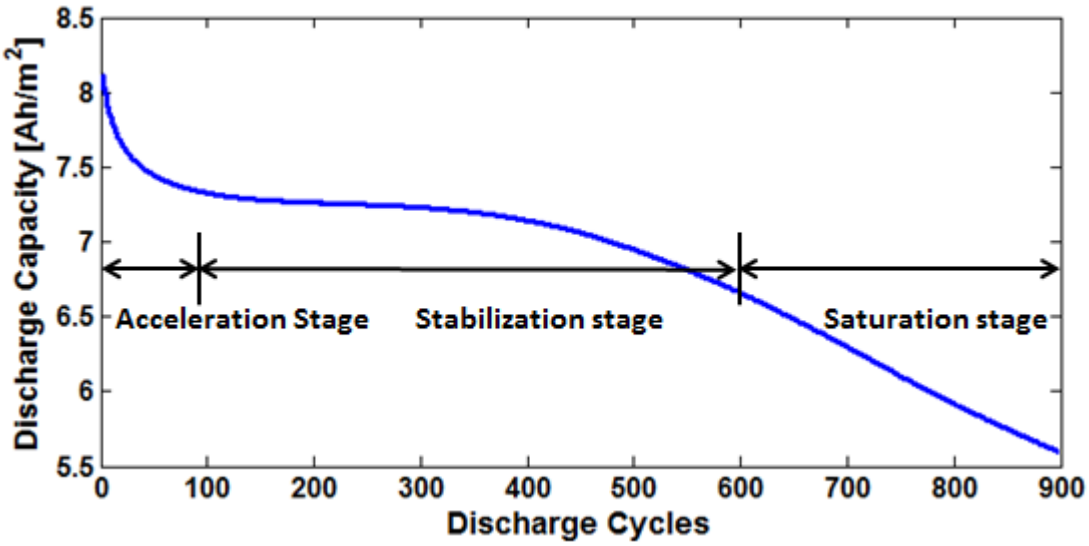

Figure 5.1 Degradation of discharge capacity after 900 cycles. The degradation is divided to three stages: acceleration stage, stabilization stage and saturation stage.

In the acceleration stage, capacity fade is quite fast due to SEI formation on the anode surface. SEI formation can remove a significant amount of cyclable lithium. For the graphitic materials such as MCMB, the irreversible capacity ranges between 8% and 15%.[12] In our simulation, the capacity fade in the acceleration stage is about 10%, which is close to the experimental values[12]. As the SEI grows thicker, the reaction rate slows down due to the isolation effect of SEI layer. The cyclable lithium loss also slows down, and the battery enters the stabilization stage. In this stage, battery performance is relatively stable, and capacity decreases slowly. Instead of cyclable lithium loss, the capacity loss of the cathode due to Mn dissolution becomes a main contributor to capacity fade. As Mn dissolution develops further, the cathode capacity is insufficient to contain all the cyclable lithium in the system and the cathode is almost fully intercalated at the end of discharge. At this point, the cell enters the saturation stage. Due to the steepness of the cathode voltage curve at high depth of discharge (DOD), the battery discharge process reaches the cutoff voltage earlier.

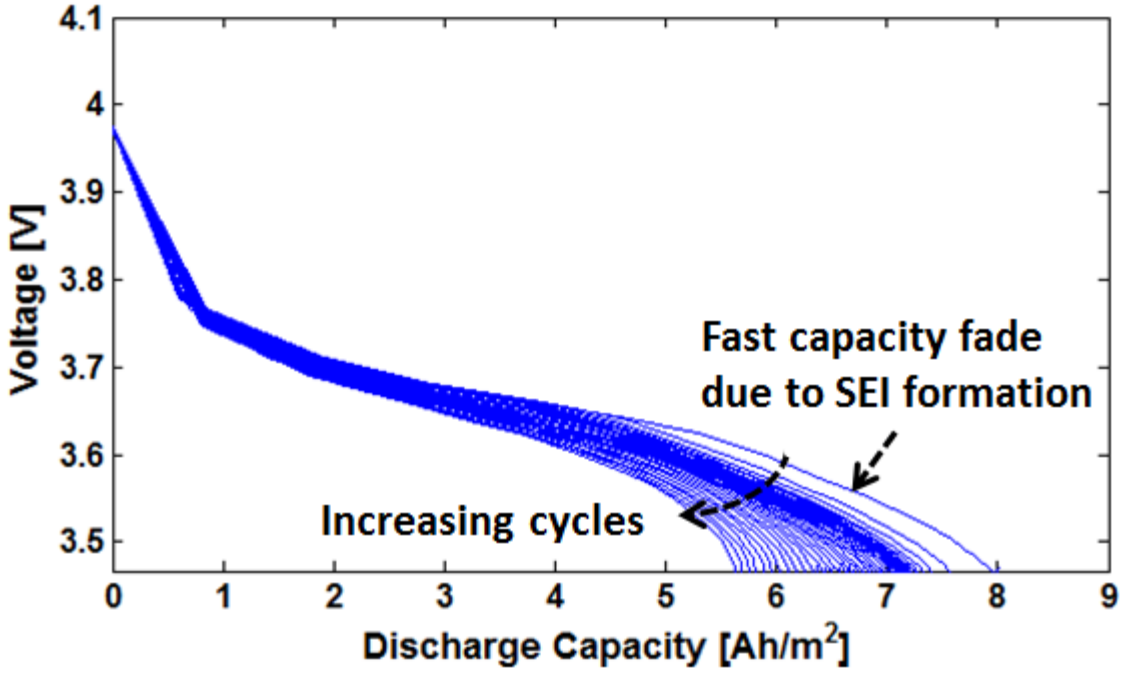

Figure 5.2 Discharge curves of aged graphite/LMO cell every 20 cycles during 900 cycles. The fast capacity fade is observed at the initial cycles due to the SEI formation induced cyclable lithium loss.

The capacity fade is also reflected in the discharge curves of aged graphite/LMO cell during 900 cycles as shown in Figure 5.2. In the initial cycles where SEI formation-induced cyclable lithium loss is the dominant contributor to the cell capacity fade, a quick shift of the potential curve near the end of discharges is observed; this is due to fast cyclable lithium loss induced by SEI formation in the acceleration stage. As the cycling number increases, the capacity decreases, and the cell voltage reaches the cutoff voltage earlier. The SEI formation induced potential shift was also confirmed in experiments. Amatucci *et al* [115] studied the degradation of $LiMn_2O_4$/coke cell and a quick shift of potential was observed. They reported that a surface electrolyte interface layer was formed on the coke surface. This passive layer reduced the cyclable lithium and led to the observed capacity fade and potential shift.

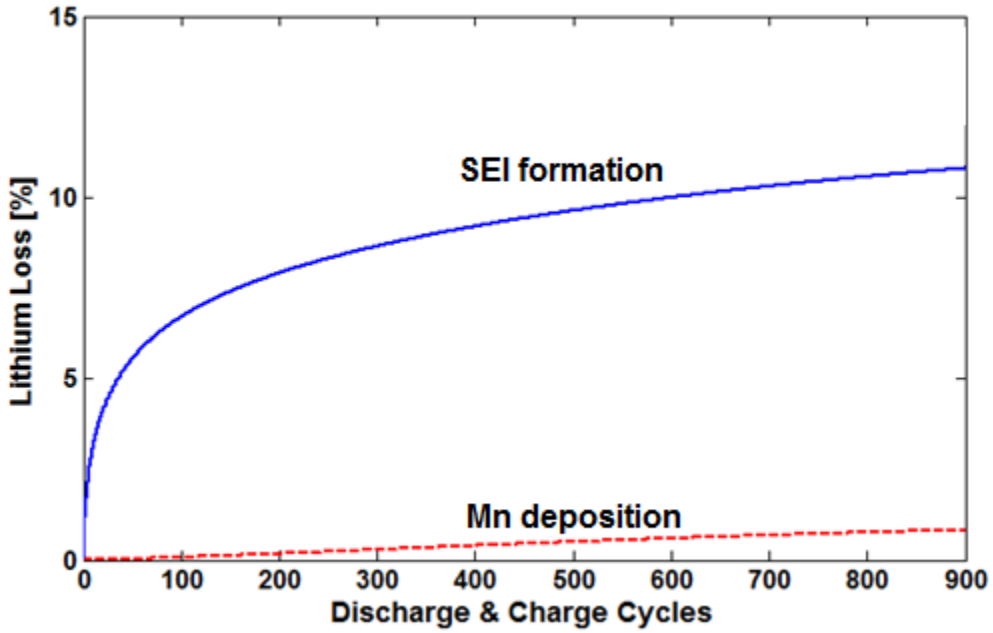

Figure 5.3 Side reaction induced cyclable lithium loss. SEI formation is the major contributor to cyclable lithium loss, and the loss is fast during initial cycles.

Figure 5.3 and Figure 5.4 show cyclable lithium loss and active material loss due to the side reactions, which provide us more insight as to what happens inside the cell.

The main side reactions consuming the cyclable lithium are SEI formation and Mn deposition. Many studies have identified a relationship of SEI growth thickness $\propto t^{1/2}$ and demonstrated that the SEI parabolic growth law fit the experimental data very well[116]. As shown in Figure 5.3, the SEI formation curve from our simulation is also consistent with the parabolic growth law. SEI formation contributes to the most significant part of cyclable lithium loss. The Mn deposition-induced cyclable lithium loss is negligible compared to the SEI formation. Therefore, SEI formation dominates cyclable lithium loss during cycling. Figure 4 shows that in initial cycles the SEI layer consumes 7% of the cyclable lithium when the paricles have a radius of 12.5 μm. Smith *et al* studied the SEI growth by high precision coulometry[116]. They reported about 8% lithium loss after 25 days which is about 250 cycles in our simulation.

The lithium loss from our simulation is about 7% after 250 cycles and is very close to their experiment data. Mn deposition causes additional cyclable lithium loss. The speed of the Mn deposition is stable through the whole cycling life due to the high penetration of Mn^{2+} through the SEI layer and the continuous dissolution of Mn^{2+} from the cathode.

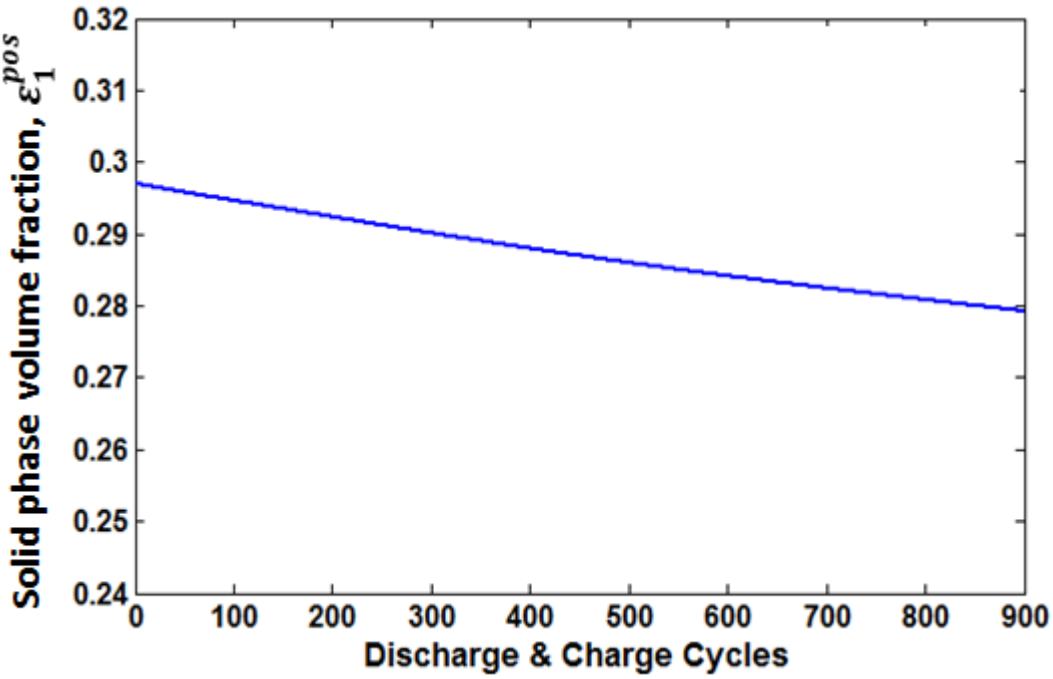

Figure 5.4 Cathode active material volume fraction change over 900 cycles. The Mn dissolution leads to the cathode active material loss and therefore the volume fraction decreases.

Cyclable lithium loss contributes the most capacity loss in the acceleration stage; the active material loss becomes important when the cell enters the stabilization and saturation stages. Figure 5.4 presents the change of active material volume fraction during cycling. After 900 cycles the solid phase volume fraction decreases to 0.279, which is about 94% of the initial value. The decrease of the solid phase volume fraction contributes to capacity fade in three ways. First, the Mn dissolution-induced active material loss leads to a decrease of conductivity of the solid phase. Second, the active material loss itself and the induced structure distortion contribute to

capacity fade. Third, the active material loss leads to contact loss of the active particle with the conductive network, which causes the isolation of active particles. All together, the decrease of the solid volume fraction will reduce the effective capacity of the cathode electrode.

5.2.2 Capacity fade analysis

As discussed in the previous section, there are three stages of lithium ion battery capacity fade. In order to clearly explore the effects of different degradation mechanisms on the capacity fade and battery performance at each stage, evolutions of the SOC swing windows of each individual electrode are investigated. Particle isolation and loss of active materials are considered in our model. Here we wish to emphasize that the SOC of an electrode as defined earlier accounts for particles still in good contact with the conducting network, and is not an average of all the connected and non-connected particles.

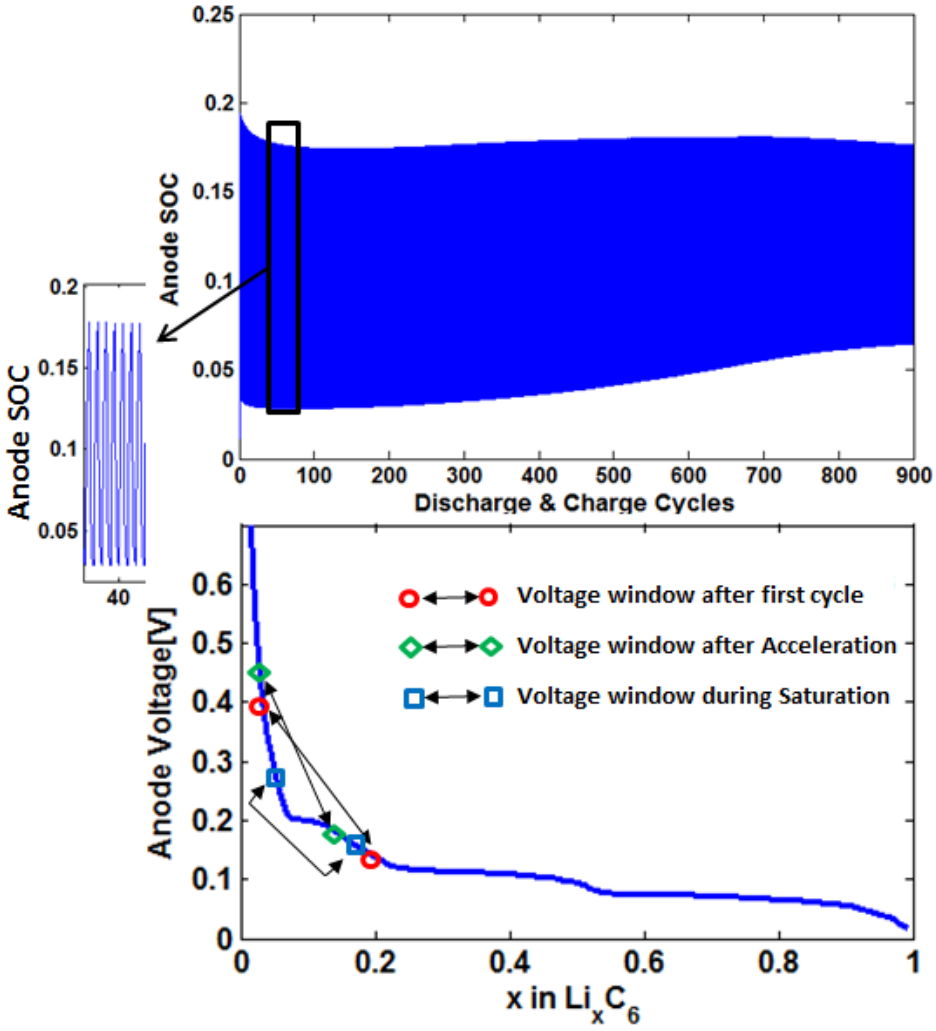

Figure 5.5 SOC swing window on anode. Each pair of makers indicate the SOCs at the end of discharge/charge that are representative of different stages. The lower markers correspond to charged state, the higher markers correspond to discharged state.

Acceleration stage

Figure 5.5 shows the evolution of the SOC swing window on the anode during 900 cycles. In the initial cycles, the anode SOC swing window starts to move down due to the sudden lithium loss. The SEI layer growth during the initial cycles consumes significant amounts of cyclable lithium in the anode, which drags the SOC swing window down in the anode. Due to the mass conservation in the system, the cyclable lithium in the cathode also decreases in the initial cycles as shown in Figure 5.6.

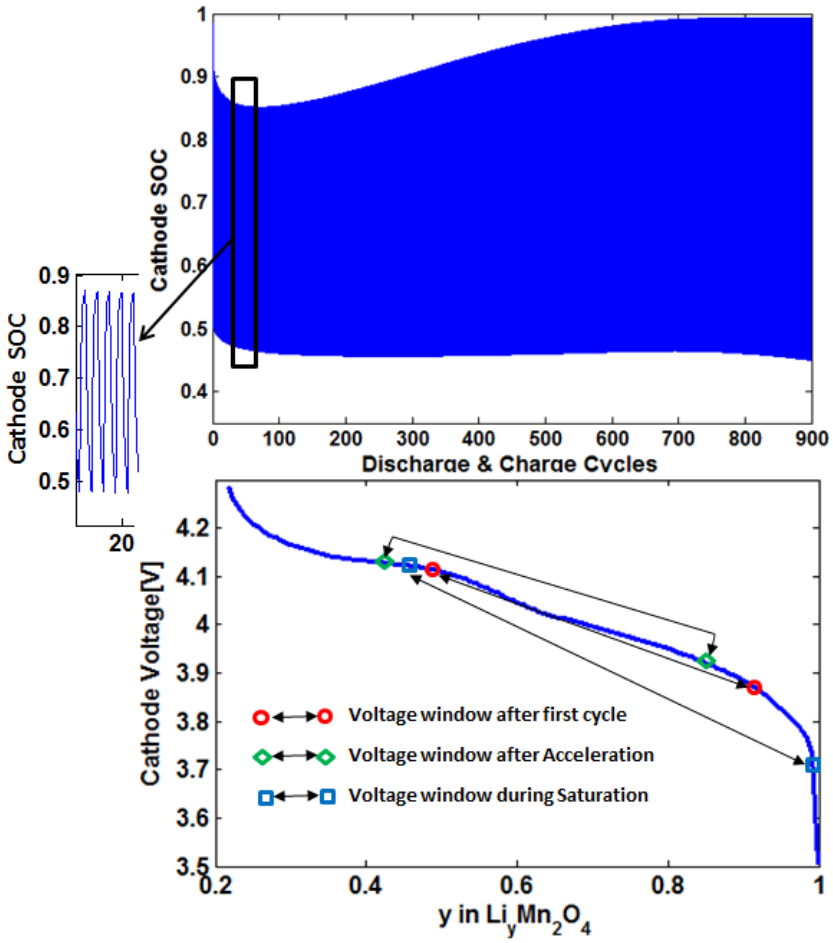

Figure 5.6 SOC swing window on cathode. Each pair of makers indicate the SOCs at the end of discharge/charge that are representative of different stages. The lower markers correspond to discharged state, the higher markers correspond to charged state.

The SOC swing window shift on both the anode and cathode affects the voltage response of each electrode. As shown in the bottom of Figure 5.5, the lower SOC in the anode increases anode potential, which leads to earlier termination of discharge. The lower SOC swing window also increases cathode potential leading to earlier termination of charge. The shift of the swing windows towards the steep potential side accelerates capacity fade. As a result of cyclable lithium loss in the anode, both electrodes are pushed to the high steep voltage region. Further, the high voltage on the cathode also speeds up electrolyte oxidation, thereby accelerating Mn

dissolution. In the acceleration stage, the side reaction induced cyclable lithium loss dominates capacity fade.

Stabilization stage

As the SEI layer grows thicker, the SEI formation on the anode surface slows down, and the battery enters the stabilization stage. In this stage the battery performance is relatively stable, and the capacity slowly decreases.

As shown in Figure 5.5 and Figure 5.6, the SOC swing windows on both electrodes shift up after entering the stabilization stage. At the same time, the cyclable lithium loss continues at a relatively slow rate compared to the acceleration stage. In the stabilization stage, the capacity loss of cathode electrode outpaces the loss of cyclable lithium; therefore, SOC on both electrodes are raised up. The shift up of SOC swing windows also brings the electrode voltage back to a relatively flat voltage region. In this stage, because of the low lithium loss rate and low cathode capacity loss, the battery works in a relatively balanced way, which benefits cell capacity performance.

Saturation stage

After the acceleration and stabilization stages, cathode stress induced fracture and Mn dissolution continue. Mn dissolution induced active material loss, fracture induced particle structure distortion and particle isolation develop further. The final result is poor capacity of the cathode. After hundreds of cycles, the capacity of the cathode is insufficient to accommodate all cyclable lithium. Therefore, more and more lithium ions are left in the anode. As shown in Figure 5.5, lithium in the anode increases. Due to the small capacity of the cathode, the cathode is almost fully intercalated, even with a small amount of lithium. The poor capacity on the cathode makes the cathode quickly saturated during discharge, and also quickly depleted during

charge. As shown in Figure 5.6, the SOC swing window on the cathode side becomes wider in the saturation stage due to the small capacity. The anode potential is pushed to a low level due to the increased concentration, and the SOC swing window of anode shrinks due to the small amount of Li interaction and deintercalation.

The three stages of degradation have been observed in experiments. Zhang *et al*. studied the capacity degradation pattern of lithium ion batteries based on a series of long term cycling data [13]. A parameter estimation technique was used to investigate the parameter trajectories along cycling. Their results showed a clear three stage capacity degradation pattern, which support our model prediction of acceleration, stabilization and saturation stages.

The effects of different degradation mechanisms on capacity fade and battery performance are studied quantitatively. Our study shows that there are three stages during the battery degradation: the acceleration stage, the stabilization stage and the saturation stage. In the acceleration stage, the cyclable lithium loss due to the SEI formation is dominant. When the SEI layer grows thicker and the side reaction rate decays, the degradation enters the stabilization stage. In this stage, the loss of cathode capacity due two Mn dissolution, and fracture outpaces the cyclable lithium loss, and the concentration of both electrodes starts to increase. In the stabilization stage, the lithium ion battery has relatively stable performance. As Mn dissolution and particle fracture continues further, the cathode loses enough capacity to contain all cyclable lithium ions. More and more cyclable lithium is left in the anode, and the total amount of cyclable lithium ions in the system decreases at very low rate. The poor capacity of the cathode makes the cathode quickly saturated during discharge and also quickly depleted during charge, which accelerates capacity fade.

In our study Mn reduction and precipitation at the anode is deemed to affect the cell by reducing the amount of cyclable lithium, much in the same way that SEI film formation at the anode operates. We have assumed that the SEI structure is independent from Mn deposition. However, it is likely that the Mn deposition may fundamentally change the nature of SEI, such as porosity, ionic conductivity and stability. These coupling effects need more studies and will be considered in future modeling effort.

5.3 Experimental Study of Capacity Fade

5.3.1 Introduction and motivation

Experiments are designed to investigate the capacity fade over long term cycling and provide physical evidence for simulation efforts. A lot of efforts have been spent on understanding the lithium ion battery degradation. Ramadass *et al*.[81] carried out a complete capacity fade analysis for the Sony 18650 cells after hundreds of cycles. They divided the capacity fade into rate capability loss as well as primary and secondary active material losses. Ning *et al*.[72] studied the capacity fade of Sony US 18650 Li-ion battery under different discharge rates and proposed a mechanism to explain the capacity fade that capacity fade is mainly due to SEI growth. Arora *et al*. [12] review a lot of degradation mechanisms and revealed each degradation mechanism. The above research attributes the cell degradation either to a specific degradation mechanism, such as SEI growth, or to a list of mechanisms. However, they didn't explain the roles of the degradation of each individual electrode in the overall capacity fade. And another important issue is the cell voltage data they used is the terminal voltage which is the potential difference between cathode and anode. Because the terminal voltage is the

difference between cathode and anode, not the absolute value of the two electrode open circuit voltages, the potential of each individual electrode is hardly observable[117]. And therefore, the information about each individual electrode capacity fade is not measurable.

In order to investigate how the overall capacity fade is affected by the individual electrode capacity and the cyclable lithium, in this dissertation, three electrode coin cells are fabricated and cycled over a long period of time. The data from the cycled cell provides not only the cell voltage information, but also the voltage information for both anode and cathode, which gives us a deep insight about the degradation of each electrode. The cycled cell is dissembled, and SEM and TEM measurements are employed to provide further physical evidence of degradation mechanisms at cathode and anode before and after long term cycling.

5.3.2 Three electrode cell cycling

Cell fabrication & experiment setup

Graphite and carbon black are provided from TIMCAL. Polyvinylidene difluoride (PVDF) and N-methyl-2-pyrrolidinone are supplied by Kureha. Powders of $LiMn_2O_4$ are available from Sigma Aldrich. The 1:1 solvent mixtures of ethylene carbonate (EC) to dimethylcarbonate (DMC) with 1 M LiPF6 dissolved are made in glove box and contained less than 10 ppm of H_2O.

The anode electrodes are prepared by mixing TIMCAL graphite, 5wt% TIMCAL super p conductive carbon black, 5 wt % PVDF and a small amount of N-methyl-2-pyrrolidinone. The mixture paste is spread on Cu foils and evaporated to dryness under vacuum for 10 h at 100 degree Celsius. The cathode electrodes are prepared by mixing the active component ($LiMn_2O_4$) with 5 wt% TIMCAL super p conductive carbon black, 5 wt% PVDF and a small amount of N-

methyl-2-pyrrolidinone. The mixture is then spread on the Al foils. The cathode and anode composition is listed in Table 5.1.

Table 5.1 Cathode and anode composition

Component	**Mass Ratio**	**Source**
Cathode		
$LiMn_2O_4$	90%	Sigma-Aldrich
Super p Carbon blacks	5%	TIMCAL Graphite & Carbon
PVDF	5%	Kureha Chemical Industry Co., Ltd.
Anode		
Graphite	90%	TIMCAL Graphite & Carbon
Super p Carbon blacks	5%	TIMCAL Graphite & Carbon
PVDF	5%	Kureha Chemical Industry Co., Ltd.

All the processes of assembling and dismantling of the cells were carried out in argon atmosphere in a glove box. A small piece of lithium metal is pressed on the Cu strip. In order to prevent the Cu strip from touching the coin cell case, the Cu strip is wrapped by Celgard separator and inserted in between two separators. The coin cell parts are purchased from MTI Corporation. After placing the anode, cathode and lithium reference electrode, the cell is sealed by the hydraulic crimper. The schematic of the three electrode cell is shown in Figure 5.7. Note that in a common procedure, the graphite anode and the LMO cathode are supposed to be placed into coin cell negative case and coin cell positive case respectively, however, due to the electroplating effect[118, 119], in this dissertation, the graphite anode is placed into the coin cell positive case and the LMO cathode is placed into the coin cell negative case. Because the two electrodes are switched, the external applied voltage/current is also switched to be functional.

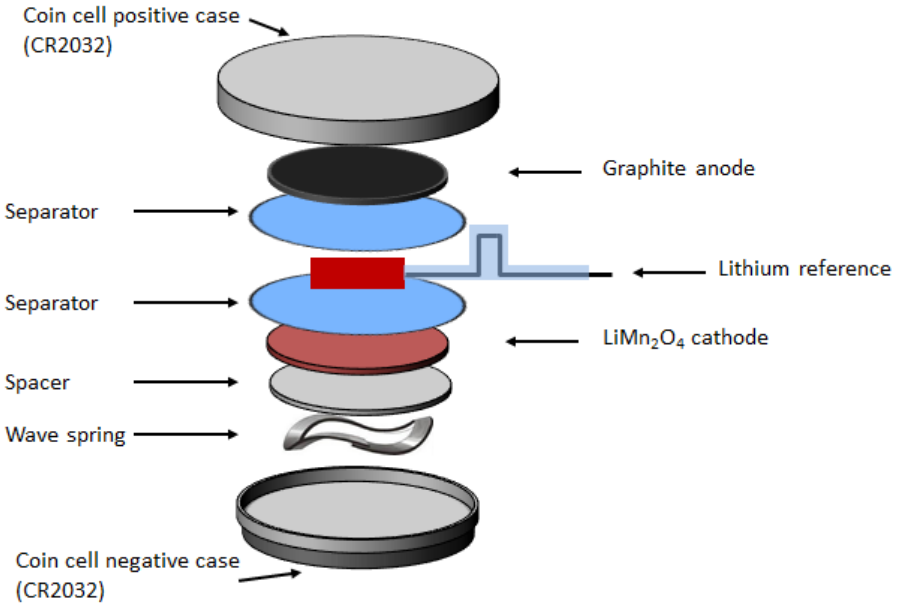

Figure 5.7 Three-electrode coin cell assembly

The electroplating is found when placing the graphite anode in the coin cell negative case as shown in Figure 5.8. After cell assembled in the common procedure, there is a distance between graphite electrode and the coin cell negative case due to the spacer and wave spring. During charging, the potential on the coin cell negative case is slightly lower than the potential of the graphite anode. Therefore, it's likely for lithium ions to get electrons from the coin cell negative case instead of the graphite anode. As shown in Figure 5.8, lithium plating is found on both the wave spring and coin cell negative case in experiments.

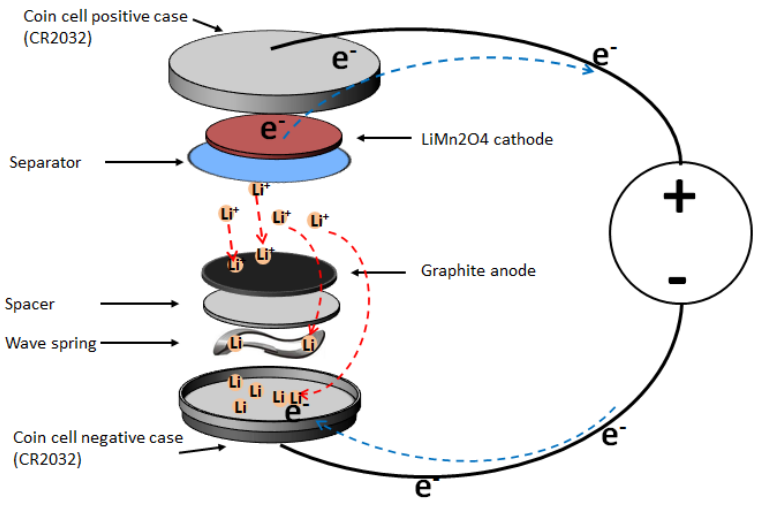

Figure 5.8 Electroplating of lithium on the negative case

By switching the positions of the electrodes, the lithium deposition on the negative case is avoided.

The assembled cells are installed on the Maccor cycler and cycled over a long period of time. The cell is charged with 1C rate until the cutoff voltage of 4.1 V. The voltage is held until the current drops down to 0.1C. Next, the cell is discharged to 3.5 V at 1C, held at 3.4C until the current drops down to 0.1C. The information of the cell current, cell capacity, cell voltage, cathode voltage respect to the lithium reference electrode and the anode voltage respect to the lithium reference electrode are recorded throughout the long term cycling.

Degradation Analysis

The voltage profiles from each electrode with respect to lithium reference electrode over long term cycling are presented in Figure 5.9. Because the electrode voltage versus Li reference electrode is determined by the surface Li concentration of the electrode, the evolution of Li concentration in the electrode can be reflected by the voltage profile. Figure 5.9 shows the voltage evolutions of LMO cathode and graphite anode with mass ratio 0.84 over the 1500 cycles.

The voltage evolution shows three different stages. In the first stage, the voltage from both electrodes shows an increasing trend, and in the second stage, the voltage decreases gradually. And finally in the third stage, cathode voltage reaches 3.5 V and the anode voltage decreases to nearly 0.15V. The voltage swing window also changes as cycle increases. As shown in Figure 5.9, the voltage swing window of cathode expands when cycling, and the voltage swing window of anode shrinks. In the middle of the whole cycling, an uncontrolled discharge happened due to the malfunction of the Maccor cycler, and the cell is discharged to 0 V for about 2 days, which is expected to increase degradation of cathode.

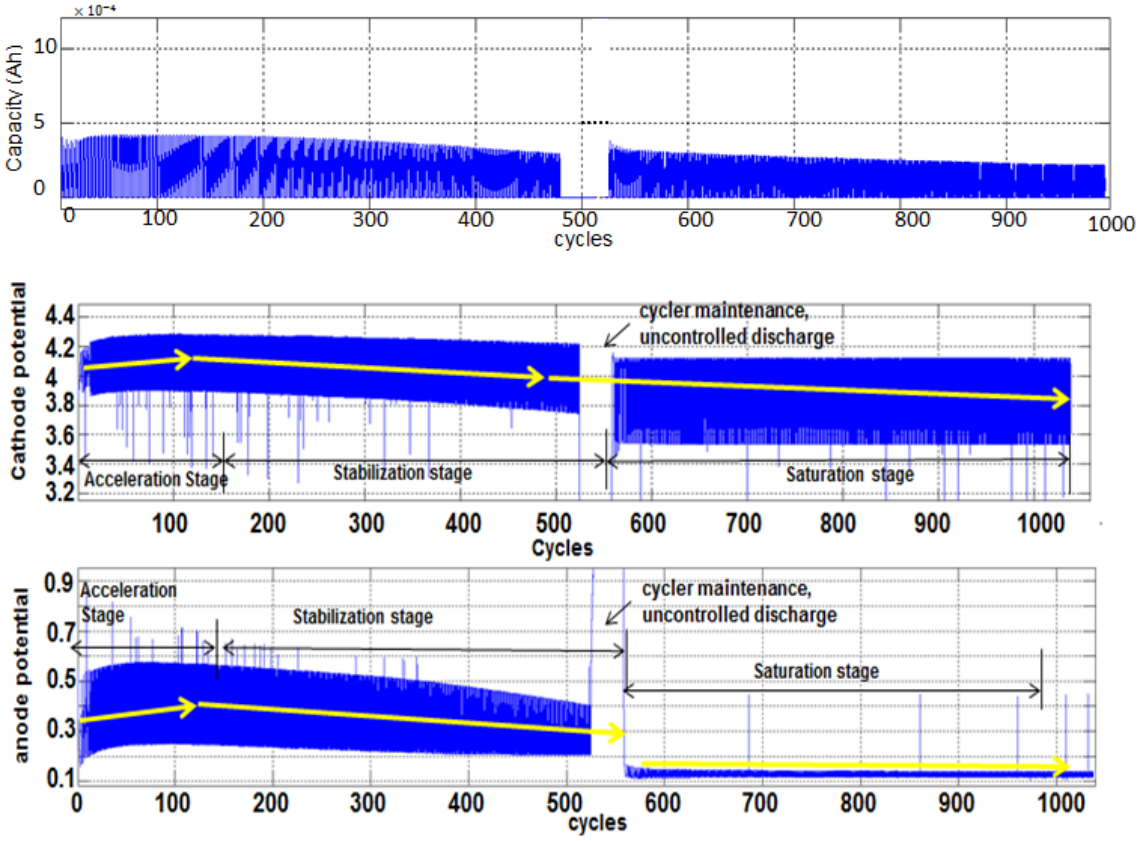

Figure 5.9 Measured charge capacity and voltage from anode and cathode with mass ratio 0.84

Another three-electrode cell with different mass ratio shows the similar pattern as shown in Figure 5.10.

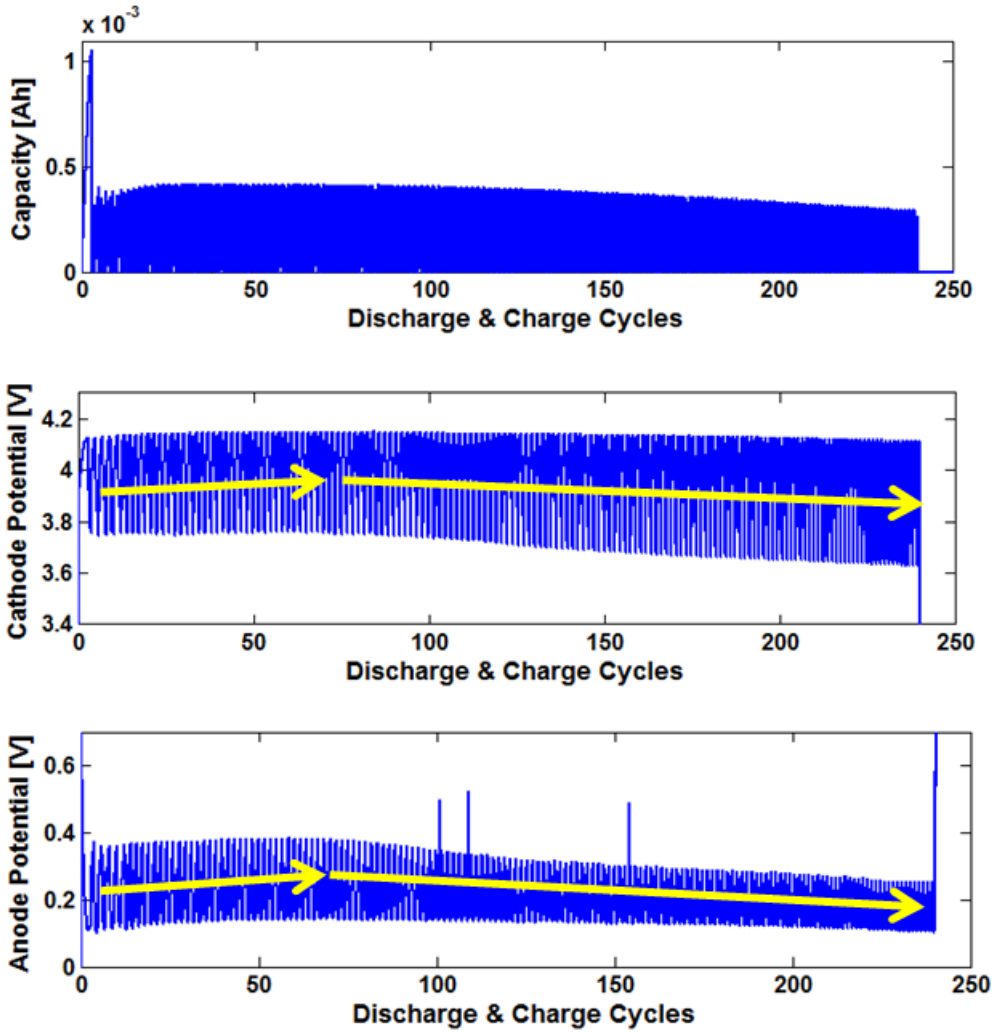

Figure 5.10 Measured charge capacity and voltage from anode and cathode with mass ratio 1.53

5.3.3 Cycled cell examination

After long term cycling, three electrode cells are dissembled and each individual electrode is taken out and examined by SEM and TEM. TEM and SEM are both electron microscopy. However, there is some difference between them. SEM is based on scattered electrons while TEM is based on transmitted electrons[120]. SEM produced the image of the sample by collecting and counting the scattered electrons reflected from the sample. TEM passes the

electrons directly through the sample. The electrons that pass through the sample are the parts that are illuminated in the image. In terms of magnification and resolution, TEM has up to a 50 million magnification level while SEM only offers 2 million as the maximum level of magnification. In this dissertation, SEM is used to examine the cycled electrode at microscale, and TEM is used to examine the cycled electrode further deeper, at the nanoscale.

Cathode examination

First, the cycled cathode is examined by SEM. In order to show the how severe the fracture is in the cathode, a fixed area on the electrode surface is selected and the fracture is examined in this fix area. As shown in Figure 5.11, in a square area, many cracks are found, the center particle shows severe fracture on its surface, the isolated part of the particle is estimated to be about 30% of its total volume. The electrode is also washed by acetone in order to remove the surface attachment, such as, carbon blacks, PVDF, and electrolyte residues. Figure 5.12 shows the fractures on the particle surface after acetone wash. The particle surface is full of fractures. For comparison, the fresh LMO powders are also examined by SEM. As shown in Figure 5.13, the fresh LMO powders have a clean crystal surface without any fractures. Therefore, there is no doubt that the fracture is due to the cycling. The above SEM examination of cycled cathode electrode reveals the fracture is everywhere in the cycled cathode electrode, and is suspected to be the main degradation mechanism of the cathode capacity fade.

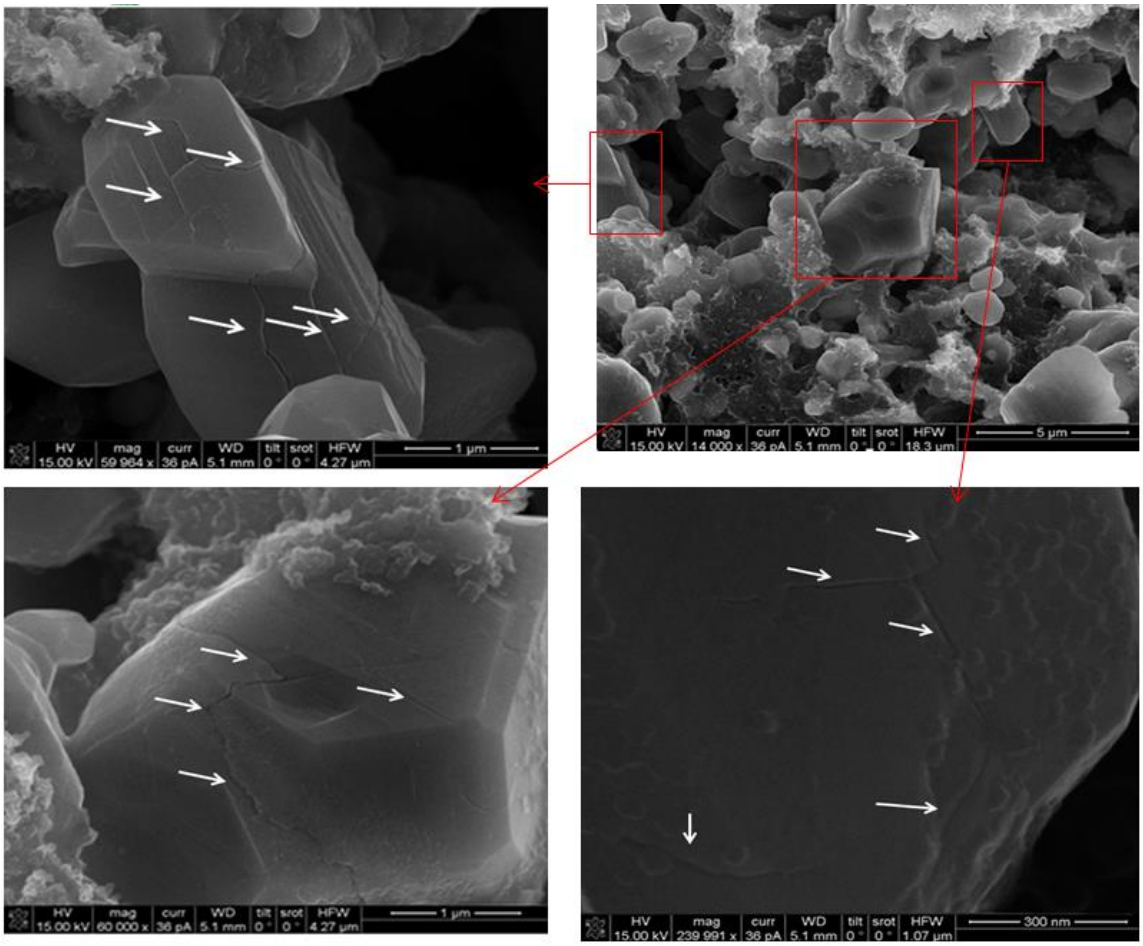

Figure 5.11 SEM measurements of cycled cathode without wash, fractures are found all over the surface

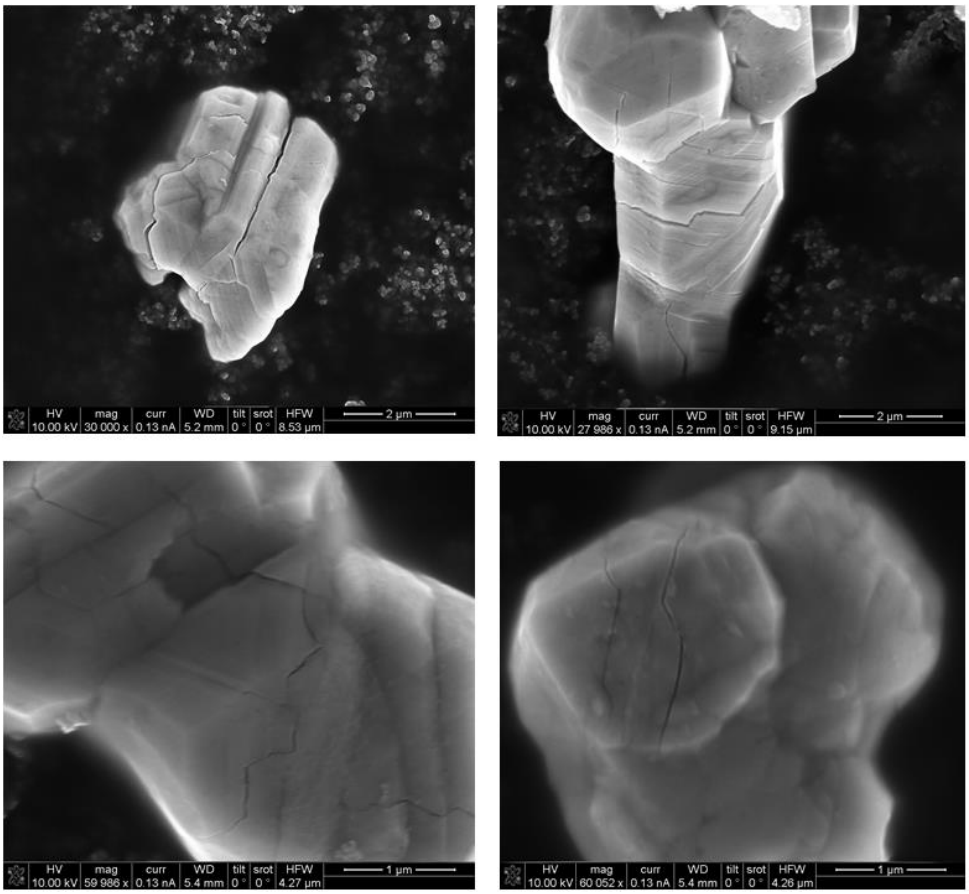

Figure 5.12 SEM measurements of cycled cathode after acetone wash, fractures are found all over the surface

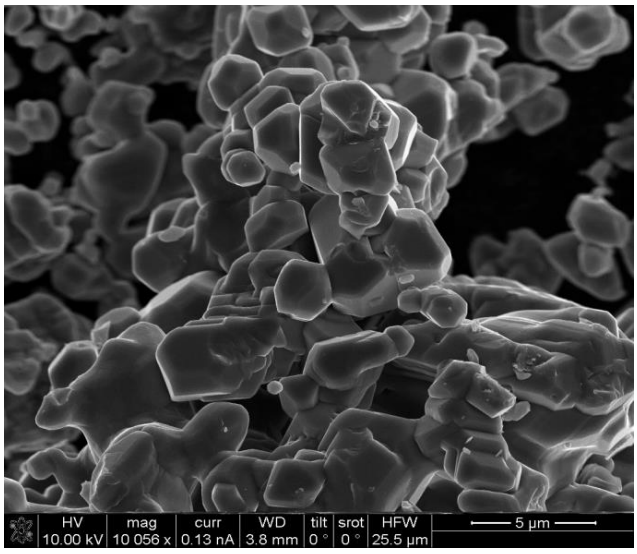

Figure 5.13 SEM image of the fresh $LiMn_2O_4$ powders

The cracks on the particles observed by SEM reveal the importance of fracture in the cathode degradation. TEM is used to provide further information at nanoscale. The particle is washed by acetone, and placed on the TEM grid. The cathode sample is transferred into TEM, and examined. Figure 5.14 shows the TEM images of the single LMO particle. The particle is placed on carbon film of the TEM grid holder. The carbon film is also shown as background in Figure 5.14. The surface of the LMO particle is examined, and nanoscale fractures are found.

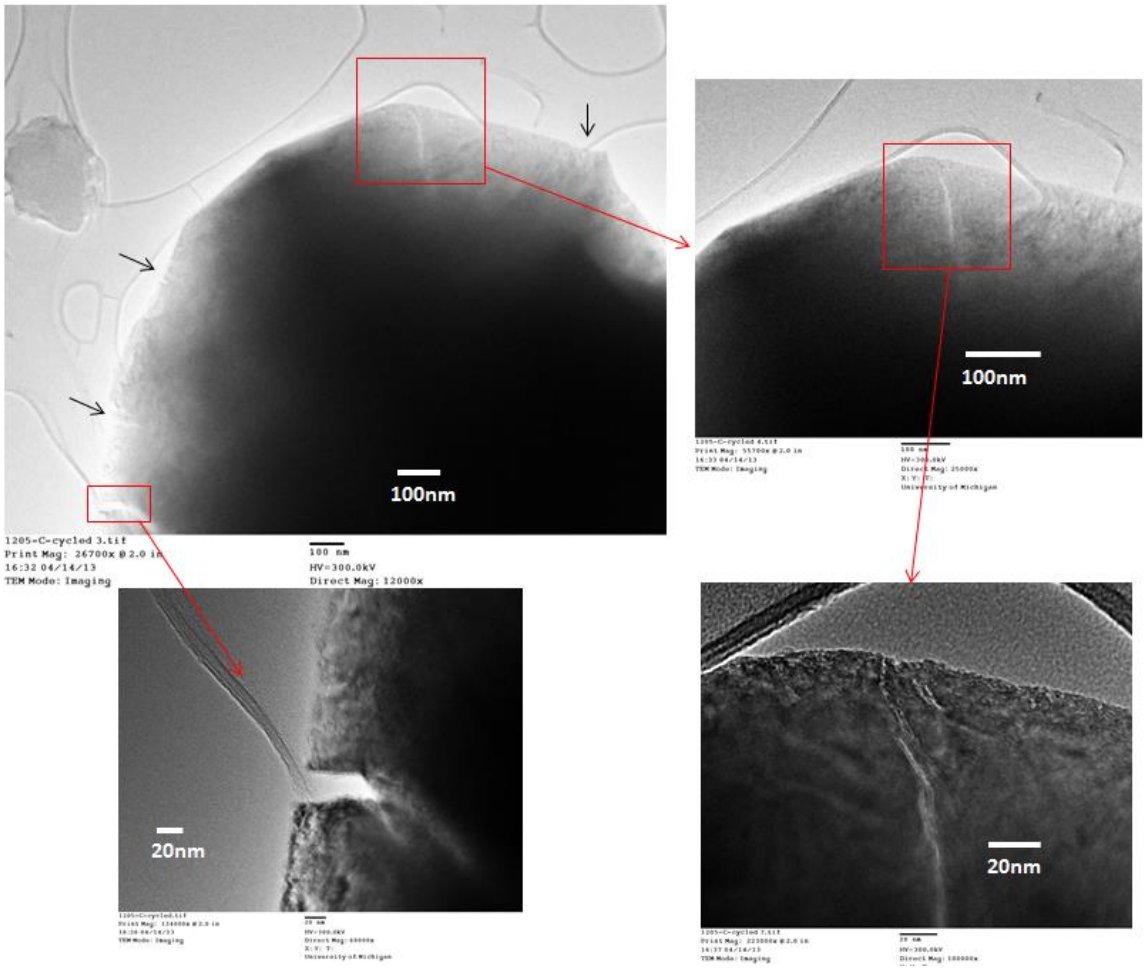

Figure 5.14 TEM images show that nano cracks are found over a single cycled cathode particle

The above TEM examination of cycled cathode electrode reveals the nanoscale fractures are all over the surface. TEM and SEM examinations confirm that the fractures are found

everywhere in the cycled cathode electrode, and are suspected to be the main degradation mechanism of the cathode capacity fade.

Anode examination

Graphite anode is believed to have a significant surface change after cycling[121]. One of the most important degradation mechanisms in the graphite anode is the SEI layer growth[46, 122] which is very likely to change the morphology of the surface morphology of the graphite anode.

The cycled anode electrode is taken out and examined by SEM and TEM to get direct view of the anode structure change and morphology change after cycling.

First, the cycled sample is examined by SEM. Figure 5.15 shows the SEM images of the fresh anode graphite electrode, and cycled anode graphite electrode. The fresh graphite electrode has a clear surface; however, the cycled graphite electrode has a very obvious film covering over all the particles.

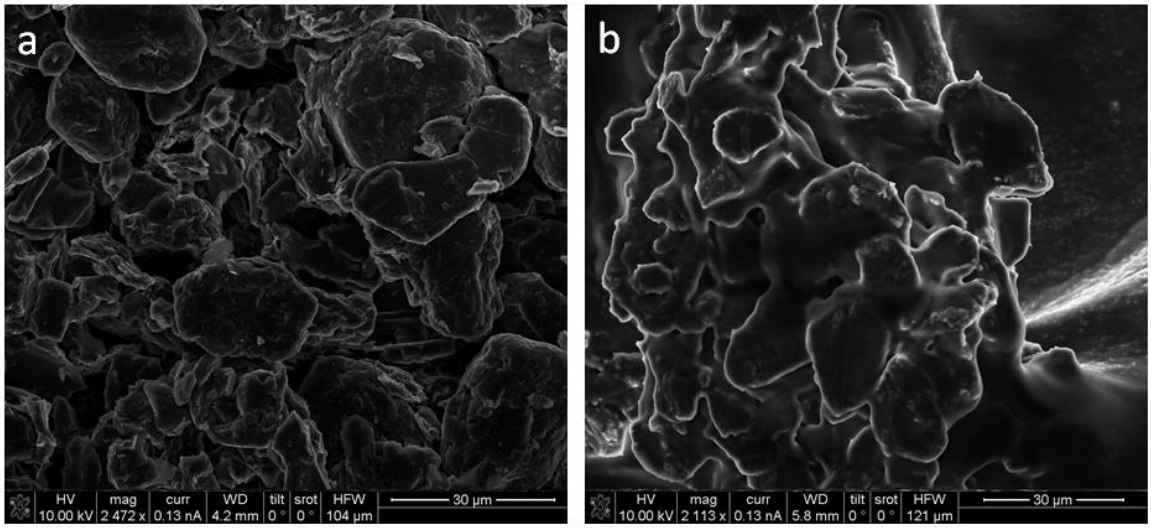

Figure 5.15 SEM images of a) fresh graphite anode with clear surface, and b) cycled graphite anode with SEI film on the surface

The SEI film is observed in SEM images, in order to get the more information, such as, SEI thickness, SEI impact on the graphite structure, TEM is used to investigate deeper. In a common TEM sample preparation procedure, the sample particle milled by ion beam to the thickness of several nanometers, however, this procedure is likely to damage the SEI layer or graphite structure. In order to protect the particle, we avoid milling the sample by looking at the particle edge of which the thickness is small enough for electrons to pass. Cycled graphite particles are directly placed into the TEM grid without acetone wash. Figure 5.16 shows the TEM images of the cycled graphite particle. The SEI layer is clearly shown on the surface of graphite. The morphology of the SEI layer is amorphous. The thickness of SEI layer varies from location to location.

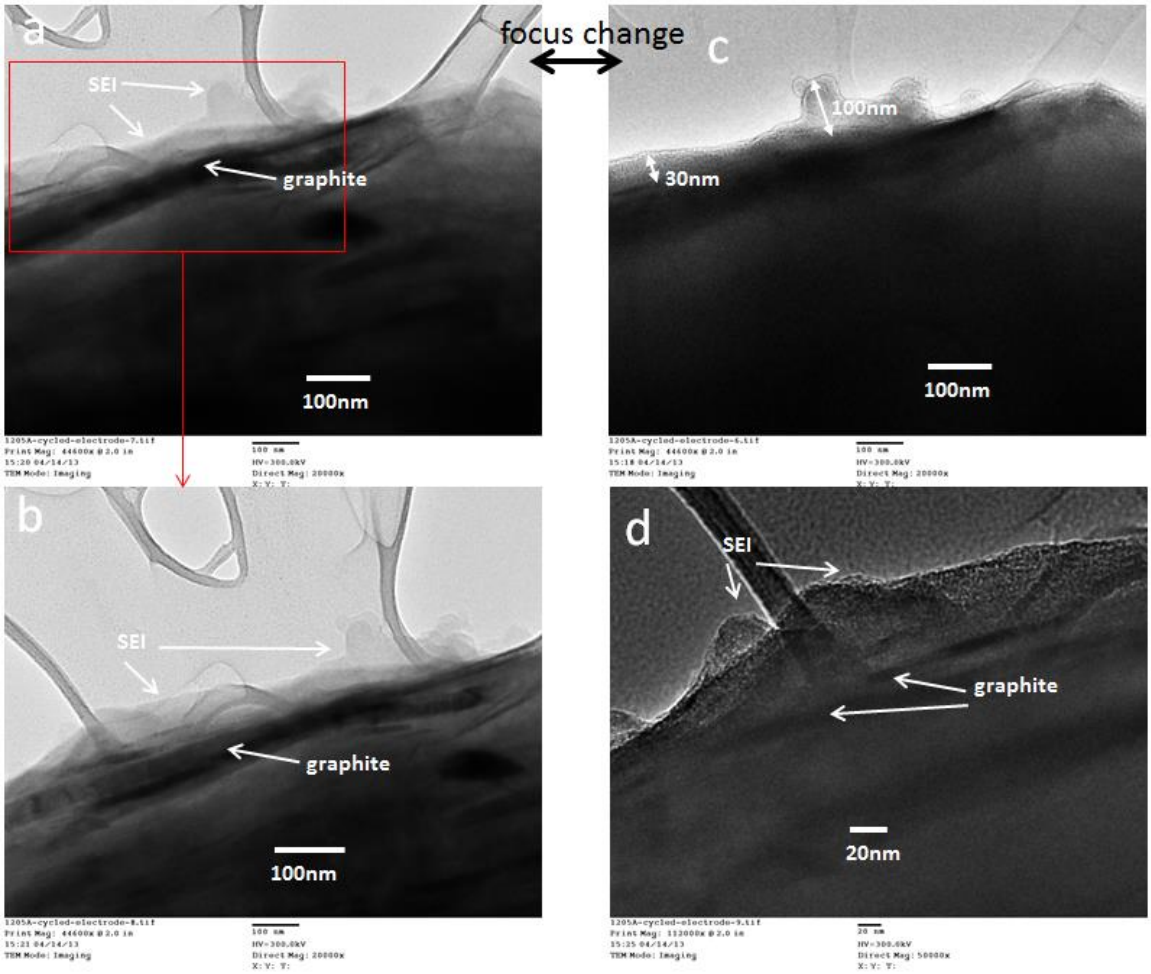

Figure 5.16 TEM images show SEI film on the graphite surface; a) and c) show the same location with different focus, the thickness of SEI varies from 30 nm to 100 nm; b) shows a magnified view of a rectangle area in a); d) shows the SEI layer in another location

Carbon blacks are also found in the TEM images as shown in Figure 5.17. The carbon blacks have about 40~50 nm diameter. Carbon blacks are found to not only stay on the surface of the graphite, but also underneath the graphite.

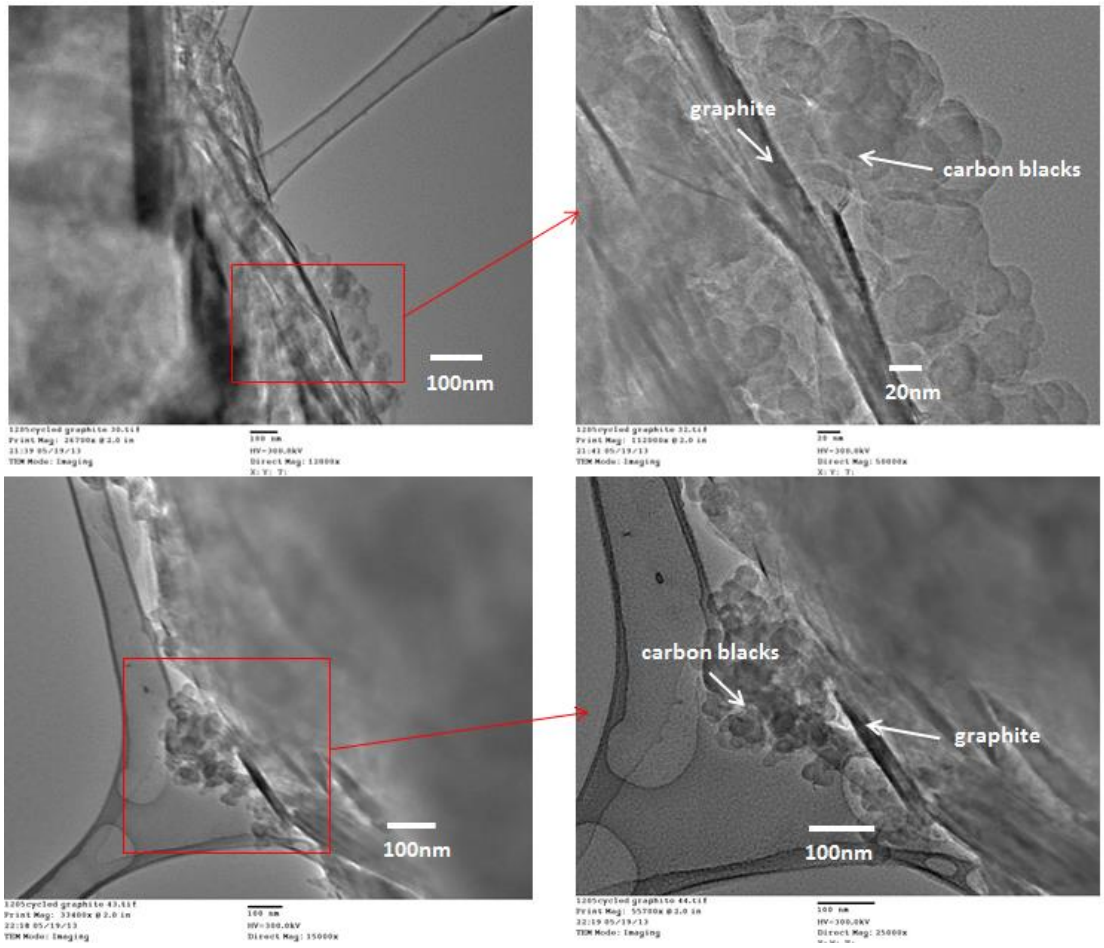

Figure 5.17 TEM images show the carbon blacks on the graphite surface

The SEI film is found all over the surface of graphite particles. Deeper investigation reveals that the graphite particle is exfoliated after cycling. Several studies have been done to elucidate the origin of graphite exfoliation. Usually, solvent cointercalation is attributed to have an important role in the graphite exfoliation [123-125]. However, the TEM results from this dissertation show another important role in the graphite exfoliation, that is the SEI growth. Figure 5.18 and Figure 5.19 show the TEM images that reveal the different patterns of graphite exfoliation in the cycled anode electrode.

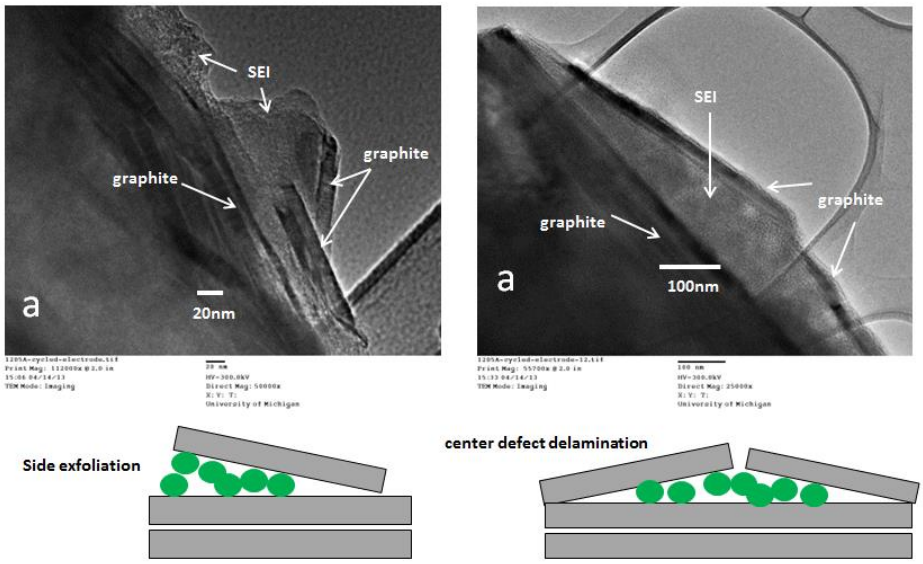

Figure 5.18 TEM images show the graphite exfoliation, a) side exfoliation, b) center exfoliation

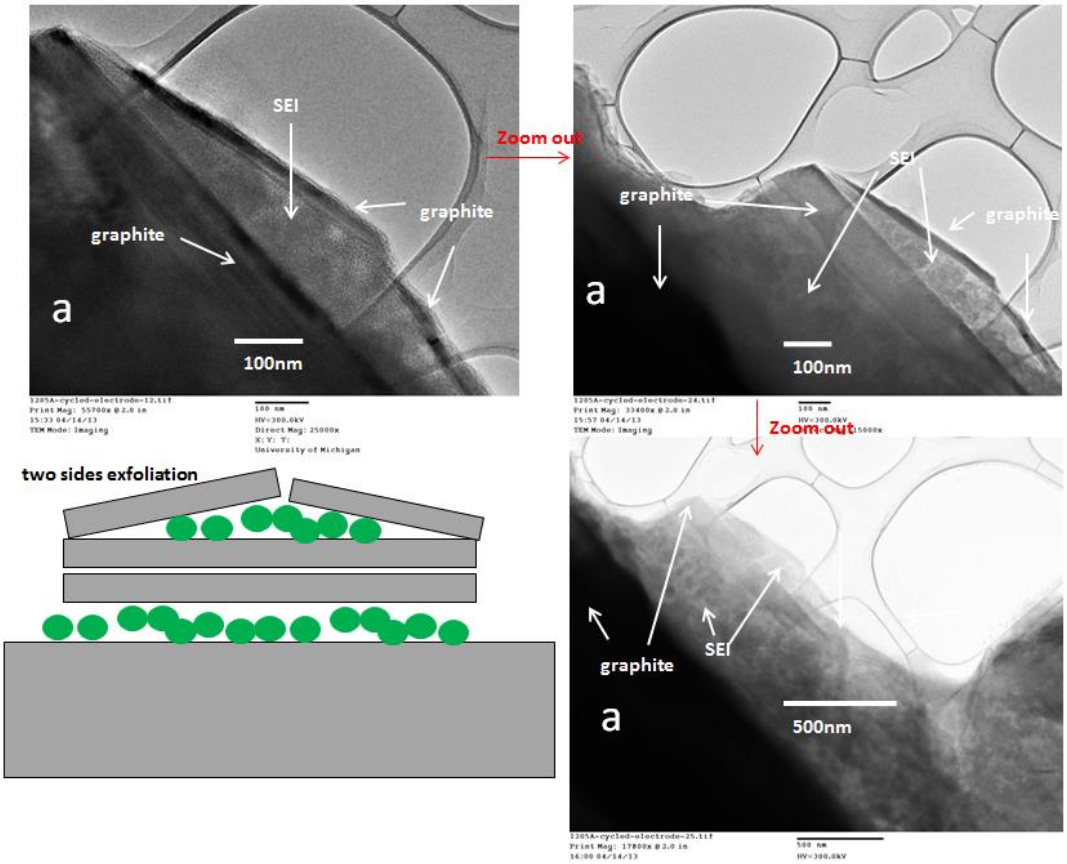

Figure 5.19 TEM images show two sides exfoliation of graphite

Figure 5.18 a) shows that SEI layer seems to grow into the graphite layer from the side and the graphite layer is delaminated. Figure 5.18 b) shows a clear view of SEI grows into the graphite layer from a top defect, and the graphite layer is delaminated from the center point. Figure 5.19 shows that the SEI layer can grow from both sides of a big piece of graphite, and finally separate this piece of graphite from the bulk graphite. In this case, the delamination is from both sides. And the capacity loss due the graphite isolation is significant.

Through the above SEM and TEM investigation, it's believed that the SEI growth and the graphite exfoliation are the suspected to be the major contributors in the anode electrode capacity fade. The SEI growth not only consumes the cyclable lithium and therefore reduces the total available lithium ion the battery system, and also increase the internal resistance increase. The role of SEI growth in the graphite exfoliation is a potential future topic.

5.3.4 Cathode fracture augment

As shown in the previous section, cathode fracture has been observed frequently over the particle surface. In 4.2.2, the change of the usable volume fraction is hypothesised to be propotional to the change of the solid phase volume fraction. With SEM and TEM observation, the fracture is highly likely to lead to usable volume fraction reduction. Therefore, in order to better reflect the real degradation mechanism, the change of the usable volume fraction updated to be propotional to the hydrostatic stress induced by the lithium intercalation/deintercalation, namely

$$\varepsilon_{usable0}^{pos} = \varepsilon_{1,ini}^{pos} \text{ at } t=0, \tag{5.1}$$

$$\frac{d\varepsilon_{usable}^{pos}}{dt} = k_{iso}\sigma_h \tag{5.2}$$

where k_{iso} is a coefficient, σ_h is the hydrostatic stress induced by the lithium intercalation/deintercalation. The details about the stress generation inside the particle will be introduced in the following section.

Stress induced particle fracture in cathode

Stress induced particle fracture is one of the important degradation mechanisms in cathode[126].

The lattice constants changes as Li intercalates into or deintercalates out of $LiMn_2O_4$ particle. Figure 5.20 shows the lattice constant variation as a function of Li stoichiometry [45]. The lattice constant change may be assumed to change linearly with Li stoichiometry[127, 128].

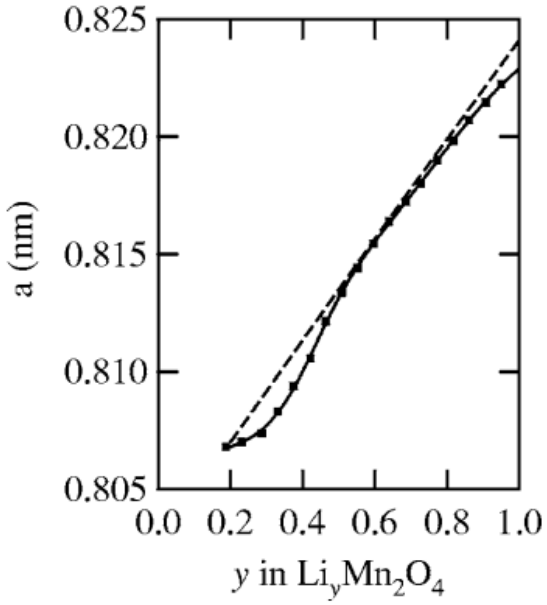

Figure 5.20 Lattice parameter change as a function of Li stoichiometry (squares) measured by Amatucci *et al.*[127]; The dashed curve is the lattice parameter change assuming constant partial molar volumes

Stress is generated when lithium intercalation/deintercalation induced lattice change is not uniform. Prussin [129] studied the stress generated by diffusion in a wafer. He made an analogy between concentration and temperature. And the stresses caused by concentration gradients are

treated to be similar to those caused by temperature gradients in an otherwise unstressed body. The classic equations describing the thermal effects on the stress-strain relations are expressed below[130].

$$\varepsilon_{xx} - \alpha T = \frac{1}{E}\left[\sigma_{xx} - v(\sigma_{yy} + \sigma_{zz})\right]. \tag{5.3}$$

$$\varepsilon_{yy} - \alpha T = \frac{1}{E}\left[\sigma_{yy} - v(\sigma_{xx} + \sigma_{zz})\right]. \tag{5.4}$$

$$\varepsilon_{zz} - \alpha T = \frac{1}{E}\left[\sigma_{zz} - v(\sigma_{xx} + \sigma_{yy})\right]. \tag{5.5}$$

$$\varepsilon_{xy} = \frac{\sigma_{xy}}{2G}\ \varepsilon_{yz} = \frac{\sigma_{yz}}{2G}\ \varepsilon_{xz} = \frac{\sigma_{xz}}{2G} \tag{5.6}$$

where ε_{ij} are strain components, $\sigma_{ij}$are stress components, E isYoung's modulus, v is Poisson's ratio, G is modulus of elasticity in shear, α is thermal expansion coefficient, and T is the temperature change from the original value. Timoshenko *et al*.[130] modified the equations for thermal effect to concentration effect by replacing temperature T with concentration c, and replacing thermal expansion coefficient α with concetration expansion coefficient $\frac{\Omega}{3}$ (partial molar volume/3). Note that, for small expansions, the volumetric expansion coefficient is three times the linear coefficient. Therefore, the equations for stress-strain relations with existing of concentration gradients can be expressed as follows.

$$\varepsilon_{xx} = \frac{1}{E}\left[\sigma_{xx} - v(\sigma_{yy} + \sigma_{zz})\right] + \frac{\tilde{c}\Omega}{3}. \tag{5.7}$$

$$\varepsilon_{yy} = \frac{1}{E}\left[\sigma_{yy} - v(\sigma_{xx} + \sigma_{zz})\right] + \frac{\tilde{c}\Omega}{3}. \tag{5.8}$$

$$\varepsilon_{zz} = \frac{1}{E}\left[\sigma_{zz} - v(\sigma_{xx} + \sigma_{yy})\right] + \frac{\tilde{c}\Omega}{3}. \tag{5.9}$$

$$\varepsilon_{xy} = \frac{\sigma_{xy}}{2G}\ \varepsilon_{yz} = \frac{\sigma_{yz}}{2G}\ \varepsilon_{xz} = \frac{\sigma_{xz}}{2G} \tag{5.10}$$

By using delta function, δ_{ij}, the above equations can be simplified to one equation shown below[131].

$$\delta_{ij} = \begin{cases} 1 & i = j \\ 0 & i \neq j \end{cases} \tag{5.11}$$

$$\sigma_{kk} = \sigma_{11} + \sigma_{22} + \sigma_{33} \tag{5.12}$$

$$\varepsilon_{ij} = \frac{1}{E}\left[(1+v)\sigma_{ij} - v\sigma_{kk}\delta_{ij}\right] + \frac{\tilde{c}\Omega}{3}\delta_{ij}. \tag{5.13}$$

where $\tilde{c} = \mathrm{c} - c_0$ is the concentration change from the original stress free value.

The above equation can be rearranged to get the stress components.

$$\sigma_{ij} = 2\mu\varepsilon_{ij} + (\lambda\varepsilon_{kk} - \beta\tilde{c})\delta_{ij} \tag{5.14}$$

where $\mu = \frac{E}{2(1+v)}$, $\lambda = \frac{2v\mu}{1-2v}$, and $\beta = \frac{\Omega(3\lambda+2\mu)}{3}$.

The relation between strain tensor and displacement is expressed as [130]

$$\varepsilon_{ij} = \frac{1}{2}\left(\frac{\partial u_i}{\partial x_j} + \frac{\partial u_j}{\partial x_i}\right) \tag{5.15}$$

In this dissertation, the body forces are neglected, thefore, the equilibrium equation is expressed by [130]

$$\sigma_{ij,i} = 0 \ (j = 1,2,3) \tag{5.16}$$

The displacement equations can be obtained by substitution of Eq. (5.14) and (5.15) into Eq. (5.16), as expressed below [132].

$$\mu\nabla^2 u_i + (\lambda + \mu)u_{k,ki} - \beta\tilde{c}_{,i} = 0 \ (i = 1,2,3) \tag{5.17}$$

The boundary condition for the particle surface is traction-free which can be expressed as follows[132].

$$p_{nx} = \sigma_{xx}l + \sigma_{yx}m + \sigma_{zx}n = 0 \tag{5.18}$$

$$p_{ny} = \sigma_{xy}l + \sigma_{yy}m + \sigma_{zy}n = 0 \tag{5.19}$$

$$p_{nz} = \sigma_{xz} l + \sigma_{yz} m + \sigma_{zz} n = 0 \tag{5.20}$$

where l, m, n denote the direction cosines between the external normal and each axis. Substitution of Eq. (5.14) and (5.15) into boundary conditions Eq. (5.18), (5.19), and (5.20) yields

$$\mu\left(u_{i,j} + u_{j,i}\right) n_j + (\lambda u_{k,k} - \beta c) n_i = 0 \ (i = 1,2,3) \tag{5.21}$$

where $n_1 = l$, $n_2 = m$ and $n_3 = n$. Therefore, the onlye equations need to be solved are Eq. (5.17), and the boundary condition of Eq. (5.21).

The concentration profile is needed in order to calculate the stress generation inside the particle throught Eq. (5.14). The mass transportation inside the particle is modeled as a diffusion process. And the driving force for Lithium diffusion is the chemical potential gradient as shown below.

$$\mathrm{v} = -M \nabla \mu \tag{5.22}$$

where M is the mobility, and μ is the chemical potential of lithium. The Lithium flux can then be written as

$$\mathrm{J} = \mathrm{cv} = -Mc \nabla \mu \tag{5.23}$$

where c is the lithium concentration.

Based on the thermodynamics, the electrochemical potential in an ideal solid solution can be expressed as[131]

$$\mu = \mu_0 + \mathrm{RT} \ln X - \Omega \sigma_h \tag{5.24}$$

$$\sigma_h = \frac{\sigma_{11} + \sigma_{22} + \sigma_{33}}{3} \tag{5.25}$$

where μ_0 is a constant, R is gas constant, T is absolute temperature, X is the molar fraction of lithium ion, Ω is partial molar volume of lithium ion, and σ_h is the hydrostatic stress.

By assuming temperature is constant, substitute Eq. (5.24) into Eq. (5.23) to get the following equation.

$$\nabla(RT\ln X) = \mathrm{RT}\frac{1}{X}\nabla X = RT\frac{1}{c}\nabla c \tag{5.26}$$

And the flux equation can be obtained as follows

$$\mathrm{J} = -\mathrm{D}(\nabla \mathrm{c} - \frac{\Omega c}{RT}\nabla\sigma_h) \tag{5.27}$$

where $\mathrm{D} = MRT$ is diffusion coefficient. The mass conservation law gives

$$\frac{\partial \mathrm{c}}{\partial \mathrm{t}} + \nabla \cdot \mathrm{J} = 0 \tag{5.28}$$

By substituting Eq. (5.27) into Eq. (5.28), we get

$$\frac{\partial \mathrm{c}}{\partial \mathrm{t}} = \mathrm{D}(\nabla^2 \mathrm{c} - \frac{\Omega}{RT}\nabla \mathrm{c}\cdot\nabla\sigma_h - \frac{\Omega c}{RT}\nabla^2\sigma_h) \tag{5.29}$$

The flux boudnary condition is

$$\mathrm{J} = -\mathrm{D}\left(\nabla \mathrm{c} - \frac{\Omega c}{RT}\nabla\sigma_h\right) = \frac{i_n}{F} \tag{5.30}$$

where i_n is the current density on the particle surface and F is Faraday's constant.

In order to implement the stress generation into the cell level model, equations of stress generation for 1D spherical particle are derived. In 1D case, the stress tensor for a spherical particle has two independent variables, radial stress σ_r and tangential stress σ_t. The equilibrium equation corresponding to Eq. (5.16) becomes,

$$\frac{\mathrm{d}\sigma_r}{\mathrm{dr}} + \frac{2}{r}(\sigma_r - \sigma_t) = 0 \tag{5.31}$$

And the equations for stress-strain relation cosressponding to Eq. (5.13) become

$$\varepsilon_r = \frac{1}{E}(\sigma_r - 2\mathrm{v}\sigma_t) + \frac{\Omega}{3}\tilde{c} \tag{5.32}$$

$$\varepsilon_t = \frac{1}{E}[\sigma_t - \mathrm{v}(\sigma_r + \sigma_t)] + \frac{\Omega}{3}\tilde{c} \tag{5.33}$$

The equation for strain-displacement relations corresponding to Eq. (5.15) becomes

$$\varepsilon_r = \frac{\mathrm{du}}{\mathrm{dr}} \quad \varepsilon_t = \frac{\mathrm{u}}{\mathrm{r}} \tag{5.34}$$

And the equation for displacement corresponding to Eq. (5.17) can be rewritten as

$$\frac{d^2u}{dr^2} + \frac{2}{r}\frac{du}{dr} - \frac{2u}{r^2} = \frac{1+\mathrm{v}}{1-v}\frac{\Omega}{3}\frac{\mathrm{d}\tilde{c}}{\mathrm{dr}} \tag{5.35}$$

The stress may be obtained by integrating the above equation. Noting that the radial stress is zero at the particle surface. The two stress variables can be obtained as shown below.

$$\sigma_r = \frac{2\Omega E}{3(1-v)}\left(\frac{1}{r_0^3}\int_0^{r_0}\tilde{c}r^2dr - \frac{1}{r^3}\int_0^{r}\tilde{c}r^2dr\right) \tag{5.36}$$

$$\sigma_t = \frac{\Omega E}{3(1-v)}\left(\frac{2}{r_0^3}\int_0^{r_0}\tilde{c}r^2dr + \frac{1}{r^3}\int_0^{r}\tilde{c}r^2dr - \tilde{c}\right) \tag{5.37}$$

The equation for the diffusion process corresponding to Eq. (5.29) can be obtained as follows.

$$\frac{\partial c}{\partial t} = D\left[\frac{\partial^2 c}{\partial r^2} + \frac{2}{r}\frac{\partial c}{\partial r} - \frac{\Omega}{RT}\frac{\partial c}{\partial r}\frac{\partial \sigma_h}{\partial r} - \frac{\Omega c}{RT}\left(\frac{\partial^2 \sigma_h}{\partial r^2} + \frac{2}{r}\frac{\partial \sigma_h}{\partial r}\right)\right] \tag{5.38}$$

The hydrostatic stress is obtained by Eq.(5.36) and Eq. (5.37).

$$\sigma_h = \frac{\sigma_r + 2\sigma_t}{3} = \frac{2\Omega E}{9(1-v)}\left(\frac{3}{r_0^3}\int_0^{r_0}\tilde{c}r^2dr - \tilde{c}\right) \tag{5.39}$$

Substitute Eq. (5.39) into Eq. (5.38), we get

$$\frac{\partial c}{\partial t} = D\left[\frac{\partial^2 c}{\partial r^2} + \frac{2}{r}\frac{\partial c}{\partial r} + \theta\left(\frac{\partial c}{\partial r}\right)^2 + \theta c\left(\frac{\partial^2 c}{\partial r^2} + \frac{2}{r}\frac{\partial c}{\partial r}\right)\right] \tag{5.40}$$

$$\theta = \left(\frac{\Omega}{RT}\right)\left[\frac{2\Omega E}{9(1-v)}\right] \tag{5.41}$$

The boundary fux equation can be obtain by substituting Eq.(5.39) into Eq. (5.30)

$$\mathrm{J} = -D(1+\theta c)\frac{\partial c}{\partial r} = \frac{i_n}{F}, at\ r = r_0 \tag{5.42}$$

Therefore, the stress generation and the diffusion process are decoupled. In order to get the sterss, the concentration profile should be calculated first.

5.3.5 Degradation model calibration and validation

Degradation model is calibrated against the data from the three electrode cell cycling. The cathode electrode potential and anode electrode potential are used to calibrate the degradation model, after calibration, capacity fade data is used to validate the model prediction. The parameters used in the degradation model are listed in Table 5.2. The first part of the parameters is from experiment measurements and also the reference. The end part of the parameters is determined by calibration.

Table 5.2 Battery parameters and calibration

Parameter	Expressions	Unit	Description	Source
L_neg	100×10^{-6}	m	Length of negative electrode	Experiment
L_sep	20×10^{-6}	m	Length of separator	Experiment
L_pos	118×10^{-6}	m	Length of positive electrode	Experiment
D1_neg	3.9×10^{-14}	m^2/s	Solid phase Li-diffusivity Negative	[27]
D1_pos0	1×10^{-13}	m^2/s	Solid phase Li-diffusivity Positive	[27]
rp_neg	10×10^{-6}	m	Particle radius Negative	Experiment
rp_pos	2.5×10^{-6}	m	Particle radius Positive	Experiment
Sa_neg	$3 \cdot (eps1\_neg)/rp\_neg$		Specific surface area Negative	[27]
brug	1.5		Bruggeman coefficient	[27]
Rg	8.314	$J/(mol \cdot K)$	Gas constant	[27]
Far	96487	$s \cdot A/mol$	Faraday's constant	[27]
t_plus	0.363		Cationic transport number	[27]
D2	7.5×10^{-11}	m^2/s	Salt diffusivity in Electrolyte	Experiment
eps1_pos0	1-eps2_pos0-0.259		Positive solid phase volume fraction	[27]
eps2_sep	1		Separator porosity	Experiment
eps2_pos0	0.48		Positive electrolyte volume fraction	Experiment
K1_pos	3.8	S/m	Solid phase conductivity Positive	Experiment
K1_neg	100	S/m	Solid phase conductivity Negative	Experiment

c20	2000	mol/m^3	Initial electrolyte salt concentration	Experiment
dlnfdlnc	0		Activity factor concentration variation	[27]
brug1	1.5		Solid phase Bruggemann coefficient	[27]
eps1_neg	1-eps2_neg-0.172		Negative solid phase volume fraction	[27]
eps2_neg	0.52		Negative electrolyte volume fraction	Experiment
c1max_neg	26390	mol/m^3	Max solid phase concentration Negative	[27]
c1max_pos	22860	mol/m^3	Max solid phase concentration Positive	[27]
soc0_neg	300[mol/m^3]/c1max_neg		Initial Negative State of Charge	Experiment
soc0_pos	22500[mol/m^3]/c1max_pos		Initial Positive State of Charge	Experiment
k_neg	2×10^{-11}	m/s	Reaction rate coefficient Negative	[27]
k_pos	2×10^{-11}	m/s	Reaction rate coefficient Positive	[27]
aA_pos	0.5		Reaction rate coefficient Positive	[27]
aC_pos	0.5		Reaction rate coefficient Positive	[27]
aA_neg	0.5		Reaction rate coefficient Negative	[27]
aC_neg	0.5		Reaction rate coefficient Negative	[27]
omega	3.5×10^{-6}	m^3/mol	Partial molar volume	[126]
pois	0.3		Poisson's ratio	[126]
E_pos	10	GPa	Young's modulus	[126]
E_max	4	V	Charge cutoff voltage	Experiment
E_min	3.4	V	Discharge cutoff voltage	Experiment
I0	20	A/m^3	Oxidation rate coefficient	Calibrattion
k3	2×10^{-9}	m/s	Dissolution rate coefficient	Calibrattion
k_iso_ch	2.5×10^{-15}	$1/(Pa \cdot s)$	Isolation rate during charge	Calibrattion
k_iso_dis	80×10^{-14}	$1/(Pa \cdot s)$	Isolation rate during discharge	Calibrattion
k_fs	4×10^{-10}	m/s	SEI growth rate coefficient	Calibrattion
lamda	1.2×10^{7}	1/m	SEI decay coefficient	Calibrattion
k_SEI	3×10^{2}	$ohm \cdot m$	SEI resistant coefficient	Calibrattion

The first part of shift is due to SEI growth, in the first part, the SEI parameters are adjusted in order to match the shift. And the latter, due to the growth of SEI layer, which reduces the reaction rate of the SEI growth, and cathode degradation, becomes the main contributor for the voltage shift later on. And the parameters related to the cathode side reaction are adjusted to meet the shift of the cathode and anode potential shift. After the calibration, the comparison between real data and simulation of cathode anode potential are shown Figure 5.21.

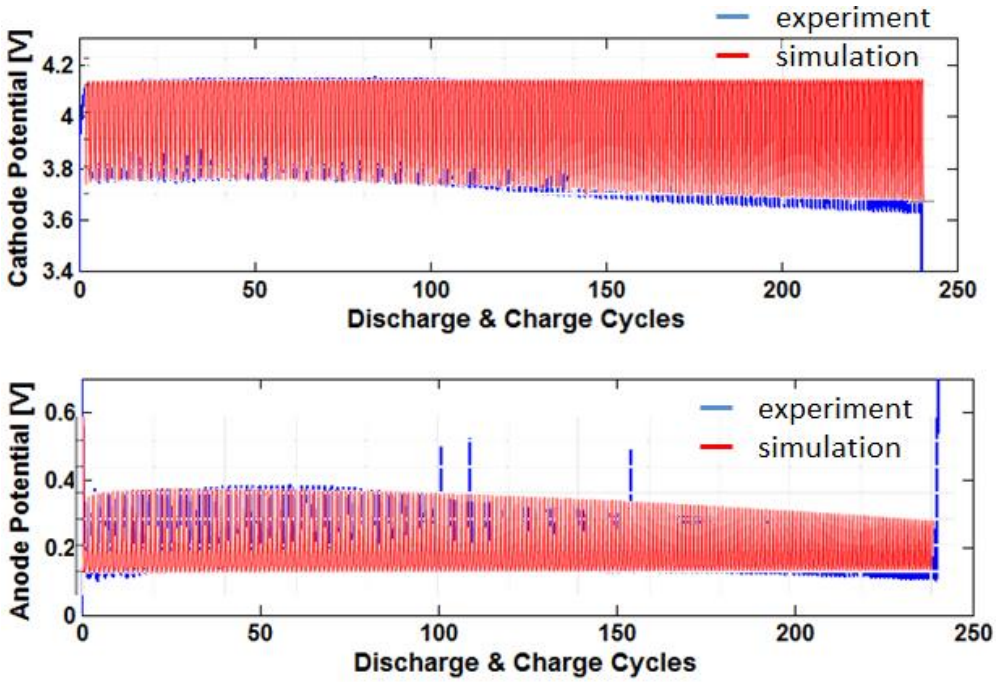

Figure 5.21 Model calibration against cathode and anode potentials

The calibrated model is run over 240 cycles, and the capacity prediction is compared with experimental data. As shown in Figure 5.22. The data and prediction has very good match. The model parameters calibrated are used in the battery health optimization process.

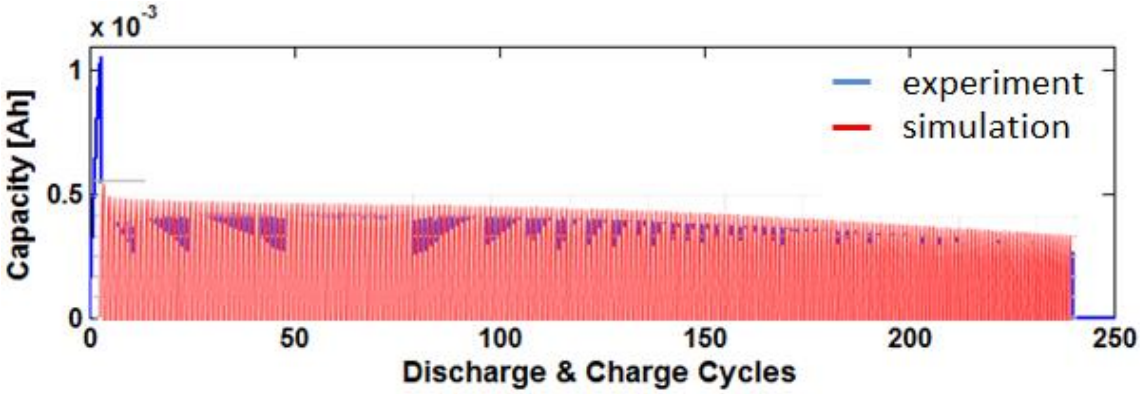

Figure 5.22 Comparison of capacity fade between simulation and experiment

5.4 Summary

This chapter utilizes experiment tools to investigate the capacity fade of Li-ion batteries. Three electrode cells are designed and the cycled data is analyzed to study the degradation pattern. TEM and SEM are employed to investigate the degradation mechanisms in each individual electrode.

From the TEM and SEM results, the SEI growth and graphite exfoliation are the two major degradation mechanisms in the anode electrode. Fracture is found everywhere in cycled cathode electrode. It's believed that the fracture is one of the most important degradation mechanisms in the cathode electrode.

Our study shows that the capacity fade can be divided into three stages: acceleration, stabilization, and saturation. This work provides the experimental evidence for the modeling framework.

Chapter 6
Fracture Impact Analysis Based On Single Particle Model

6.1 Introduction

Local fractures in Li-ion batteries have been experimentally observed in the cycled cathode electrodes[43]. As discussed in previous chapter, SEM and TEM have shown severe fractures on the LMO particles of the cycled cathode electrode. The fracture is believed to be one of the most important degradation mechanisms in cathode electrode. Several models have been developed to determine the stress generated by lithium intercalation and deintercalation[113, 133, 134]. And the relationships have been established between stress levels within cathode particles and parameters such as current density, voltage and particle size[135]. Analytical expressions have been constructed to capture the stress evolution in spherical electrode particles under galvanostatic or potentiostatic conditions[126]. However, the fracture impact on the capacity fade has not been well understood. The classic model for the LMO only considers the diffusion in the single particle, and assumes that the electron conductivity is not the limiting factor. However, due to the low conductivity of the LMO material, especially, when fracture exists, the lithium transportation in LMO material is not only controlled by diffusion, but also migration.

In this chapter, our objectives are as follows:

1) Develop a physics based single particle model with fracture.
2) Determine the effect of particle fracture on the lithium transportation
3) Determine the SOC impact on the fracture

Figure 6.1 shows the comparison of SEM images between fresh LMO cathode and cycled ones. Figure 6.1 (a) and (b) show the fresh LMO electrode with clear surfaces. Figure 6.1 (c) and

(d) clearly show the fractures on the particles after about 1000 cycles. One possible cause of fracture in the LMO particle is the high stress induced by lithium intercalation/deintercalation, especially at high charge/discharge rates. A substantial amount of work has gone into understanding stress generation and fracture propagation in cathode electrodes. Zhang *et al*.[126] developed a three dimensional stress model to systematically study intercalation-induced stress in the cathode particles. They investigated the lithium intercalation-induced stress at different particles sizes and aspect ratios and suggested that smaller sizes are desirable for reducing intercalation-induced stress during the cycling of lithium ion batteries. Later, Zhu *et al*.[135] conducted fracture analysis by using the extended finite element method in order to evaluate the effects of current density, particle size and particle aspect ratio on fracture propagation. Their study shows that current density and particle size are positively correlated with fracture propagation, though not monotonically. All the above research has elucidated stress generation and fracture propagation in the cathode particle under different conditions. However, no direct relationship between fracture and capacity fade has yet been established for the cathode particles under different conditions. The impact of fracture on cathode capacity fade during discharge/charge cycles remains to be investigated.

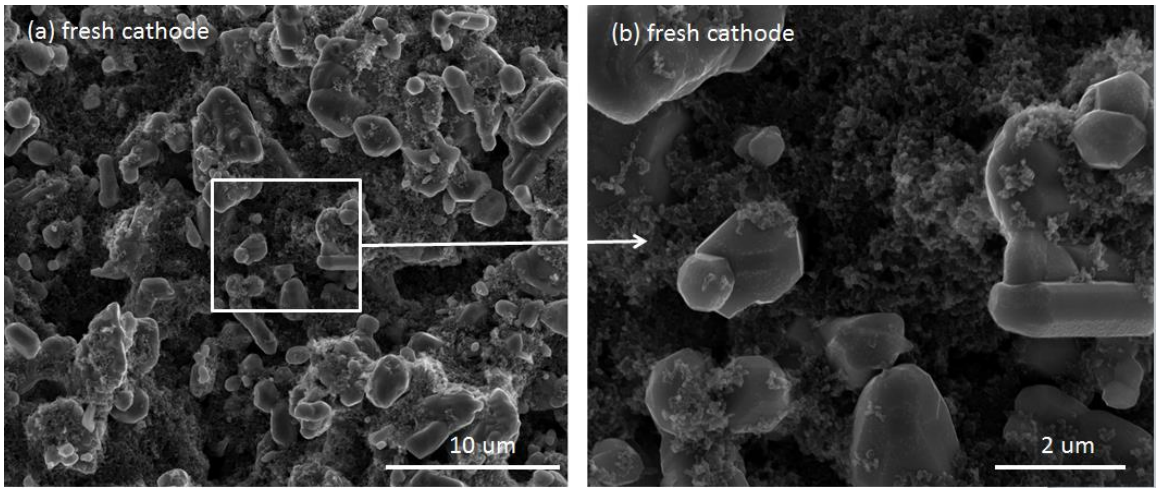

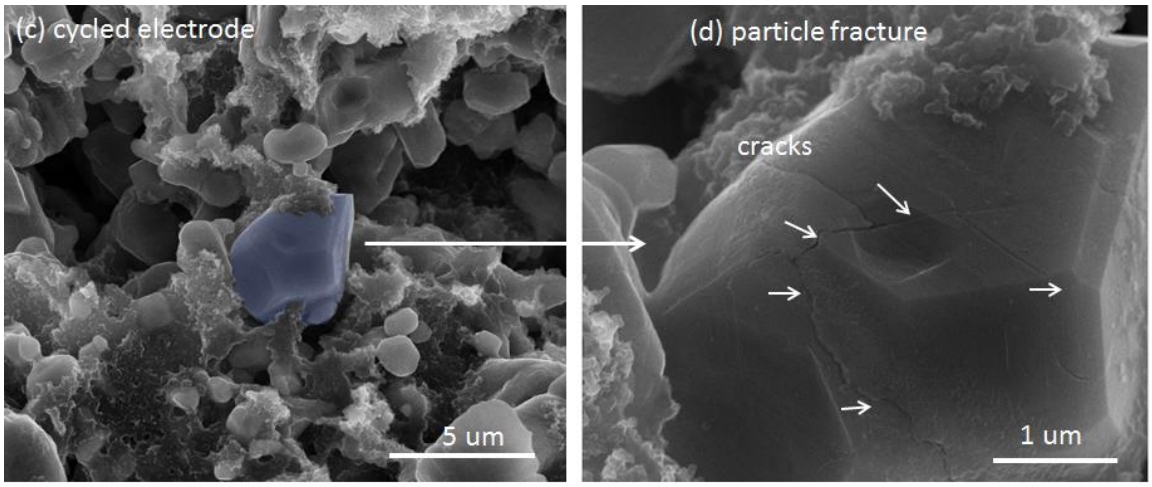

Figure 6.1 SEM images of (a)/(b) fresh cathode electrode with clear particle surfaces and cycled cathode electrode (c)/(d) after 1200, fractures are observed all over the surface of the particles. (d) shows that a part of the LMO material is surrounded by fractures and almost isolated from the bulk particle. The composite electrode consists of 5% carbon blacks and 5% PVDF and 90% LMO material from Sigma-Aldrich.

Fracture has a significant impact on cathode electrode performance. Fracture increases the surface area exposed to the electrolyte, therefore increasing the side reaction rate and Mn^{2+} dissolution[41]. The increased surface area might be beneficial for the lithium intercalation/deintercalation due to increased contact area with the electrolyte. However, fracture also leads to the loss of electrical contact and causes particle isolation, which contributes to capacity fade of the cathode electrode. In order to understand the impact of fracture on battery performance, our present work develops a single-particle fracture model which includes both diffusion and migration of lithium ions and electrons in the LMO particle. This model is used to investigate capacity fade due to fracture under different conditions.

The following sections introduce details of the modeling work as well as simulation experiments. The impact of LMO material conductivity, cathode SOC swing window, and particle size on cathode capacity performance will be investigated. As a result, the optimal design and operation rules are obtained to suppress the impact of fracture on cathode capacity fade.

6.2 Model Development

6.2.1 Cathode electrode composition and micro-structure

The fresh LMO cathode is made by mixing 5% carbon black, 90% LMO active material and 5% PVDF binder together. As shown in the Figure 6.1 (a), (b) and Figure 6.2 (a), carbon blacks are not distributed evenly on the surface of each particle. Instead a considerable portion of carbon blacks aggregate in between LMO particles and form the conductive network. Only a fraction of carbon blacks is in contact with LMO particles. The LMO particle surface is not fully covered by carbon blacks, and part of the surface area is exposed to the electrolyte. The carbon blacks connected to the LMO particles are the bridges for electron transport between the current collector and LMO particles. The LMO surface area exposed to the electrolyte is available for lithium ion intercalation /deintercalation. Figure 6.2 (b) shows the roles of carbon blacks and LMO particle and also the electron pathways in the cathode electrodes. The composition and the micro-structure of the LMO electrode can be simplified and represented by Figure 6.2 (d).

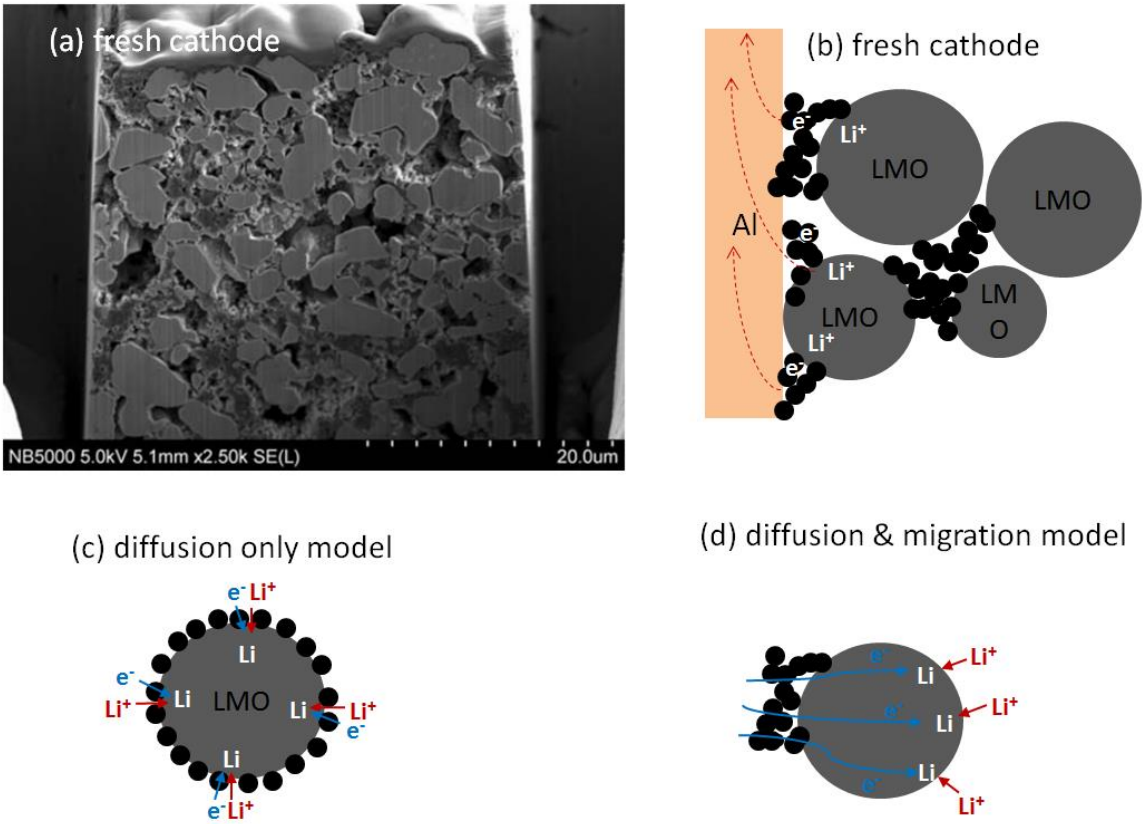

Figure 6.2 FIB-SEM micrograph of (a) a lithium manganese oxide composite electrode.[136] Due to carbon black aggregation, only a fraction of carbon blacks are in contact with the LMO particle (b). Diffusion only model (c) assumes that the carbon blacks are distributed over the particle surface uniformly, and therefore, the electrons and lithium ions react uniformly over the surface, only diffusion law governs the lithium transportation inside the particle. Diffusion & migration model (d) assumes that carbon blacks are not distributed evenly on the surface, and the mass transportation of lithium ions and electrons is controlled by both migration and diffusion.

In the conventional model [27], the lithium transportation in the particles is modeled by only diffusion lay as shown in Figure 6.2 (c). Diffusion only model assumes that the carbon blacks are distributed over the particle surface uniformly, and therefore, the electrons and lithium ions react uniformly over the surface, only diffusion law governs the lithium transportation inside the particle. The diffusion only model has a uniform flux over the particle surface. Therefore, bigger particle surface facilitates the lithium ion and electron reaction, and increases the lithium diffusion. Particle fracture increases the particle surface area, therefore is beneficial for batter performance in the diffusion only model, which is contradictory to the experimental

observations[42]. The electrical isolation cannot be captured in the diffusion only model. In the new proposed diffusion and migration model as shown in Figure 6.2 (d), it's assumed that carbon blacks are not distributed evenly on the surface, and the mass transportation of lithium ions and electrons is controlled by both migration and diffusion. Therefore, the fracture induced electrical isolation or electrical resistance increase can be captured and the impact of fracture on the battery capacity can be investigated.

As shown in Figure 6.2 (d), when the $LiMn_2O_4$/Li half-cell is being charged, the electrons are transferred out from the cathode. The carbon black network provides the pathway for electron transportation. Once the electrons from the LMO particles are out, due to the charge neutrality, the lithium ions are deintercalated out of the particles as well. When the cell is being discharged, the electrons are injected into the current collector from the external circuit and transferred to the LMO particles through the carbon black network. The lithium ions in the electrolyte are also intercalated into particles due to charge conservation.

After cycling, fracture develops as shown in Figure 6.1 (c) and (d). The fractured particles often have parts which are surrounded by fractures and almost isolated from the bulk particles as shown in Figure 6.1 (d). Based on experimental observations, the cathode micro-structure can be simplified and represented by a single-particle half-cell as shown in Figure 6.3.

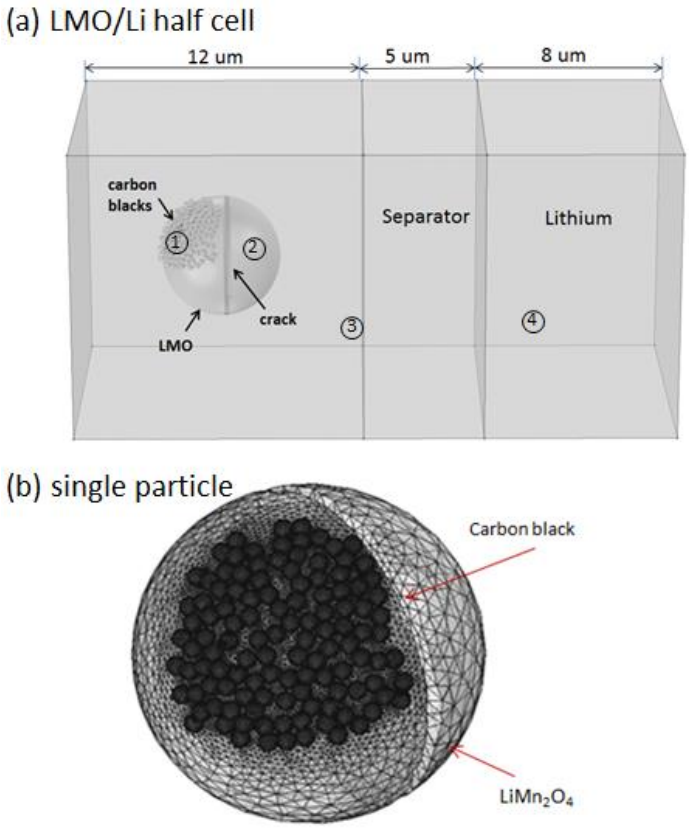

Figure 6.3 (a) LMO/Li half-cell includes carbon blacks (domain1), LMO particle (domain2), electrolyte and separator (domain3), and lithium metal anode (domain4). (b) Meshed geometry of the single LMO particle with carbon blacks. The carbon blacks are in contact with one side of the LMO surface.

The single-particle model is constructed in COMSOL as shown in Figure 6.3 (a). The model consists of 4 domains, carbon blacks (domain1), LMO particle (domain2), electrolyte and separator (domain3), and lithium metal anode (domain4). In all sections, subscripts 1, 2, 3, 4 denote the domains. Subscripts (1,2), (2,3), (3,4) denote the interfaces between carbon blacks and LMO particle, LMO particle and electrolyte, electrolyte and Li metal anode, respectively.

When the cell is being charged, the current flux is added to the carbon black surface, the electrons are transferred out of the LMO particle through the carbon black network, and lithium ions are deintercalated into the electrolyte. Lithium ions in the electrolyte are transferred to the anode side and deposited on the surface of lithium metal.

Due to the uneven distribution of carbon blacks in the cathode electrode, the carbon blacks are positioned mainly on one side of the LMO particle. Figure 6.3 (b) shows that the carbon blacks are positioned mainly on one side of the particle surface via Matlab random function.

The mass ratio between carbon black and LMO particle is 5%:90%. Due to the van der Waals force, electrostatic force, and Brownian force, LMO particles and carbon blacks dispersed in the liquid phase during electrode fabrication stick to each other, and spontaneously form irregular particle aggregates. Due to carbon black aggregation, carbon blacks are not distributed evenly on the LMO particle surface, instead, they form aggregates in between LMO particles. Therefore, only a fraction of the carbon blacks are in contact with the surface of LMO particles. Here we assume that about 40% of carbon blacks are attached to the surface. Therefore, the mass ratio between LMO particle and carbon blacks is 90:2.

6.2.2 Single-particle model equations

Due to the high conductivity of the carbon blacks, the only mobile species in them is electrons. Therefore, the flux of electrons in the carbon black network is governed by Ohm's law as expressed in the following equation:

$$E_1 = -\nabla \phi_1 \tag{6.1}$$

$$J_1 = \sigma_1 E_1 \tag{6.2}$$

where ϕ_1 is the electric potential of the carbon blacks. E_1 is the electric field, J_1 is the current density, i.e., the negative flux of the electrons, and σ_1 is the conductivity of the carbon black network.

The inlet/outlet flux only occurs on the interface of the LMO particle and carbon blacks, and also the interface between the LMO particle and the electrolyte. The interfaces between carbon

blacks and the electrolyte, between the LMO particle and the electrolyte, and between the electrolyte and lithium metal are electrically insulated.

Lithium ions are exchanged with the available electrons on the surface of the LMO particle. No electron flux occurs between the LMO particle and electrolyte. The electrochemical reaction at the LMO/electrolyte interface can be expressed in the following equation:

$$Li^+ + Mn_2O_4 + e^- \leftrightarrow LiMn_2O_4 \tag{6.3}$$

On the interface of carbon blacks and LMO particles, the electron flux is governed not only by electron concentrations in the LMO particle, but also the local potential difference between the carbon blacks and LMO particle. Butler volmer equation is used to model the electron flux as expressed in the following equation:

$$j_{1,2} = i_{1,2}\left\{\exp\left[\frac{\alpha_a F}{RT}\eta_{1,2}\right] - \exp\left[-\frac{\alpha_c F}{RT}\eta_{1,2}\right]\right\} \tag{6.4}$$

$$\eta_{1,2} = \phi_1 - \phi_2 - \mu \cdot U \tag{6.5}$$

where $j_{1,2}$ is the reaction current between carbon blacks and LMO, $i_{1,2}$ is the exchange current density, α_a is the anodic charge transfer coefficient, α_c is the cathodic charge transfer coefficient, U is the open-circuit potential, $\phi_2$is the LMO particle potential, and ϕ_1 is the carbon blacks potential, μ is the fraction coefficient.

On the interface of LMO particles and electrolyte, the Lithium intercalation/deintercalation rate is governed not only by lithium ion concentrations in both the electrolyte and LMO particle, but also the local potential difference between the electrolyte and LMO particle. Butler volmer equation is used to model the lithium intercalation/deintercalation rate as expressed in the following equation:

$$j_{2,3} = i_{2,3}\left\{\exp\left[\frac{\alpha_a F}{RT}\eta_{2,3}\right] - \exp\left[-\frac{\alpha_c F}{RT}\eta_{2,3}\right]\right\} \tag{6.6}$$

$$\eta_{2,3} = \phi_2 - \phi_3 - (1-\mu)\cdot U \tag{6.7}$$

where $j_{2,3}$ is the reaction current between LMO and electrolyte, $i_{2,3}$ is the exchange current density, α_a is the anodic charge transfer coefficient, α_c is the cathodic charge transfer coefficient, U is the open-circuit potential, ϕ_2 is the LMO particle potential, and ϕ_3 is the electrolyte potential.

In the LMO particle, the mobile species are lithium ions and electrons. The Mn_2O_4 host structure is relatively stationary. Yamamura *et al*. [137] conducted an in situ measurement of $LiMn_2O_4$ conductivity at different SOC. From their measurements, the conductivity vs. SOC curve is shown in Figure 6.4.

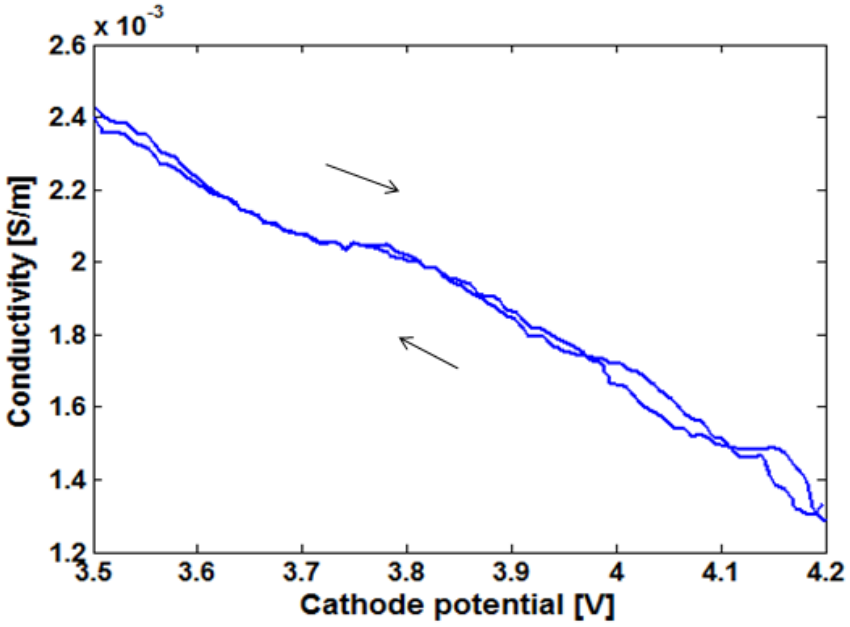

Figure 6.4 the potential-conductivity profile of a 0.2 um $LiMn_2O_4$ film[137]

Figure 6.4 shows that when the voltage is 4.2 V (x=0 in $Li_xMn_2O_4$), Mn_2O_4 still has a low conductivity, which indicates that there exist mobile electrons provided by Mn_2O_4. As the lithium ions intercalate into the LMO particle, the mobile electrons in the particle are increased. Therefore, based on charge neutrality, the total amount of mobile electrons is equal to the sum of

lithium ions and the certain amount of mobile electrons provided by the host structure (Mn_2O_4). The two sources of mobile electrons can be expressed in the following equations.

$$Li \leftrightarrow Li^+ + e^- \tag{6.8}$$

$$Mn_2O_4 \leftrightarrow (Mn_2O_4)^{x+} + xe^- \tag{6.9}$$

The fluxes of negatively and positively charged species in the cathode particle are governed by Nernst-planck equations, which are obtained by combining Ohm's law and diffusion equations to keep the charge conservation and mass conservation. The flux of each species is not only controlled by the concentration gradient but also the potential gradient as shown in the following equation.

$$J_{2,i} = -D_{2,i}\nabla c_{2,i} - z_{2,i}u_{m,i}Fc_{2,i}\nabla\phi_2 \tag{6.10}$$

$$k_{2,i} = {z_{2,i}}^2 u_{m,i}F^2 c_{2,i} \tag{6.11}$$

where $J_{2,i}$represents the flux of the mobile species i which can be e (electrons), Li (lithium ions), or Mn_2O_4 ($(Mn_2O_4)^{x+}$). $D_{2,i}$ is the diffusivity of species i. $c_{2,i}$ is the concentration, $z_{2,i}$ is the charge number, $u_{m,i}$ is the mobility, F is the Faraday constant, and ϕ_2 is the electric potential of the LMO particle. Because $(Mn_2O_4)^{x+}$ is stationary, it's assumed that the diffusion coefficient for $(Mn_2O_4)^{x+}$ is infinitely small; therefore, its flux is negligible. $k_{2,i}$ is the conductivity of the species i, which is a function of the concentration of species i .

The mobility of species i can be obtained from the Einstein relation expressed in the following equation.

$$u_{m,i} = \frac{D_{2,i}}{RT} \tag{6.12}$$

where $u_{m,i}$ is the mobility of the mobile species i, $D_{2,i}$ is the diffusity, R is the gas constant, and T is the absolute temperature. The mass conservation of each species is expressed as

$$\frac{\partial c_{2,i}}{\partial t} = -\nabla J_{2,i} = -\nabla(-D_{2,i}\nabla c_{2,i} - z_{2,i}u_{m,i}Fc_{2,i}\nabla\phi_2) \tag{6.13}$$

The charge conservation is expressed as

$$\sum_i z_{2,i}c_{2,i} = 0 \tag{6.14}$$

where $z_{2,i}$ is the charge number of species i.

The electrolyte ($LiPF_6$ 1M EC/DMC) is assumed to be binary, i.e., only positively charged lithium ions and negatively charged species are assumed to be mobile. The electro neutrality is satisfied by keeping the Li ions concentration always equal to the concentration of negatively charged species. Based on the concentrated solution theory[138], the fluxes of the positively charged ions and negatively charged ions can be expressed by the gradient of the electrochemical potential. The gradient of the electrochemical potential can be decomposed into gradients of the salt concentration and the electrical potential.[26] Therefore, the fluxes of the Li-ions and the negatively charged species can be expressed in the following equations. The detailed derivation is included in the Appendix. [139]

$$j_{3,+} = \left[-v_{3,+}D_3\frac{c_T}{c_0} + \frac{2k_3t_-^0t_+^0RT}{c_{3,+}z_{3,+}F^2}\right]\left(1 + \frac{d\ln f_{\pm}}{d\ln c_3}\right)\nabla c_{3,+} - \frac{k_3t_+^0}{z_{3,+}F}\nabla\phi_3 \tag{6.15}$$

$$j_{3,-} = \left[-v_{3,-}D_3\frac{c_T}{c_0} + \frac{2k_3t_-^0t_-^0RT}{c_{3,-}z_{3,-}F^2}\right]\left(1 + \frac{d\ln f_{\pm}}{d\ln c_3}\right)\nabla c_{3,-} - \frac{k_3t_-^0}{z_{3,-}F}\nabla\phi_3 \tag{6.16}$$

$$c_T = \sum_i c_{3,i} \tag{6.17}$$

$$\frac{c_{3,+}}{v_{3,+}} = \frac{c_{3,-}}{v_{3,-}} = c_3 \tag{6.18}$$

where $j_{3,+}$ and $j_{3,-}$ are the lithium ion flux and negatively charged ion flux in the electrolyte, $v_{3,+}$ and $v_{3,-}$ are the numbers of cations and anions into which a molecule of electrolyte

dissociates. D_3 and k_3 are the diffusivity and conductivity of electrolyte, c_T is the total concentration including the solvent, c_0 is the solvent concentrations. t_-^0 and t_+^0 are transference numbers. R is the gas constant, T is absolute temperature, $c_{3,+}$ and $c_{3,-}$ are the concentrations of lithium ions and negatively charged ions, $z_{3,+}$ and $z_{3,-}$ are charge numbers, F is the Faraday constant. $f_\pm$ is the electrolyte activity coefficient. c_3 is the electrolyte concentration. ϕ_3 is the electric potential of the electrolyte.

On the anode (lithium metal) surface, lithium deposition and dissolution occurs during charging and discharging. There is no electron exchange between electrolyte and lithium metal. The reaction rate of the lithium deposition or dissolution is controlled by the over potential between electrolyte and lithium metal and also lithium concentration in the electrolyte as expressed in the following equation.

$$j_{3,4} = i_{3,4}\left\{\exp\left[\frac{\alpha_{a,Li}F}{RT}\eta\right] - \exp\left[-\frac{\alpha_{c,Li}F}{RT}\eta\right]\right\} \tag{6.19}$$

$$\eta_{3,4} = \phi_4 - \phi_3 \tag{6.20}$$

where $j_{3,4}$ is the reaction current between electrolyte and lithium metal, $i_{3,4}$ is the exchange current density, $\alpha_{a,Li}$ is the anodic charge transfer coefficient, $\alpha_{c,Li}$ is the cathodic charge transfer coefficient, $\phi_4$is lithium metal potential, and ϕ_3 is the electrolyte potential.

Material properties were selected based on carbon blacks, $LiMn_2O_4$, EC/DMC 1M $LiPF_6$ electrolyte and Lithium metal. The values are listed in Table 6.1.

Table 6.1 Parameters for fracture model

TABLE I. Values of model parameters

Paramters	Description	Value	Ref.
σ_1(S/m)	Carbon black conductivity	100	[140]

$c_{2,Li}^{max}$(mol/m^3)	Maximum solid phase concentration	22860	[27]
k_0 (m/s)	Reaction rate coefficient	2×10^{-11}	[27]
α_a, α_c	Charge transfers coefficient	0.5	[27]
$k_{1,2}$ (m/s)	Reaction rate coefficient	7×10^{-8}	assumed
μ	Fraction coefficient	0.5	assumed
$i_{1,2}$	Exchange current density between carbon blacks and LMO	$Fk_{1,2}{c_2}^{0.5}$	assumed
$i_{2,3}$ (A/m^2)	Exchange current density between LMO and electrolyte	$Fk_0{c_3}^{\alpha_a}(c_{2,Li}^{max} - c_{2,Li})^{\alpha_a}{c_2}^{\alpha_c}$	[27]
U(V) [c]	Cathode electrode equilibrium potential	U($c_{2,Li}/c_{2,Li}^{max}$) curve	
$D_{2,Li}$(m^2/s)	Diffusivity of lithium ions	1×10^{-13}	[27]
$D_{2,e}$(m^2/s)	Diffusivity of electrons	1.5×10^{-14}	fitted
D_{2,Mn_2O_4}(m^2/s)	Diffusivity of $(Mn_2O_4)^{x+}$	1×10^{-900}	
$z_{2,Li}$	Charge number of lithium ion	1	
$z_{2,e}$	Charge number of electron	-1	
z_{2,Mn_2O_4}	Charge number of $(Mn_2O_4)^{x+}$	0.875	fitted
$v_{3,+}$	Number of cations per molecular of electrolyte	1	
$v_{3,-}$	Number of anions per molecular of electrolyte	1	
c_0(mol/m^3)	Solvent concentration	2.07×10^3	[141]
D_3(m^2/s)	Diffusivity of electrolyte	1.27×10^{-11}	[139]
k_3(S/m)	Conductivity of electrolyte	0.38	[142]
t_+^0	Li transference number	0.363	[27]
t_-^0	Anion transference number	$1 - t_+^0$	

$z_{3,+}$	Charge number of cations in electrolyte	1	
$z_{3,-}$	Charge number of anions in electrolyte	-1	
f_{-}^{+}	Electrolyte activity coefficient	1	
$i_{3,4}$(A/m^2)	Exchange current density between lithium foil and electrolyte	8500	[139]
$\alpha_{a,Li}$, $\alpha_{c,Li}$	Charge transfer coefficient	0.5	[139]
a_2(m^2)	Cross area	1.9635×10^{-11}	
L(m)	Distance between two terminals	5×10^{-6}	
F (C/mol)	Faraday constant	96485.3415	

[c] Curves in Appendix

6.3 Results

6.3.1 Validation of the single-particle model

In order to validate the model, a simulation experiment is conducted. Due to the difficulty of measuring the electronic conductivity of a sphere particle, a cylinder particle is constructed by using the same parameters and equations as used in the sphere particle. This simple geometry change makes the measurement much easier, and validates the same equations and same parameters. The simulation experiment setup is shown in Fig. 5 (a). During the electronic conductivity measurements, the electrons in the LMO cylinder are the only mobile species. The current flux (electron flux) is added to one terminal of the cylinder and flowing out of the cylinder from the other terminal. The conductivity is calculated by the following equation.

$$k_{2,e} = \frac{IL}{U_2 a_2} \tag{6.21}$$

where $k_{2,e}$ is the conductivity, I is the current, L is the distance between two terminals, U_2 is the voltage difference between two terminals, a_2 is cross area of the cylinder.

The electronic conductivity of the LMO material at different SOCs is measured from both simulation and experiments. Figure 6.5 (b) shows the comparison of measured [137] LMO conductivity and calculated value from simulation. The model has good prediction of LMO conductivity under different SOCs.

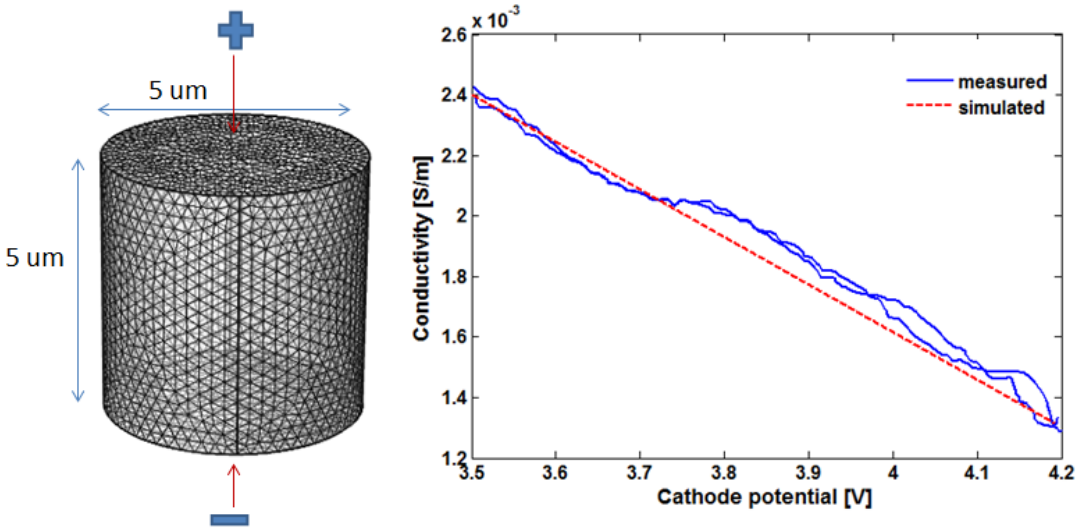

Figure 6.5 Simulation setup for measurements of conductivity and comparison between experimental measurements and calculated values from simulation.

Figure 6.5 shows that the conductivity of the LMO material is a function of Li ion concentration. As the lithium ion concentration increases, the conductivity increases as well. The maximum deviation between the simulated value and the measured data is about 6%.

Impact of the electronic conductivity

The electronic conductivity of LMO particles strongly affects lithium transportation in the particle. LMO material has a quite low conductivity [137]. In order to understand the impact of conductivity impact on the mass transportation pattern in the LMO particle, the model is charged

at 1C rate for 1000 seconds under different conductivities. Figure 6.6 (a) shows the lithium transportation in the LMO particle by using the measured conductivity data. Most of the lithium is deintercalated from the side where the carbon blacks connect to. As the conductivity increases by 10 times and 100 times shown in Figure 6.6 (b) and Figure 6.6 (c), more and more lithium is deintercalated out of the particle from elsewhere. After conductivity is increased by 1000 times as shown in Figure 6.6 (d), the lithium transportation pattern is much closer to the diffusion-only model. The lithium is deintercalated from each direction with the same flux. Figure 6.6 clearly shows that with high electronic conductivity, lithium intercalation/deintercalation initiates in each directions surrounding the particle. The fast transportation of electrons compensates for the lithium intercalation/deintercalation. With low electronic conductivity, the lithium intercalation/deintercalation initiates on the side close to the carbon blacks. The slow transportation of electrons cannot compensate for the lithium intercalation/deintercalation far away from the carbon blacks. Therefore, lithium intercalation/deintercalation mainly occurs on the side where electrons are available.

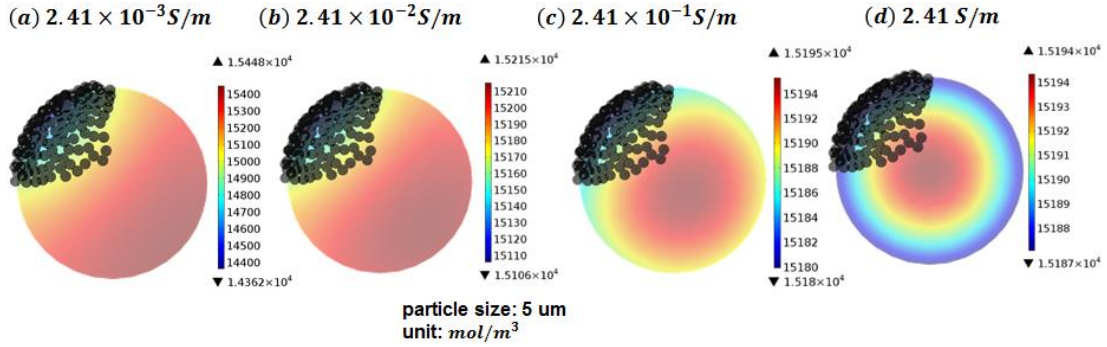

Figure 6.6 Li transportation in the LMO particle under different conductivities.

6.3.2 Fracture impact on lithium transportation

Fractures of LMO particles have been observed repeatedly [43] in the cycled electrodes as shown in Figure 6.1. On one hand, the fracture inevitably increases the surface area in contact with the electrolyte. The increased surface area is available for lithium intercalation/deintercalation. On the other hand, fracture increases the internal resistance for electron transportation inside the LMO particle. As shown in Figure 6.1 (c) and (d), the fractured particles are observed often to have some parts which are almost isolated from the bulk particle by fractures. In order to study the fracture impact on the lithium transportation in the particle, fracture is introduced to the particle, as shown in the Figure 6.7 (b). After fracture is added, the single particle is charged at 1C until the voltage increases to 4.4 V. Figure 6.7 (a) shows the lithium concentration profiles of LMO particle without fracture, and Figure 6.7 (b) shows the lithium concentration profile with fracture. For a particle without fracture, the lithium ions are mainly deintercalated on the side where carbon blacks connect to. The Lithium concentrations in the bulk are close to each other. The average concentration is about 6400 mol/m^3. After adding fracture, the concentrations in the bulk differ significantly. The concentration difference across the fracture is about 3899 mol/m^3. That means there is more lithium in the isolated region than the connected region. The fracture leads to the difficulty of lithium deintercalation in the isolated region. The total charge capacity with fracture decreases about 13.7% compared to the one without fracture.

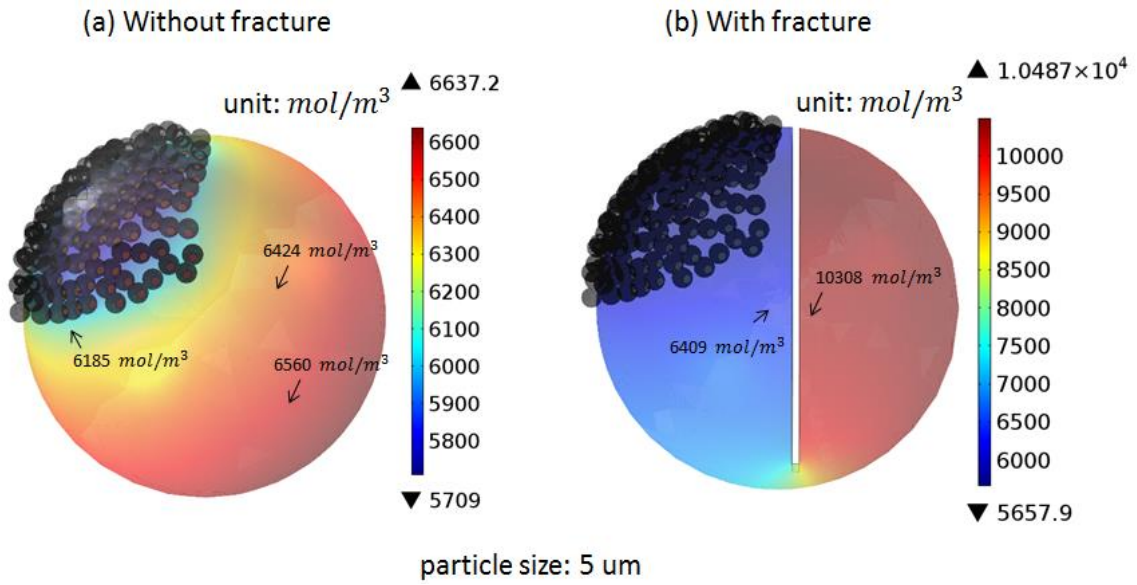

Figure 6.7 Lithium concentration profiles in the particles before and after adding fractures

6.3.3 Particle size impact

The impact of the particle size was also investigated. Three different particle sizes chosen are 1um, 5 um, and 8um. The mass ratio between carbon blacks and LMO particles are the same as before. In order to mesh the geometry, carbon blacks are scaled accordingly. All the particles are charged to 4.4 V. Figure 6.8 shows the lithium concentration profiles with different particle sizes.

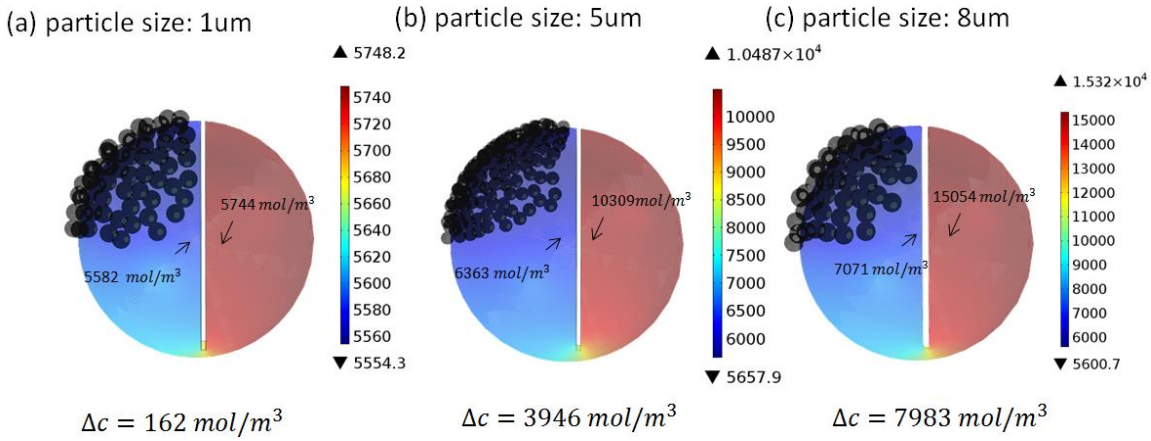

Figure 6.8 Lithium concentration profiles at different particle sizes

Figure 6.8 shows that the particle size has a significant impact on lithium transportation in the LMO particle with fractures. Smaller particles facilitate the transportation of lithium due to increased specific surface area and decreased internal resistance. The lithium concentration difference across the fracture decreases as particle size decreases. When particle size is 1um as shown in Figure 6.8 (a), the concentration difference across the fracture is only 162 mol/m3 which is quite small and negligible. However, after increasing the particle size to 5 um as shown in Figure 6.8 (b), the concentration difference becomes 3946 mol/m^3. When the particle size is increased to 8 um as shown in Figure 6.8 (c), the concentration difference further increases to 7983 mol/m^3 which is significant. From the above study, smaller particle size is preferable in order to suppress the impact of fracture.

6.3.4 SOC impact

SOC has a significant impact on the conductivity of the LMO material as shown in Figure 6.4. In order to understand the SOC impact on the lithium transportation with fracture, particles are charged at 1C rate to different SOCs; the lithium concentration profiles are shown in Figure 6.9.

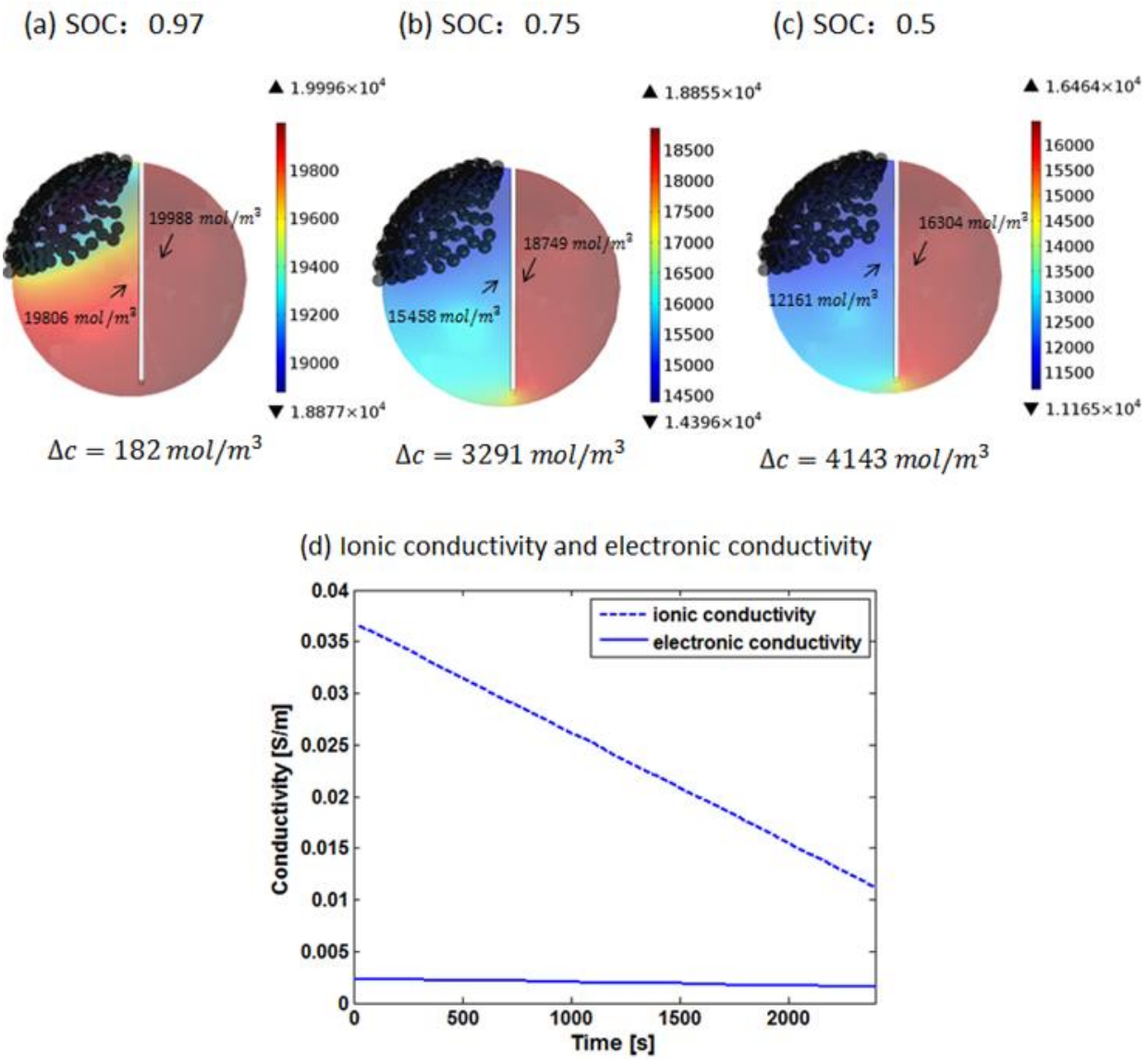

Figure 6.9 lithium concentration profiles at different particle sizes

Because the carbon blacks pull the electrons out of the LMO particle, most of the lithium is deintercalated from the side where carbon blacks connect to. However, as the lithium concentration goes down during charging, Eq. 9 demonstratesthat the ionic conductivity of lithium goes down as well. Lithium transportation becomes more difficult. The electronic conductivity also goes down. The comparison between ionic conductivity and electronic conductivity is shown in Figure 6.9 (e). It shows that electronic conductivity is lower than ionic conductivity. Therefore, the mass transportation inside the particle is mainly limited by electron

transportation. After the SOC goes down, both electronic conductivity and ionic conductivity decrease. In order to suppress the impact of fracture, higher SOC is preferable; higher SOC brings both high electronic conductivity and ionic conductivity, which facilitates mass transportation.

6.3.5 Conclusions

Based on the experimental observations, a single-particle model has been developed to study the impact of fracture on the capacity fade of Li-ion batteries. This study explores the impact of conductivity, the SOC swing window, and particle size on fracture-induced capacity fade.

It shows that electronic conductivity has a significant impact on the Li transportation in the LMO particle. When electronic conductivity is low, the main limiting factor is the electron transportation in the particle rather than lithium transportation. As electronic conductivity increases, the limiting factor changes from electron transportation to lithium transportation. When the electronic conductivity is high enough, lithium transportation can be assumed to be diffusion only. The low electronic conductivity indicates that the lithium is deintercalated on the side where carbon blacks connect to. When fracture is present, the resistance for electron transportation increases inside the particle. Therefore, some lithium is stuck in the isolated part due to lack of electrons. Based on the SOC investigation, SOC also has a significant impact on the conductivity of the LMO particle. When the SOC is high, the particle is full of lithium and electrons, and both electronic conductivity and ionic conductivity are relatively higher. Therefore, the electrons can be pulled out relatively easily. The SOC study suggests that the cathode should be run at a higher SOC level to gain the good conductivity required to suppress the impact of fracture on capacity fade. Particle size is another key factor that affects mass transportation in the particle. Larger particles lead to higher internal resistance for electron transportation; therefore,

fracture-induced capacity fade is more severe than with particles of smaller size. Therefore, in order to suppress the impact of fracture, a smaller particle size is preferable.

Nomenclature

a_2	cross area
$c_{2,Li}$	concentration of lithium
$c_{2,e}$	concentration of electrons
c_{2,Mn_2O_4}	Concentration of $(Mn_2O_4)^{x+}$
c_T	total concentration including the solvent
c_0	solvent concentrations
$c_{3,+}$	concentrations of lithium ions in electrolyte
$c_{3,-}$	concentrations of negatively charged ions in electrolyte
c_3	electrolyte concentration
$D_{2,Li}$	diffusivity of Lithium
$D_{2,e}$	diffusivity of electron
D_{2,Mn_2O_4}	diffusivity of $(Mn_2O_4)^{x+}$, which is infinitely small
D_3	diffusivity of electrolyte
E_1	electric field of carbon black network
f_-^+	electrolyte activity coefficient
F	Faraday constant
I	applied current for conductivity measurements
$i_{1,2}$	exchange current density between carbon blacks and LMO
$i_{2,3}$	exchange current density between LMO and electrolyte
$j_{3,+}$	lithium ion flux in the electrolyte
$j_{3,-}$	negatively charged ion flux in the electrolyte
$j_{3,4}$	reaction current between electrolyte and lithium metal
$i_{3,4}$	exchange current density between electrolyte and lithium metal
$j_{1,2}$	reaction current between carbon blacks and LMO
$j_{2,3}$	reaction current between LMO and electrolyte
$J_{2,Li}$	flux of lithium in LMO particle
$J_{2,e}$	flux of electron in LMO particle
J_{2,Mn_2O_4}	flux of $(Mn_2O_4)^{x+}$ in LMO particle, which is zero
$k_{2,e}$	electronic conductivity of LMO
k_3	conductivity of electrolyte
L	distance between two terminals
t_+^0	Li transference number
U	cathode electrode equilibrium potential
U_2	voltage difference between two terminals
$v_{3,+}$	number of cations per molecular of electrolyte
$v_{3,-}$	number of anions per molecular of electrolyte
$z_{2,Li}$	charge number of lithium ion

$z_{2,e}$	charge number of electron
z_{2,Mn_2O_4}	charge number of $(Mn_2O_4)^{x+}$
$z_{3,+}$	ccharge number of cations in electrolyte
$z_{3,-}$	charge number of anions in electrolyte
σ_1	conductivity of the carbon black network
$\eta_{1,2}$	over potential between carbon blacks and LMO
$\eta_{2,3}$	over potential between LMO and electrolyte
$\eta_{3,4}$	over potential between Li metal and electrolyte
ϕ_1	electric potential of the carbon blacks
ϕ_2	LMO particle potential
ϕ_3	electrolyte potential
ϕ_4	lithium metal potential

6.4 Summary

This chapter developed a single-particle model to study the impact of fracture on the capacity fade of cathode electrode. The study investigates the impact of conductivity, SOC swing window, and particle size on the fracture-induced capacity fade. The study suggests that the cathode should be run at a higher SOC level to gain the good conductivity required to suppress the impact of fracture on capacity fade. Particle size is another key factor that affects mass transportation in the particle. Larger particles lead to higher internal resistance for electron transportation; therefore, fracture-induced capacity fade is more severe than with particles of smaller size. Therefore, in order to suppress the impact of fracture, a smaller particle size is preferable. This chapter provides design guidance to the cathode electrode.

Chapter 7
Battery Health Improvement through Multi-objective Optimization

7.1 Introduction

Battery longevity is crucial in transportation electrification[143, 144]. While a 3 to 5 years battery life is acceptable for consumer electronics, such as, cell phones, laptops, etc., such short service time would pose a major drawback for a hybrid/electric vehicle[145, 146]. Battery pack replacement would constitute an expense comparable to an engine or transmission. However, batteries are non-ideal energy storage system, minimizing the energy consumption of a battery – powered system is not equivalent to maximizing the battery lifetime[147]. Several studies have been done to optimize the battery performance, especially the energy density and power density. Fuller *et al*. [148] investigated the dual lithium ion insertion cell and optimized the energy density and power density by using Newman's battery model. Sumitava *et al*. [149] developed a model-based procedure to optimize the battery parameters, such as, electrode porosities and thickness to maximize the energy draw for an applied current, cutoff voltage, and total amount of discharge time. Some research efforts have been devoted to improving the battery lifetime. Advanced control algorithms have been developed to improve the battery lifetime. Moura *et al*.[150-152] developed a battery management strategy based on SEI growth model to protect the battery health during charging and discharging. Advanced control algorithm can maximize the performance under certain hardware settings, however, the best achieve performance is limited by the battery parameters. Therefore, before developing advanced management algorithms, battery parameters should be first optimized to reduce the potential degradations. All the above research work is focused on control algorithms or energy density and power density optimization.

No direct relationship between battery parameters and capacity fade has yet been established. In this chapter, the impact of design parameters on the battery capacity fade will be investigated, and optimal design guidance will be developed.

7.2 Degradation analysis and potential improvement

As discussed in previous chapters, the capacity fade can be explained in total cyclable lithium loss and individual electrode capacity loss.

7.2.1 Side reactions on anode

From 1.2.4 and 5.3.3, the cyclable lithium loss is mainly due to the side reactions on the anode surface, especially, the SEI growth. Figure 7.1 summarizes the degradation mechanisms on the anode surface, which lead to the total cyclable lithium loss. SEI growth is the major contributor to the cyclable lithium loss. The lithium which is supposed to intercalate into the graphite, reacts with solvent and forms SEI products. The deposition of Mn particles on the lithium metal after cycling was confirmed through EDX analysis [41, 99]. Mn deposition also costs additional cyclabe lithium loss. The electrons that are supposed to couple with lithium ions in the electrolyte are consumed by Mn^{2+} ions, therefore, the lithium ions are left in electrolyte inactively. Li plating leads to a huge amount of cyclable lithium loss, because the lithium deposited on the surface will react fast with solvent to form SEI products. The details of the roles of each side reactions on the graphite surface have been discussed in Chapter 5. In order to reduce side reactions on the graphite surface, different design parameters are investigated by using the degradation model developed in previous sections.

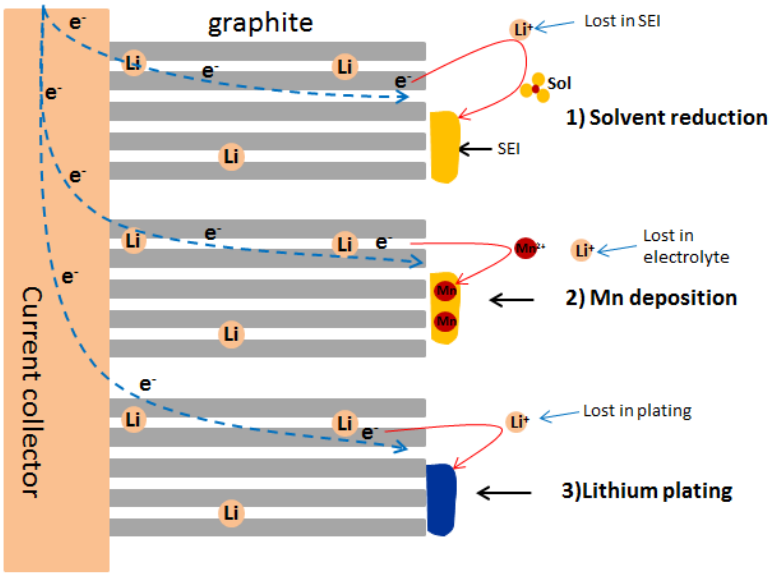

Figure 7.1 Cyclable lithium loss due to side reactions on the graphite surface

7.2.2 Side reactions on cathode

From the study in Chapter 5, cathode electrode capacity fade is one main contributor to the cell capacity fade. The fracture induced by stress inside the cathode particle could lead to particle isolation, and therefore capacity fade. Figure 7.2 shows the SEM images of fractures and Mn dissolution at the same scale. These figures show clearly that compared to fracture, Mn dissolution is less likely to cost significant capacity fade.

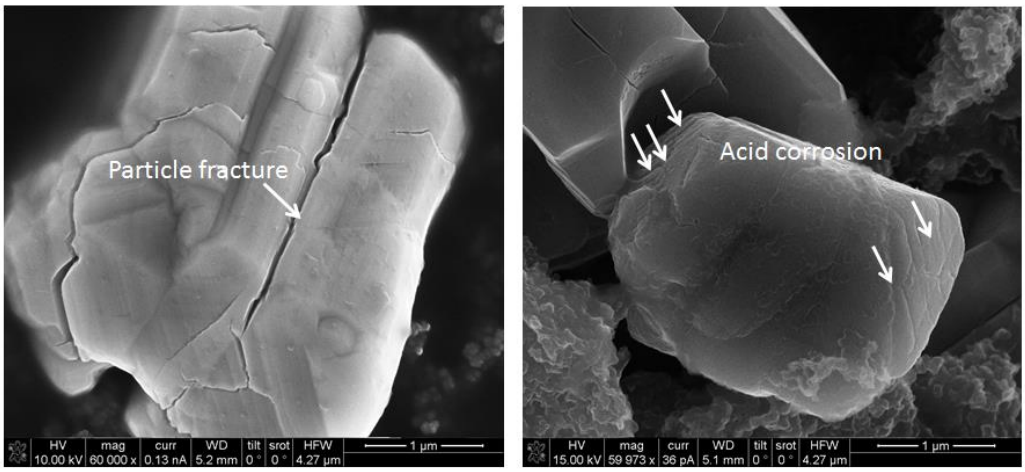

Figure 7.2 Comparison between fracture and Mn dissolution

The details of the roles of fracture and Mn dissolution in the cathode capacity fade have been discussed in Chapter 5. In order to reduce side reactions, mainly the fracture, on the cathode particle, different design parameters are investigated by using the degradation model developed in previous sections.

In order to improve the cycle life, side reactions on both anode and cathode should be reduced. In the following section, advanced optimization algorithm is utilized to improve the battery health.

7.3 Multiple-objective optimization

The design parameters have significant impact on the battery performance. In several research works[149, 153-157], battery design parameters are optimized to achieve better battery performance, such as, high energy density and power density. In this dissertation, several main design parameters are investigated in order to achieve better battery cycle life. In this Chapter, the design parameters are optimized to meet the power density and energy density requirements first, and then the cycle life is optimized.

Design parameters for a typical Lithium ion battery are chosen from reference [27] as shown in Table 4.2. Parameters of material properties are determined by the nature of the material and the synthesis methods, in this Chapter, the values for material properties are known from reference and fixed. Based on the material properties, the impact of cell fabrication parameters, such as, anode and cathode particle sizes, electrode thickness, electrode porosity, and mass ratio, are investigated.

7.3.1 Optimization framework

A general optimization problem has the following form:

$$\text{minimize} \qquad f(x),\ f: \mathbb{R}^n \to \mathbb{R} \tag{7.1}$$

$$\text{subject to} \qquad \begin{cases} x_{lower} \le x \le x_{upper} \\ g_i(x) \le 0,\ i = 1, \dots, m \\ h_i(x) = 0,\ \ i = 1, \dots, p \end{cases} \tag{7.2}$$

Where $f(x)$ is the objective function to be minimized over the variable x, $g_i(x)$ are called inequality constraints, and $h_i(x)$ are called equality constraints. In this case, the objective function is the battery capacity fade after long time cycling. The variables are the design variables listed in Table 7.1.

A gradient-descent scheme [158] is employed in this framework due to its efficiency and ability to handle nonlinear problems. The process of gradient calculation and variable optimization is shown in Figure 7.3.

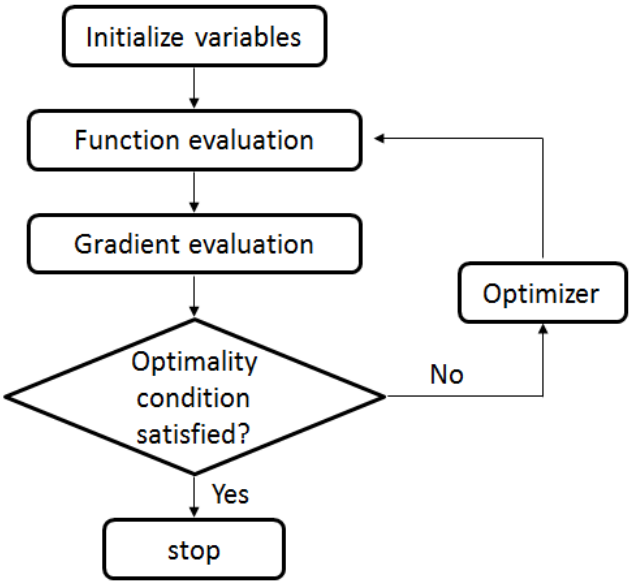

Figure 7.3 Flowchart of a gradient based optimization scheme

The first order necessary conditions for a solution in nonlinear programming to be minimal is the Karush-Kuhn-Tucker (KKT) conditions[159], which is expressed as below.

$$\nabla f(x^*) - \sum_{i=1}^{m} \mu_i \nabla g_i(x^*) - \sum_{i=1}^{p} \lambda_i \nabla h_i(x^*) = 0 \tag{7.3}$$

$$\mu_i \geq 0, \qquad \text{for all} \quad i = 1, \dots, m \tag{7.4}$$

$$\mu_i g_i(x) = 0, \quad \text{for all} \quad i = 1, \dots, m \tag{7.5}$$

Where μ and λ are the Lagrange multipliers associated with the inequality and equality constraints. Eq. (7.3) and Eq. (7.4) are used to differentiate between active and inactive inequality constraints, such that inactive constraints can be removed from consideration by equating them to zero. The numerical method used to solve the optimization problem is introduced in the following section.

7.3.2 Optimization method

In this dissertation, the gradient-based optimization method used is the sequential quadratic programming (SQP). SQP solves a sequence of optimization subproblems, each of which optimizes a quadratic model of the objective subject to a linearization of the constraints. The subproblem at each iteration can be expressed by.

$$\text{minimize} \quad \frac{1}{2} d^T H_k d + \nabla f(x_k)^T d \tag{7.6}$$

$$\nabla g_i(x_k)^T d + g_i(x_k) \leq 0, \qquad \text{for all} \quad i = 1, \dots, m \tag{7.7}$$

$$\nabla h_i(x_k)^T d + h_i(x_k) = 0, \qquad \text{for all} \quad i = 1, \dots, p \tag{7.8}$$

The matrix H_k is a positive definite approximation of the Hessian matrix of the Lagrangian function. H_k can be updated by any of the quasi-Newton methods. This subproblem can be solved using QP algorithm. The solution is used to form a new iterate at

$$x_{k+1} = x_k + \alpha_k d_k \tag{7.9}$$

The step length parameter α_k is determined by an appropriate line search procedure so that a sufficient decrease in a merit function is obtained.

7.3.3 Problem Setup

In order to satisfy automobile performance, energy density and power density are first optimized. The power density requirement is chosen first and fixed as a constraint. The energy density is maximized by using the numerical optimization framework in previous section. The battery parameters obtained after maximizing energy density with power density requirement are used as the starting point of battery health optimization. In the battery health optimization, the power density requirement is still fixed, and the energy density requirement is lowered down to a fraction of the maximum energy density in order to let optimization algorithm have some freedom to search for better parameters to improve health.

In the first step, the energy density is obtained through one galvanostatic discharge cycle of the cell until a cutoff voltage of 3.5V for 3600s, which is a common cutoff voltage for Li-ion cell. The power density is obtained through high discharge rate to cutoff voltage of 3V for 10 s[160]. This cutoff value is selected as further discharge of cell in real life could lead to irreversible damage to the battery. The capacity fade is represented by the relative difference between discharge capacity at the 100th cycles and the discharge capacity at the 1st cycle.

$$E_{cell} = \frac{1}{M_{cell}} \int_0^{3600} V_{cell}(t) I dt \tag{7.10}$$

$$P_{cell} = \frac{1}{M_{cell}} \int_0^{10} V_{cell}(t) I dt \tag{7.11}$$

$$f_{degra} = \frac{C_{100} - C_1}{C_1} \tag{7.12}$$

$$M_{cell} = M_{cc-} + M_{-} + M_{sep} + M_{+} + M_{cc+} \tag{7.13}$$

Where E_{cell} is the energy density, P_{cell} is the power density, V_{cell} is the cell terminal voltage, I is the discharge rate, f_{degra} is the relative capacity fade, C_{100} is the discharge capacity at 100th cycle, C_1 is the discharge capacity at 1st cycle. M_{cell} is the total cell mass, M_{cc-} is the mass of the negative current collector, M_- is the mass of the negative electrode, M_{sep} is the mass of the separator, M_+ is the mass of the positive electrode, M_{cc+} is the mass of the positive current collector. The mass of electrodes is a function of thickness, and porosity.

$$\text{maximize} \qquad E_{cell} = \frac{1}{M_{cell}} \int_0^{3600} V_{cell}(t) I dt \tag{7.14}$$

$$\text{subject to} \qquad \begin{cases} x_{lower} \leq x \leq x_{upper} \\ g_1(x) = P_{req} - P_{cell} \leq 0 \end{cases} \tag{7.15}$$

To minimize the capacity fade, we selected 8 design parameters, as shown in Table 7.1. The cycling rate is an operation condition and not a cell design variable. It's necessary to allow it to vary during the constraint evaluation, in order to meet the energy and power density requirements. Except cycling rate, there are 7 design parameters. There are 3 design parameters for the anode, which are particle size, electrode thickness, and porosity. However, there are 4 design parameters for cathode, which includes particle size, electrode thickness, porosity, and conductivity. Because graphite electrode is highly conductivity, adding more carbon blacks doesn't affect the conductivity much; therefore, the conductivity of the anode is fixed at a high value. However, the conductivity of cathode electrode is highly dependent on the conductive additive, and can be varied significantly during fabrication.

$$E_{cell} = \frac{1}{M_{cell}} \int_0^{3600} V_{cell}(t) I dt \tag{7.16}$$

$$P_{cell} = \frac{1}{M_{cell}} \int_0^{10} V_{cell}(t) I dt \tag{7.17}$$

$$f_{degra} = \frac{C_{100} - C_1}{C_1} \tag{7.18}$$

$$M_{cell} = M_{cc-} + M_{-} + M_{sep} + M_{+} + M_{cc+} \tag{7.19}$$

The optimization problem is to minimize the capacity fade after long term cycling while meeting the energy density and power density requirements. The overall optimization problem can be expressed by the following equations.

$$\text{minimize} \qquad f_{degra}(x) = \frac{C(x)_{100} - C(x)_1}{C(x)_1} \tag{7.20}$$

$$\text{subject to} \qquad \begin{cases} x_{lower} \le x \le x_{upper} \\ g_1(x) = P_{req} - P_{cell} \le 0 \\ g_2(x) = E_{req} - E_{cell} \le 0 \end{cases} \tag{7.21}$$

Where P_{req} is the power density requirement, E_{req} is the energy density requirement.

Table 7.1 Design variables and their bounds

Design variables	Lower bound	Upper bound
Cathode particle radius (um)	0.2	20
Cathode thickness (um)	40	250
Cathode porosity	0.1	0.6
Cathode conductivity (S/m)	1	10
Anode particle radius (um)	0.2	20
Anode thickness (um)	40	250
Anode porosity	0.1	0.6
Cycling rate (C)	0.1	20

In order to achieve global minimal, different starting points are chosen as shown in Table 7.2. In each set of initial parameters, the value of each parameter is chosen randomly and also different from other sets of parameters. These four sets of initial parameters are used as initial values for each energy and power optimization.

Table 7.2 Initial values for four different starting points

Parameters	1 set	2 set	3 set	4 set
Cathode particle radius (m)	$\mathbf{4 \times 10^{-6}}$	$\mathbf{3 \times 10^{-6}}$	$\mathbf{3.5 \times 10^{-6}}$	$\mathbf{3 \times 10^{-6}}$
Cathode thickness (m)	$\mathbf{80 \times 10^{-6}}$	$\mathbf{60 \times 10^{-6}}$	$\mathbf{90 \times 10^{-6}}$	$\mathbf{50 \times 10^{-6}}$
Cathode porosity	0.35	0.45	0.4	0.35
Cathode conductivity (S/m)	3	2	1	1
Anode particle radius (m)	$\mathbf{6 \times 10^{-6}}$	$\mathbf{7 \times 10^{-6}}$	$\mathbf{5 \times 10^{-6}}$	$\mathbf{12 \times 10^{-6}}$
Anode thickness (m)	$\mathbf{52 \times 10^{-6}}$	$\mathbf{47 \times 10^{-6}}$	$\mathbf{66 \times 10^{-6}}$	$\mathbf{55 \times 10^{-6}}$
Anode porosity	0.3	0.47	0.3	0.55
Mass ratio	2.1726	1.9788	1.6794	2.4383

The battery parameters except the design variables are listed in the following table. These parameters are listed in Table 4.2 and fixed in each optimization.

7.4 Results and discussion

The power density requirement varies from different application. In this study it is chosen to be $2200\ \mathrm{W/kg}$ which is in the range of the reported values [161, 162]. Due to the high complexity of the degradation model, each derivative evaluation takes about half hour. After 15 days' continuously running, the optimized values are found and listed in Table 7.3. For each set of initial parameters, the optimization is conducted.

As shown in Figure 7.4, for each set of initial parameters, the optimization algorithm maximized the energy density, and meanwhile adjusts the parameters to meet the power requirement. All power densities from four different starting points reach the power density

requirement 2200 W/kg after optimization. Energy densities are increased as much as possible to nearly 100 Wh/kg.

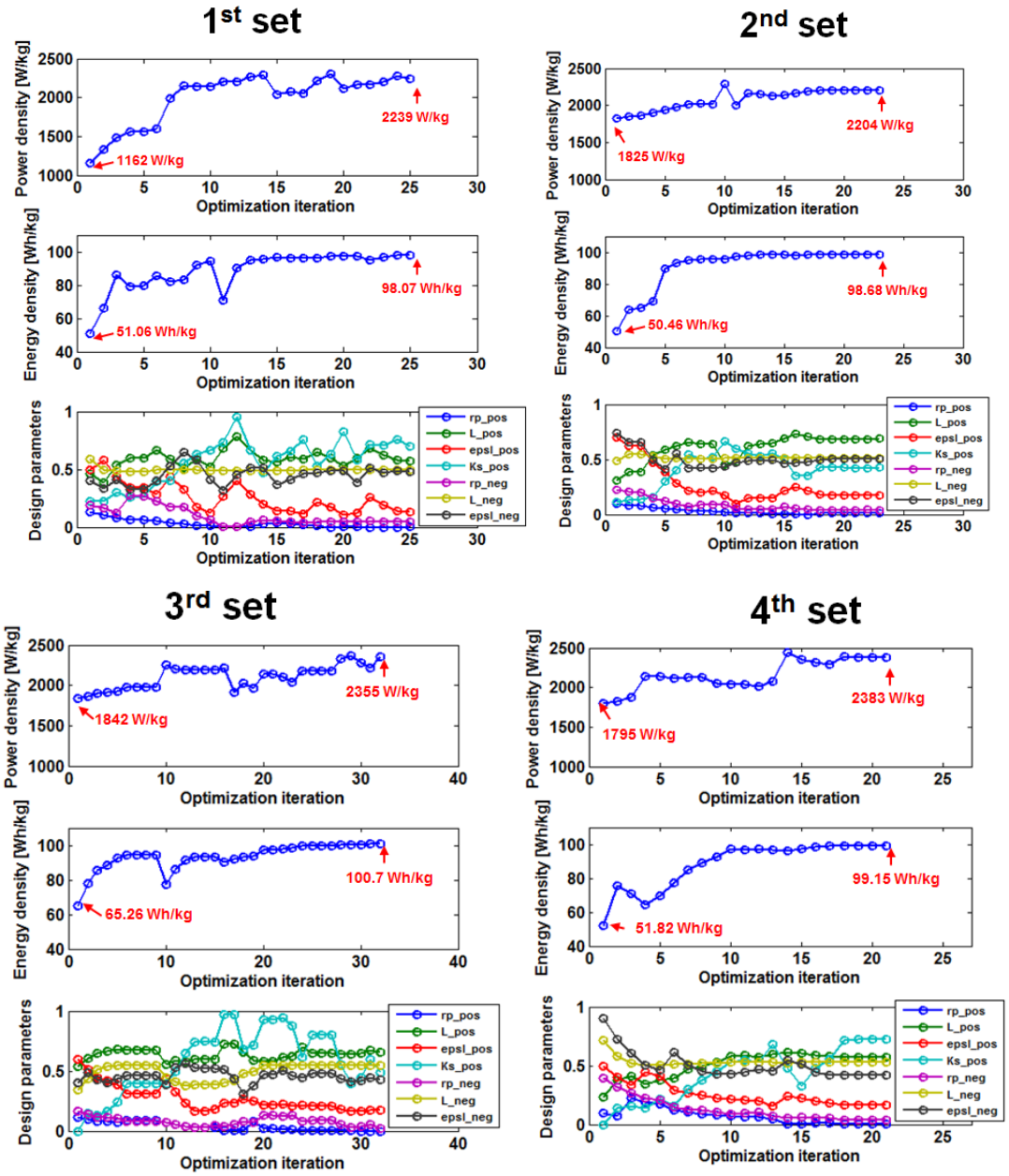

Figure 7.4 Energy optimization with power density requirement

The optimized parameters in Table 7.3 are close to each other, and the average values are calculated. These average values are used as the starting point for the battery health optimization.

Table 7.3 Optimized parameter value for energy and power

Parameters	Symbol	1 set	2 set	3 set	4 set	average
Cathode particle radius	rp_pos [um]	0.45	0.51	0.21	0.38	0.39
Cathode thickness	L_pos [um]	94.26	109.36	103.35	94.39	100.34
Cathode porosity	Epsl_pos	0.17	0.19	0.19	0.18	0.18
Cathode conductivity	Ks_pos [S/m]	7.28	4.85	6.02	7.53	6.42
Anode particle radius	rp_neg [um]	1.57	1.39	1.74	1.31	1.50
Anode thickness	L_neg [um]	106.31	119.74	101.86	94.25	105.26
Anode porosity	epsl_neg	0.34	0.35	0.32	0.31	0.33
Mass ratio	mass_ratio	2.00	2.03	2.09	2.06	2.04

From the optimization of energy density and power density, it shows that the design parameters are converging to the optimal values. The energy density reaches about 100 Wh/kg which is the maximum achievable density under power requirement and material parameters. In order to allow optimization algorithm to have freedom to adjust design parameters, energy density requirement is cut to certain level of the maximum achievable. In this study, 86% of the maximum value is chosen, i.e. 86 Wh/kg. The parameter values from energy and power optimization are used as starting point for battery health optimization. Energy density and power density requirements are used as constraints for battery health optimization. Figure 7.5 shows the optimization process. Battery degradation is decreased from 60% to 20% at 100 cycles after optimization. The design parameters all converged to the optimal values.

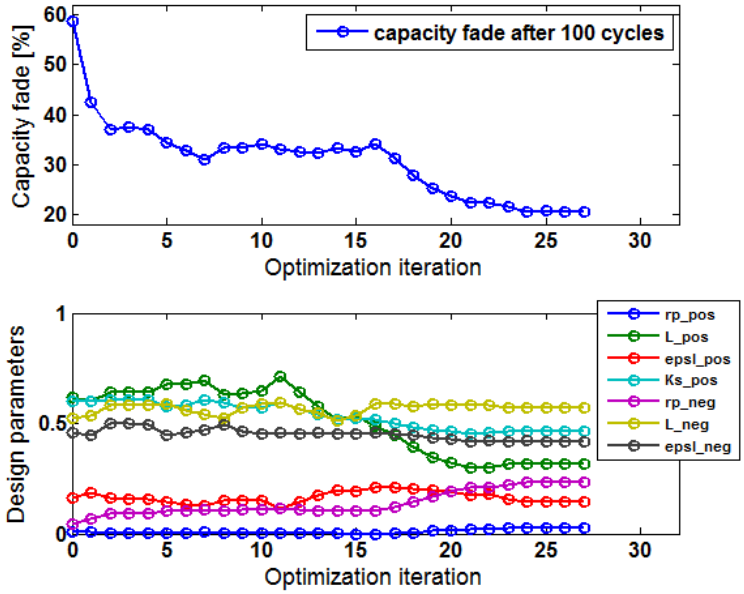

Figure 7.5 Battery health optimization

The design parameters are compared before and after optimization, which are listed in Table 7.4. From the comparison, it shows the most significant changes are the particle sizes change of anode particle and cathode particle.

Table 7.4 Optimized parameter values for battery health

Parameters	Symbol	average	optimized for health
Cathode particle radius	*rp_pos [um]*	*0.39*	*0.95*
Cathode thickness	*L_pos [um]*	*100.34*	*61.12*
Cathode porosity	*Epsl_pos*	*0.18*	*0.17*
Cathode conductivity	*Ks_pos [S/m]*	*6.42*	*5.18*
Anode particle radius	*rp_neg [um]*	*1.50*	*7.08*
Anode thickness	*L_neg [um]*	*105.26*	*60.00*
Anode porosity	*epsl_neg*	*0.33*	*0.31*
Mass ratio	*mass_ratio*	*2.04*	*2.14*
	degradation	*60%*	*20%*

7.4.1 Comparison before and after optimization

The cell performance before and after optimization are compared by using the parameters in Table 7.4. Before optimization, the capacity fade is shown in Figure 7.6, the capacity fade is about 40% after 100 cycles, which is severe. However, after optimization, the cell capacity decreases about 20 %, which is about half degradation before optimization. The energy density is reduced to about 86 Wh/kg to achieve better battery health.

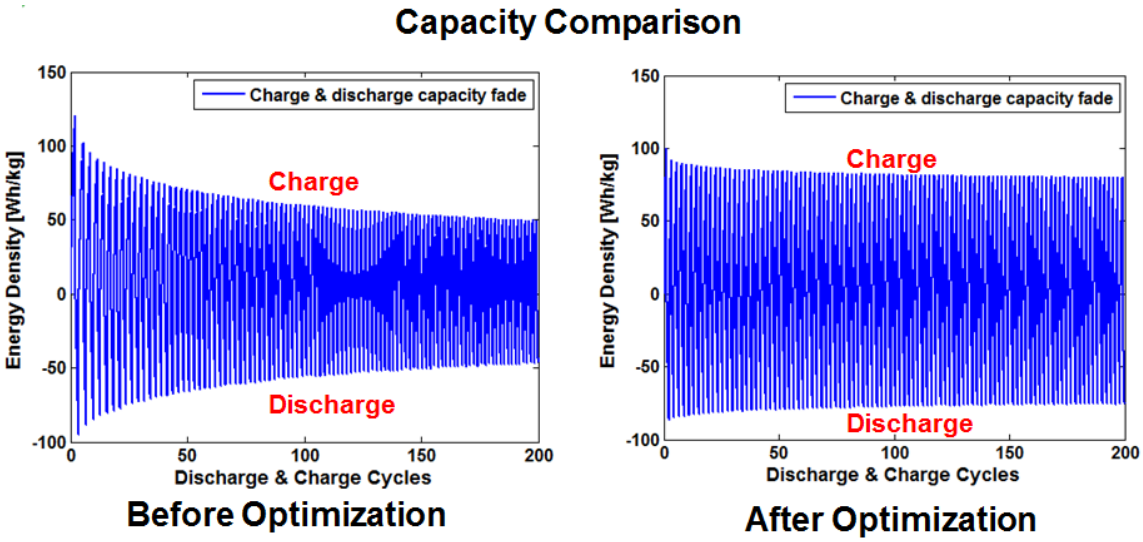

Figure 7.6 Capacity degradation comparison between normal cell and optimized cell

In order to understand the degradation pattern in the above two cases, the SOC windows are analyzed. As shown in Figure 7.7, the anode and cathode swing windows have been optimized. The degradation of the cell before health optimization has a shrinking cathode SOC window, and a shrinking anode SOC window. The main reason is due to the anode SEI growth which consumes the cyclable lithium. Before the health optimization, the anode particle size is quite small due to high power and energy requirement. Small anode particle size provides a high total surface area which accelerates the SEI growth, therefore leads to consumption of cyclable lithium. After optimization, the anode particle size is increases significantly as shown in Table

7.4. The SEI growth is suppressed, and therefore the SEI induced cyclable lithium loss is also decreased. The optimized cell has a more balanced degradation from both anode and cathode, therefore, the cycle life is improved.

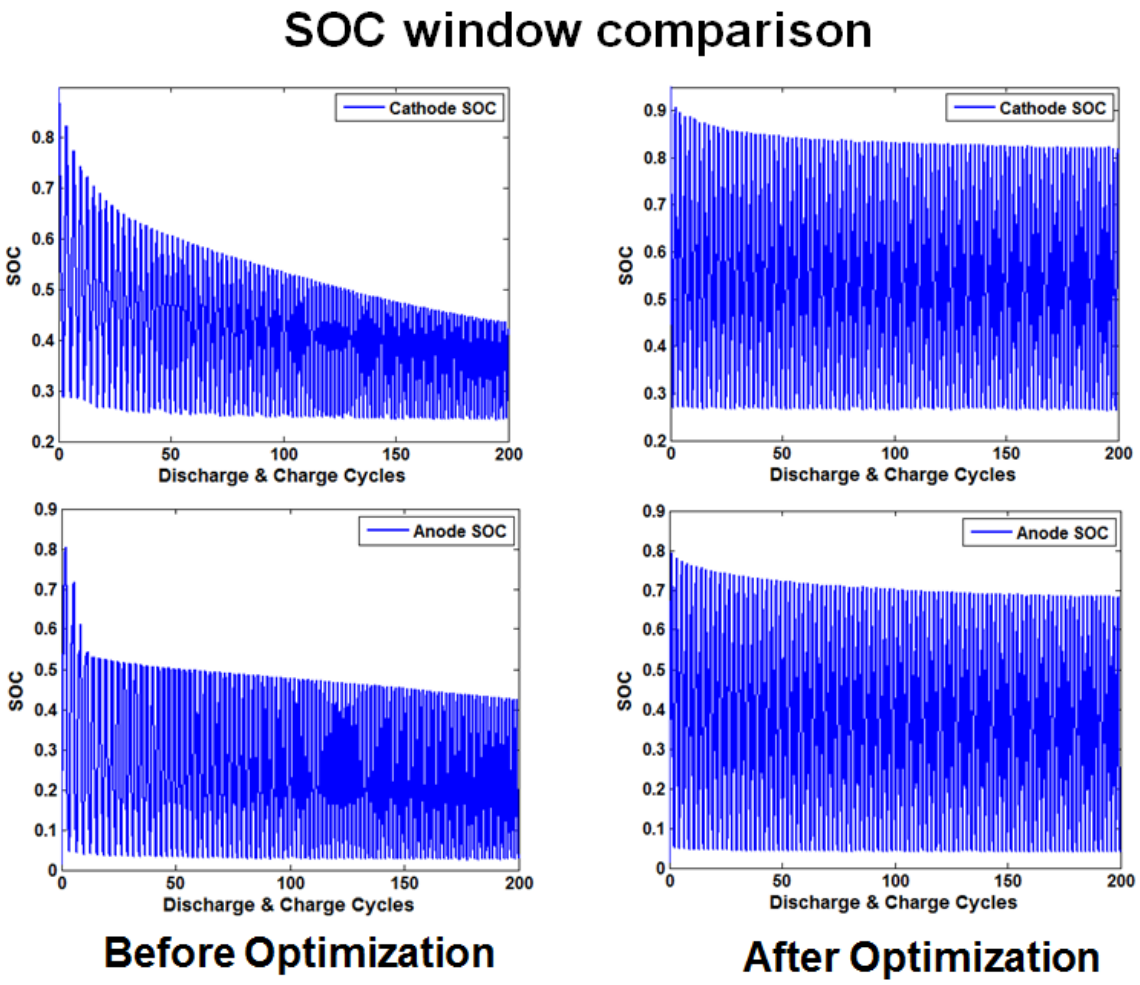

Figure 7.7 SOC swing window comparison between normal cell and optimized cell

The SOC windows changes after optimization indicates the side reaction change on the anode and catode electrode. Figure 7.8 shows the details about the side reaction induced cyclable lithium loss on the anode before and after optimization. The cell before health optimization has

about 50% cyclable lithium loss after 100 cycles, and the optimized cell has only 14% cyclable lithium loss.

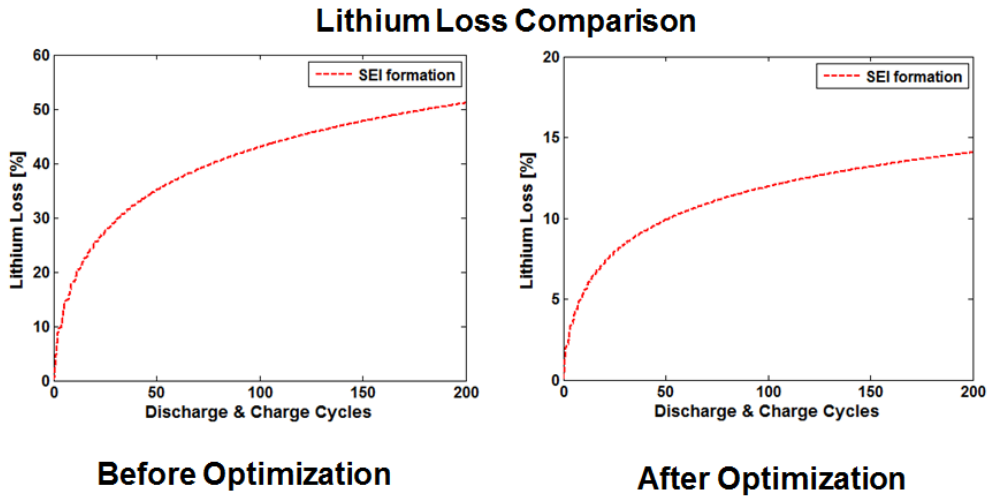

Figure 7.8 Cyclable lithium loss due to SEI and Mn deposition

After health optimization, the battery degradation is significantly reduced. The optimal design parameters are obtained. Particle size plays an important role in the battery degradation. Bigger anode particle size suppresses the SEI growth, and the optimal mass ratio is also found.

7.5 Summary

This chapter developed a general procedure to optimize the battery health while fulfilling the energy and power requirements. The study investigates the impact of battery parameters on the battery performance, such as energy density, power density and battery health. Study shows that energy density and power density optimization doesn't guarantee the battery health. Therefore, for hybrid vehicle application, the energy density, power density, and battery health should be optimized together. Higher energy density and power density require small particle sizes of both anode and cathode; however, battery health needs bigger particle size on anode and a small

particle size on cathode. The gradient based optimization algorithm enables us to optimize the battery parameters to achieve better battery health while still fulfilling the energy and power requirements. After the optimization, battery degradation can be reduced without affecting power and energy density.

Chapter 8
Conclusions and Future Work

In the dissertation, we propose a methodology for power management optimization of hydraulic electric hybrid vehicle. The study demonstrates the benefits of hydraulic hybridization of electric vehicle and its effects on the vehicle range and battery health. After the power management optimization, battery health is identified to be the key issue in the vehicle electrification. Battery degradation is investigated and a comprehensive degradation model is developed. Based on the modeling work, an optimization procedure is developed to improve the battery health. A detailed summary of the dissertation contents is as follows.

8.1 Achievements and Contributions

8.1.1 Hydraulic Electric Hybrid Vehicle Optimization

The all electric range and battery health of the electric vehicle is improved by hydraulic hybridization. A hydraulic electric hybrid vehicle model is developed with the objective to increase the range and protect the battery for improved life. Based on the EV model and Hydraulic Electric Hybrid Vehicle model, an energy management problem was formulated with the objective to lower the energy consumption. As a starting point, a preliminary rule-based (PR) control strategy was proposed based on the analysis of the DC motor efficiency and the battery characteristics. The PR control was a simple and intuitive strategy; nevertheless it enabled

significant improvements of the system efficiency and increased the electric range. A secondary benefit was achieved by reduced battery peak loads and likely extended battery life.

In order to explore the best achievable energy saving, an optimization problem was formed and solved by Dynamic Programming algorithm. Based on the forward simulation results, optimal rules are extracted from the optimal control trajectory. Results show that the additional energy consumption improvement is mainly from the more efficient DC motor operation. Based on this study, the near optimal and vehicle implementable rule-based energy management strategy was developed for the Hydraulic-Electric Hybrid Vehicle. The next challenge will be to implement designed control strategy into the real vehicle, and this effort is underway.

8.1.2 Degradation Analysis Based On Degradation Model

A degradation model was developed by including the key side reactions, and three electrode cell long term cycling was conducted to validate the comprehensive model. Both simulation and experiment show that the capacity degradation process can be divided into three stages: the acceleration stage (SEI growth on anode is dominant), the stabilization stage (SEI slows down, Mn dissolution induced capacity fade is small), and the saturation stage (cathode has poor capacity and becomes the limiting factor). Cracks are suspected to be the main degradation mechanism of Adrich LMO. Anode graphite defoliation was found, which is companied by SEI growth. SEI seems to promote the graphite defoliation. A water-glass model is proposed to explain the overall capacity fade by including different degradation mechanisms. Our study shows that the capacity fade can be divided into three stages: acceleration, stabilization, and saturation. This work provides the experimental evidence for the modeling framework.

8.1.3 Fracture Impact Analysis of Single Cathode Particles

A single-particle model to study the impact of fracture on the capacity fades of cathode electrode. The study investigates the impact of conductivity, SOC swing window, and particle size on the fracture-induced capacity fade. The study suggests that the cathode should be run at a higher SOC level to gain the good conductivity required to suppress the impact of fracture on capacity fade. Particle size is another key factor that affects mass transportation in the particle. Larger particles lead to higher internal resistance for electron transportation; therefore, fracture-induced capacity fade is more severe than with particles of smaller size. Therefore, in order to suppress the impact of fracture, a smaller particle size is preferable. This chapter provides design guidance to the cathode electrode.

8.1.4 Battery capacity fade Optimization Based on Degradation Model

A general procedure to optimize the battery health while fulfilling the energy and power requirements is developed. The study investigates the impact of battery parameters on the battery performance, such as energy density, power density and battery health. Study shows that energy density and power density optimization doesn’t guarantee the battery health. Therefore, for hybrid vehicle application, the energy density, power density, and battery health should be optimized together. Higher energy density and power density require small particle sizes of both anode and cathode; however, battery health needs bigger particle size on anode and a small particle size on cathode. The gradient based optimization algorithm enables us to optimize the battery parameters to achieve better battery health while still fulfilling the energy and power requirements. After the optimization, battery degradation can be reduced without affecting power and energy density.

8.2 Future Work

8.2.1 Degradation model further augment

Degradation is complex process of the lithium ion battery, the degradation in the auto mobile application are taking severe environmental conditions, such as, high temperature, high stress. The degradation patterns under these hassle conditions should also be included in the future study.

8.2.2 Battery management optimization

Battery design optimization provides the best achievable design for the automobile application, however, the power management system is also a key part of the whole system, and will largely affect the battery cycle life. In order to get the best cycle life, the energy management system should also be considered.

Appendices

Appendix A Potential for anode and cathode

The equilibrium potentials for LMO cathode and graphite anode are obtained by C/50 charge and discharge on a 90:5:5 mass ratio anode half-cell and cathode half-cell, respectively, as shown in Fig. A-1. and Fig. A-2. The electrolyte ionic conductivity is shown in Fig. A-3, which is a function of salt concentration.[27]

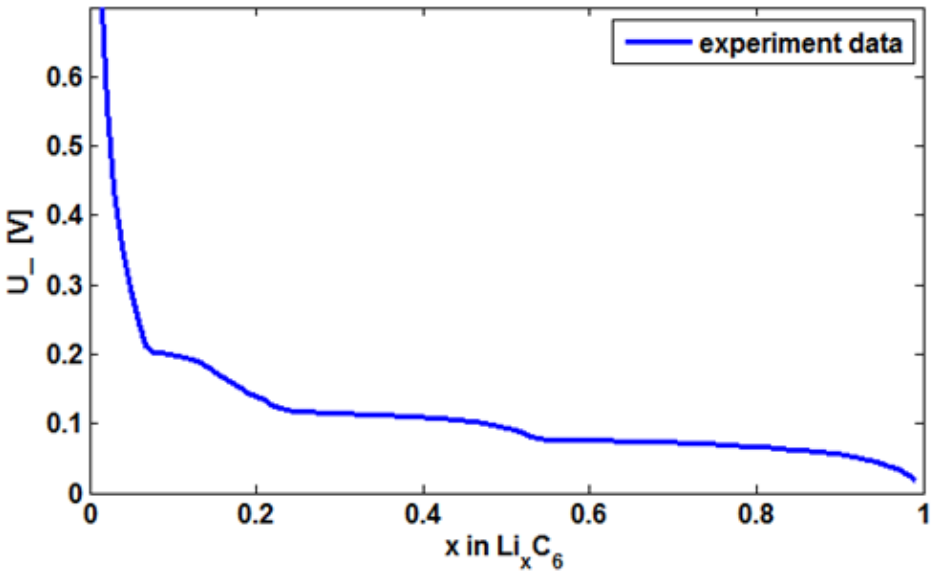

Figure A-1. Equilibrium potential for anode.

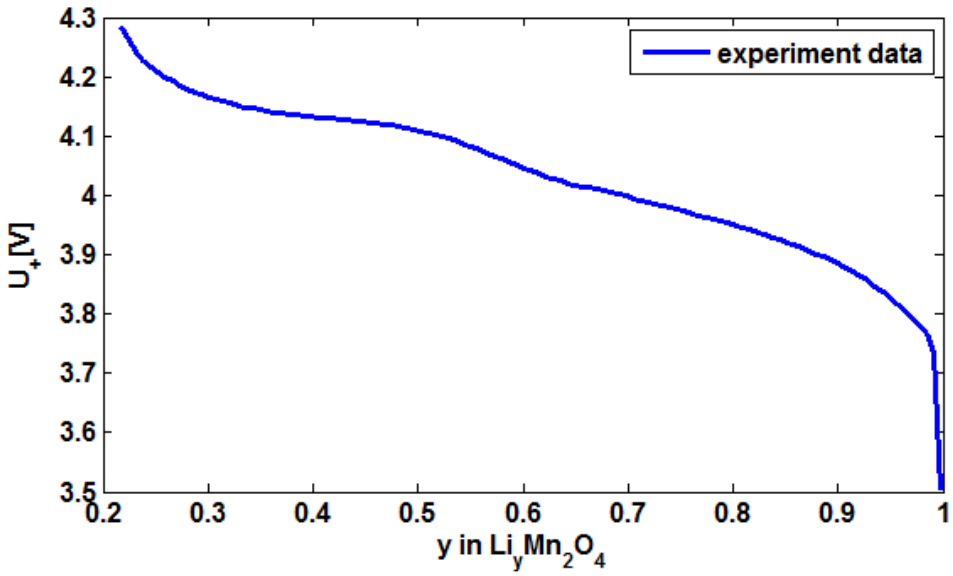

Figure A-2. Equilibrium potential for cathode.

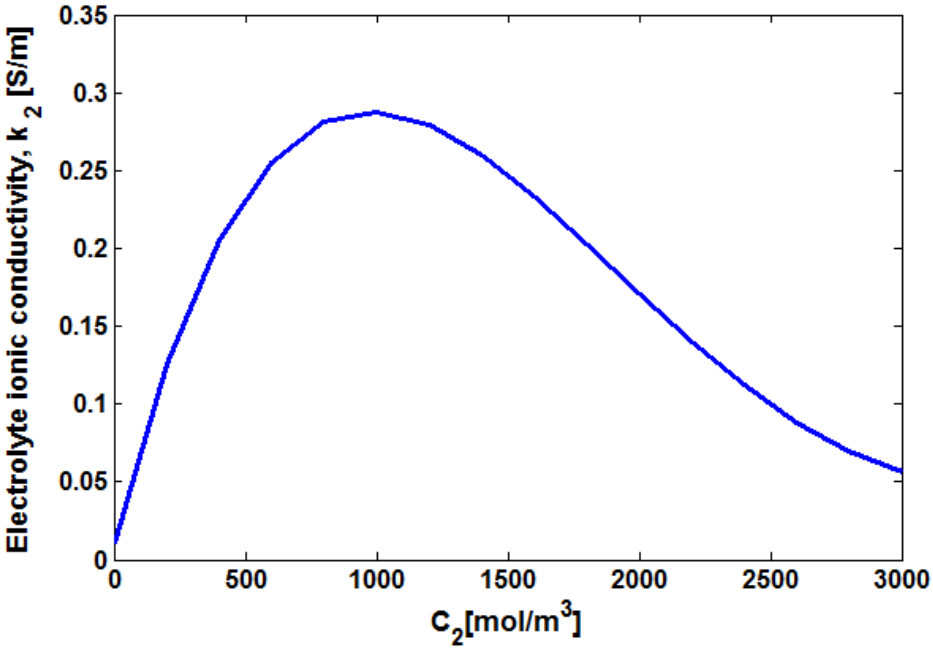

Figure A-3. Electrolyte phase ionic conductivity.

Appendix B Detailed derivation

In the electrolyte, electrochemical potential is the driving force for species flux. The flux of mobile species in the electrolyte can be expressed in the following equations. [138]

$$j_{3,+} = -\frac{v_{3,+}}{vRT}\frac{c_T}{c_0}c_3\nabla\mu_2 + \frac{it_+^0}{z_{3,+}F} + c_{3,+}v_0 \tag{A1}$$

$$j_{3,-} = -\frac{v_{3,-}}{vRT}\frac{c_T}{c_0}c_3\nabla\mu_2 + \frac{it_-^0}{z_{3,-}F} + c_{3,-}v_0 \tag{A2}$$

where $v = v_{3,+} + v_{3,-}$, and $\mu_2 = \mathrm{vRT}\ln(c_3 f_{\pm-} a_{\pm-}^0)$ is the electrochemical potential of the electrolyte.

The relationship between electrolyte potential and current density can be expressed in the following equation. [138]

$$i = -k_3\nabla\phi_3 + k_3\frac{2RT}{c_3F}\left(1 + \frac{d\ln f_\pm}{d\ln c_3}\right)(1 - t_+^0)\nabla c_3 \tag{A3}$$

In order to express species flux densities in terms of concentration gradient and potential gradient, equation A3 is substituted into equation A1 and A2 to read:

$$\begin{aligned} j_{3,+} &= -v_{3,+}D_3\frac{c_T}{c_0}\left(1 + \frac{d\ln f_\pm}{d\ln c_3}\right)\nabla c_{3,+} + \frac{it_+^0}{z_{3,+}F} + c_{3,+}v_0 \\ &= -v_{3,+}D_3\frac{c_T}{c_0}\left(1 + \frac{d\ln f_\pm}{d\ln c_3}\right)\nabla c_{3,+} \\ &+ \frac{2k_3t_-^0t_+^0RT}{c_{3,+}z_{3,+}F^2}\left(1 + \frac{d\ln f_\pm}{d\ln c_3}\right)(1 - t_+^0)\nabla c_{3,+}\frac{k_3t_+^0}{z_{3,+}F}\nabla\phi_3 + c_{3,+}v_0 \\ &= \left[-v_{3,+}D_3\frac{c_T}{c_0} + \frac{2k_3t_-^0t_+^0RT}{c_{3,+}z_{3,+}F^2}\right]\left(1 + \frac{d\ln f_\pm}{d\ln c_3}\right)\nabla c_{3,+} - \frac{k_3t_+^0}{z_{3,+}F}\nabla\phi_3 + c_{3,+}v_0 \end{aligned} \tag{A4}$$

Apply the same procedure to equation.

$$j_{3,-} = \left[-v_{3,-}D_3\frac{c_T}{c_0} + \frac{2k_3 t_-^0 t_-^0 RT}{c_{3,-}z_{3,-}F^2}\right]\left(1 + \frac{d\ln f_{\pm}}{d\ln c_3}\right)\nabla c_{3,-} - \frac{k_3 t_-^0}{z_{3,-}F}\nabla\phi_3 + c_{3,+}v_0 \qquad \text{(A5)}$$

The last term in equation A4 and A5 is negligible when solvent velocity, v_0, is small.

The equilibrium potentials for the LMO cathode is obtained by C/50 charge and discharge on a 90:5:5 mass ratio cathode half-cell as shown in Fig. A-1.

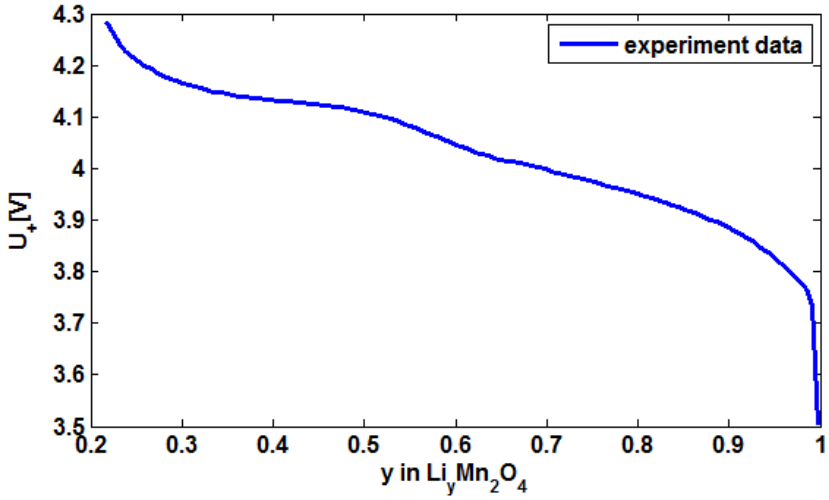

Figure A-1. Equilibrium potential for cathode.

Bibliography

[1] Scrosati, B. and J. Garche, *Lithium batteries: Status, prospects and future.* Journal of Power Sources, 2010. **195**(9): p. 2419-2430.

[2] Boulanger, A.G., et al., *Vehicle electrification: Status and issues.* Proceedings of the IEEE, 2011. **99**(6): p. 1116-1138.

[3] Kahn Ribeiro, S., et al., *Transport and its infrastructure.* Climate change, 2007: p. 323-385.

[4] Agency, I.E., *Energy Technology Perspectives 2012*. 2012.

[5] Forster, P., et al., *Changes in atmospheric constituents and in radiative forcing.* Climate change, 2007. **20**.

[6] EPA, A., *Inventory of US greenhouse gas emissions and sinks: 1990-2011*. 2013, EPA 430-R-13-001.

[7] DeLuchi, M.A., *Emissions of greenhouse gases from the use of transportation fuels and electricity*. 1991, Argonne National Lab., IL (United States). Energy Systems Div.

[8] Franklin, P., et al., *" Xebra Muscle" Making the Xebra Electric Car Go Faster Using Hydraulics.* 2006.

[9] Choi, S.S. and H.S. Lim, *Factors that affect cycle-life and possible degradation mechanisms of a Li-ion cell based on LiCoO< sub> 2</sub>*. Journal of Power Sources, 2002. **111**(1): p. 130-136.

[10] Liu, D. and G. Cao, *Engineering nanostructured electrodes and fabrication of film electrodes for efficient lithium ion intercalation.* Energy & Environmental Science, 2010. **3**(9): p. 1218-1237.

[11] Vetter, J., et al., *Ageing mechanisms in lithium-ion batteries.* Journal of power sources, 2005. **147**(1): p. 269-281.

[12] Arora, P., R.E. White, and M. Doyle, *Capacity Fade Mechanisms and Side Reactions in Lithium‐Ion Batteries.* Journal of The Electrochemical Society, 1998. **145**(10): p. 3647-3667.

[13] Zhang, Q. and R.E. White, *Capacity fade analysis of a lithium ion cell.* Journal of Power Sources, 2008. **179**(2): p. 793-798.

[14] Elbert, P., S. Ebbesen, and L. Guzzella, *Economic Viability of Battery Load-Leveling in Hybrid Electric Vehicles using Supercapacitors.*

[15] Finance, B.N.E., *Global Renewable Energy Market Outlook.* 2011.

[16] Martinot, E., et al., *Renewable energy futures: Targets, scenarios, and pathways.* Annu. Rev. Environ. Resour., 2007. **32**: p. 205-239.

[17] Pourmovahed, A., et al., *Experimental evaluation of hydraulic accumulator efficiency with andwithout elastomeric foam.* Journal of Propulsion and Power, 1988. **4**(2): p. 185-192.

[18] Park, J., B. Raju, and A. Emadi, *Effects of an ultra-capacitor and battery energy storage system in a hybrid electric vehicle.* SAE transactions, 2005. **114**(7): p. 897-904.

[19] Kim, Y.J., *Integrated modeling and hardware-in-the-loop study for systematic evaluation of hydraulic hybrid propulsion options*. 2008: ProQuest.

[20] Agency, E.P., *World's First Full-Size Hydraulic Hybrid SUV Presented at 2004 SAE World Congress.* EPA420-F-04-019, 2004.

[21] Thomas, C., et al., *Correlative Light and Electron Microscopy (CLEM) for Characterization of Lithium Ion Battery Materials.* Microscopy and Microanalysis, 2010. **16**(S2): p. 784-785.

[22] Zhang, X., et al., *Electrochemical performance of spinel LiMn< sub> 2</sub> O< sub> 4</sub> cathode materials made by flame-assisted spray technology.* Journal of Power Sources, 2011. **196**(7): p. 3640-3645.

[23] Liu, Q., et al., *Preparation and Doping Mode of Doped LiMn2O4 for Li-Ion Batteries.* Energies, 2013. **6**(3): p. 1718-1730.

[24] Wohlfahrt-Mehrens, M., *SECONDARY BATTERIES – LITHIUM RECHARGEABLE SYSTEMS – LITHIUM-ION | Positive Electrode: Manganese Spinel Oxides*, in *Encyclopedia of Electrochemical Power Sources*, J. Garche, Editor. 2009, Elsevier: Amsterdam. p. 318-327.

[25] Delhaes, P., *Graphite and precursors*. Vol. 1. 2001: CRC Press.

[26] Doyle, C.M., *Design and simulation of lithium rechargeable batteries*. 1995, Lawrence Berkeley Lab., CA (United States).

[27] Doyle, M., et al., *Comparison of modeling predictions with experimental data from plastic lithium ion cells.* Journal of The Electrochemical Society, 1996. **143**(6): p. 1890-1903.

[28] Du, W., et al., *Energy Density Comparison of Li-ion Cathode Materials Using Dimensional Analysis.* Journal of The Electrochemical Society, 2013. **160**(8): p. A1187-A1193.

[29] Xue, N., et al., *Optimization of a Single Lithium-Ion Battery Cell with a Gradient-Based Algorithm.* Journal of The Electrochemical Society, 2013. **160**(8): p. A1071-A1078.

[30] Smith, K. and C.-Y. Wang, *Power and thermal characterization of a lithium-ion battery pack for hybrid-electric vehicles.* Journal of power sources, 2006. **160**(1): p. 662-673.

[31] Aurbach, D., et al., *Common electroanalytical behavior of Li intercalation processes into graphite and transition metal oxides.* Journal of The Electrochemical Society, 1998. **145**(9): p. 3024-3034.

[32] Aurbach, D., et al., *The Study of Surface Phenomena Related to Electrochemical Lithium Intercalation into Li x MO y Host Materials (M = Ni, Mn).* Journal of The Electrochemical Society, 2000. **147**(4): p. 1322-1331.

[33] Jang, D.H. and S.M. Oh, *Electrolyte Effects on Spinel Dissolution and Cathodic Capacity Losses in 4 V Li/Li x Mn2 O 4 Rechargeable Cells.* Journal of The Electrochemical Society, 1997. **144**(10): p. 3342-3348.

[34] Jang, D.H., Y.J. Shin, and S.M. Oh, *Dissolution of Spinel Oxides and Capacity Losses in 4 V Li / Li x Mn2 O 4 Cells.* Journal of The Electrochemical Society, 1996. **143**(7): p. 2204-2211.

[35] Jang, D.H. and S.M. Oh, *Electrolyte Effects on Spinel Dissolution and Cathodic Capacity Losses in 4 V Li / Li x Mn2 O 4 Rechargeable Cells.* Journal of The Electrochemical Society, 1997. **144**(10): p. 3342-3348.

[36] Park, J., et al., *Numerical Simulation of the Effect of the Dissolution of LiMn2O4 Particles on Li-Ion Battery Performance.* Electrochemical and Solid-State Letters, 2011. **14**(2): p. A14-A18.

[37] Lu, C.-H. and S.-W. Lin, *Dissolution kinetics of spinel lithium manganate and its relation to capacity fading in lithium ion batteries.* Journal of materials research, 2002. **17**(6): p. 1476-1481.

[38] Dai, Y., L. Cai, and R.E. White, *Capacity Fade Model for Spinel LiMn2O4 Electrode.* Journal of The Electrochemical Society, 2013. **160**(1): p. A182-A190.

[39] Xia, Y., Y. Zhou, and M. Yoshio, *Capacity Fading on Cycling of 4 V Li / LiMn2 O 4 Cells.* Journal of The Electrochemical Society, 1997. **144**(8): p. 2593-2600.

[40] Komaba, S., et al., *Inorganic electrolyte additives to suppress the degradation of graphite anodes by dissolved Mn (II) for lithium-ion batteries.* Journal of power sources, 2003. **119**: p. 378-382.

[41] Blyr, A., et al., *Self - Discharge of LiMn2 O 4/C Li - Ion Cells in Their Discharged State: Understanding by Means of Three - Electrode Measurements.* Journal of The Electrochemical Society, 1998. **145**(1): p. 194-209.

[42] Wang, D., et al., *Cracking causing cyclic instability of LiFePO< sub> 4</sub> cathode material.* Journal of Power Sources, 2005. **140**(1): p. 125-128.

[43] Lim, M.-R., W.-I. Cho, and K.-B. Kim, *Preparation and characterization of gold-codeposited LiMn< sub> 2</sub> O< sub> 4</sub> electrodes.* Journal of power sources, 2001. **92**(1): p. 168-176.

[44] Wang, H., et al., *TEM Study of Electrochemical Cycling‐Induced Damage and Disorder in LiCoO2 Cathodes for Rechargeable Lithium Batteries.* Journal of The Electrochemical Society, 1999. **146**(2): p. 473-480.

[45] Christensen, J. and J. Newman, *A Mathematical Model of Stress Generation and Fracture in Lithium Manganese Oxide.* Journal of The Electrochemical Society, 2006. **153**(6): p. A1019-A1030.

[46] Fong, R., U. von Sacken, and J.R. Dahn, *Studies of Lithium Intercalation into Carbons Using Nonaqueous Electrochemical Cells.* Journal of The Electrochemical Society, 1990. **137**(7): p. 2009-2013.

[47] Kim, S.-P., A.C.v. Duin, and V.B. Shenoy, *Effect of electrolytes on the structure and evolution of the solid electrolyte interphase (SEI) in Li-ion batteries: A molecular dynamics study.* Journal of Power Sources, 2011. **196**(20): p. 8590-8597.

[48] Zhang, H.-L., et al., *New insight into the solid electrolyte interphase with use of a focused ion beam.* The Journal of Physical Chemistry B, 2005. **109**(47): p. 22205-22211.

[49] Edström, K., M. Herstedt, and D.P. Abraham, *A new look at the solid electrolyte interphase on graphite anodes in Li-ion batteries.* Journal of Power Sources, 2006. **153**(2): p. 380-384.

[50] Arora, P., M. Doyle, and R.E. White, *Mathematical Modeling of the Lithium Deposition Overcharge Reaction in Lithium‐Ion Batteries Using Carbon‐Based Negative Electrodes.* Journal of The Electrochemical Society, 1999. **146**(10): p. 3543-3553.

[51] Harris, S.J., et al., *Direct< i> in situ</i> measurements of Li transport in Li-ion battery negative electrodes.* Chemical Physics Letters, 2010. **485**(4): p. 265-274.

[52] Dey, A. and B. Sullivan, *The electrochemical decomposition of propylene carbonate on graphite.* Journal of The Electrochemical Society, 1970. **117**(2): p. 222-224.

[53] Tsujikawa, T., et al., *A Study on the Cause of Deterioration in Float-Charged Lithium-Ion Batteries Using LiMn2O4 as a Cathode Active Material.* Journal of The Electrochemical Society, 2011. **158**(3): p. A322-A325.

[54] Xiao, X., et al., *Atomic Layer Coating to Mitigate Capacity Fading Associated with Manganese Dissolution in Lithium Ion Batteries.* Electrochemistry Communications, 2013.

[55] Komaba, S., N. Kumagai, and Y. Kataoka, *Influence of manganese (II), cobalt (II), and nickel (II) additives in electrolyte on performance of graphite anode for lithium-ion batteries.* Electrochimica acta, 2002. **47**(8): p. 1229-1239.

[56] Collia, D.V., J. Sharp, and L. Giesbrecht, *The 2001 national household travel survey: A look into the travel patterns of older Americans.* Journal of Safety Research, 2003. **34**(4): p. 461-470.

[57] Schafer, A. and D.G. Victor, *The future mobility of the world population.* Transportation Research Part A: Policy and Practice, 2000. **34**(3): p. 171-205.

[58] Filipi, Z., et al., *Combined optimisation of design and power management of the hydraulic hybrid propulsion system for the 6× 6 medium truck.* International Journal of Heavy Vehicle Systems, 2004. **11**(3): p. 372-402.

[59] Kim, Y.J. and Z. Filipi, *Simulation study of a series hydraulic hybrid propulsion system for a light truck.* Training, 2007. **2008**: p. 12-10.

[60] Woon, M., et al., *Energy management options for an electric vehicle with hydraulic regeneration system.* Fuel, 2011. **2015**: p. 06-22.

[61] Pourmovahed, A., N. Beachley, and F. Fronczak, *Modeling of a Hydraulic Energy Regeneration System: Part I—Analytical Treatment.* Journal of dynamic systems, measurement, and control, 1992. **114**(1): p. 155-159.

[62] Doerffel, D. and S.A. Sharkh, *A critical review of using the Peukert equation for determining the remaining capacity of lead-acid and lithium-ion batteries.* Journal of Power Sources, 2006. **155**(2): p. 395-400.

[63] Ceraolo, M., *New dynamical models of lead-acid batteries.* Power Systems, IEEE Transactions on, 2000. **15**(4): p. 1184-1190.

[64] Caumont, O., et al., *Energy gauge for lead-acid batteries in electric vehicles.* Energy Conversion, IEEE Transactions on, 2000. **15**(3): p. 354-360.

[65] Drouilhet, S. and B.L. Johnson. *A battery life prediction method for hybrid power applications*. in *AIAA Aerospace Sciences Meeting and Exhibit*. 1997.

[66] Culpin, B. and D. Rand, *Failure modes of lead/acid batteries.* Journal of power sources, 1991. **36**(4): p. 415-438.

[67] Lin, C.-C., et al. *Energy management strategy for a parallel hybrid electric truck*. in *American Control Conference, 2001. Proceedings of the 2001*. 2001. IEEE.

[68] Lin, C.-C., H. Peng, and J. Grizzle. *A stochastic control strategy for hybrid electric vehicles*. in *American Control Conference, 2004. Proceedings of the 2004*. 2004. IEEE.

[69] Sundstrom, O. and L. Guzzella. *A generic dynamic programming Matlab function*. in *Control Applications,(CCA) & Intelligent Control,(ISIC), 2009 IEEE*. 2009. IEEE.

[70] Alson, J., et al., *Progress report on clean and efficient automotive technologies under development at EPA.* United States Environmental Protection Agency, EPA420, 2004.

[71] Narayanrao, R., M. Joglekar, and S. Inguva, *A Phenomenological Degradation Model for Cyclic Aging of Lithium Ion Cell Materials.* Journal of The Electrochemical Society, 2013. **160**(1): p. A125-A137.

[72] Ning, G., B. Haran, and B.N. Popov, *Capacity fade study of lithium-ion batteries cycled at high discharge rates.* Journal of Power Sources, 2003. **117**(1): p. 160-169.

[73] Honkura, K., K. Takahashi, and T. Horiba, *Capacity-fading prediction of lithium-ion batteries based on discharge curves analysis.* Journal of Power Sources, 2011. **196**(23): p. 10141-10147.

[74] Smith, A., J. Burns, and J. Dahn, *A high precision study of the Coulombic efficiency of Li-ion batteries.* Electrochemical and Solid-State Letters, 2010. **13**(12): p. A177-A179.

[75] Shim, J. and K.A. Striebel, *Effect of electrode density on cycle performance and irreversible capacity loss for natural graphite anode in lithium-ion batteries.* Journal of power sources, 2003. **119**: p. 934-937.

[76] Yuqin, C., et al., *Irreversible capacity loss of graphite electrode in lithium-ion batteries.* Journal of power sources, 1997. **68**(2): p. 187-190.

[77] Nadimpalli, S.P., et al., *Quantifying capacity loss due to solid-electrolyte-interphase layer formation on silicon negative electrodes in lithium-ion batteries.* Journal of Power Sources, 2012. **215**: p. 145-151.

[78] Spotnitz, R., *Simulation of capacity fade in lithium-ion batteries.* Journal of Power Sources, 2003. **113**(1): p. 72-80.

[79] Ramasamy, R.P., J.-W. Lee, and B.N. Popov, *Simulation of capacity loss in carbon electrode for lithium-ion cells during storage.* Journal of power sources, 2007. **166**(1): p. 266-272.

[80] Nakagawa, Y., et al., *Study on irreversible capacity loss in lithium ion rechargeable batteries.* Synthetic metals, 1997. **85**(1): p. 1343-1344.

[81] Ramadass, P., et al., *Capacity fade of Sony 18650 cells cycled at elevated temperatures: Part II. Capacity fade analysis.* Journal of Power Sources, 2002. **112**(2): p. 614-620.

[82] Safari, M., et al., *Multimodal physics-based aging model for life prediction of Li-ion batteries.* Journal of The Electrochemical Society, 2009. **156**(3): p. A145-A153.

[83] Smith, K. and C.-Y. Wang, *Solid-state diffusion limitations on pulse operation of a lithium ion cell for hybrid electric vehicles.* Journal of power sources, 2006. **161**(1): p. 628-639.

[84] Dolle, M., et al., *In situ TEM study of the interface carbon/electrolyte.* Journal of power sources, 2001. **97**: p. 104-106.

[85] Levi, M.D. and D. Aurbach, *The mechanism of lithium intercalation in graphite film electrodes in aprotic media. Part 1. High resolution slow scan rate cyclic voltammetric studies and modeling.* Journal of Electroanalytical Chemistry, 1997. **421**(1): p. 79-88.

[86] Colclasure, A.M., K.A. Smith, and R.J. Kee, *Modeling detailed chemistry and transport for solid-electrolyte-interface (SEI) films in Li–ion batteries.* Electrochimica Acta, 2011. **58**: p. 33-43.

[87] McArthur, M., S. Trussler, and J. Dahn, *In Situ Investigations of SEI Layer Growth on Electrode Materials for Lithium-Ion Batteries Using Spectroscopic Ellipsometry.* Journal of The Electrochemical Society, 2012. **159**(3): p. A198-A207.

[88] Aurbach, D., et al., *A short review of failure mechanisms of lithium metal and lithiated graphite anodes in liquid electrolyte solutions.* Solid State Ionics, 2002. **148**(3): p. 405-416.

[89] Zhang, S., K. Xu, and T. Jow, *EIS study on the formation of solid electrolyte interface in Li-ion battery.* Electrochimica acta, 2006. **51**(8): p. 1636-1640.

[90] Smith, A., et al., *Interpreting High Precision Coulometry Results on Li-ion Cells.* Journal of The Electrochemical Society, 2011. **158**(10): p. A1136-A1142.

[91] Smith, A., J. Burns, and J. Dahn, *High-Precision Differential Capacity Analysis of LiMn2O4/graphite Cells.* Electrochemical and Solid-State Letters, 2011. **14**(4): p. A39-A41.

[92] Aurbach, D., et al., *The Correlation Between the Surface Chemistry and the Performance of Li‐Carbon Intercalation Anodes for Rechargeable ‘Rocking‐Chair’ Type Batteries.* Journal of The Electrochemical Society, 1994. **141**(3): p. 603-611.

[93] Yang, C., Y. Wang, and C. Wan, *Composition analysis of the passive film on the carbon electrode of a lithium-ion battery with an EC-based electrolyte.* Journal of power sources, 1998. **72**(1): p. 66-70.

[94] Wang, Y., et al., *Theoretical studies to understand surface chemistry on carbon anodes for lithium-ion batteries: Reduction mechanisms of ethylene carbonate.* Journal of the American Chemical Society, 2001. **123**(47): p. 11708-11718.

[95] Legrand, N., et al., *Physical characterization of the charging process of a Li-ion battery and prediction of Li plating by electrochemical modelling.* Journal of Power Sources, 2014. **245**: p. 208-216.

[96] Aurbach, D., et al., *Recent studies on the correlation between surface chemistry, morphology, three-dimensional structures and performance of Li and Li-C intercalation anodes in several important electrolyte systems.* Journal of power sources, 1997. **68**(1): p. 91-98.

[97] Zhang, S., K. Xu, and T. Jow, *Study of the charging process of a LiCoO< sub> 2</sub>-based Li-ion battery.* Journal of power sources, 2006. **160**(2): p. 1349-1354.

[98] Zhang, S.S., *The effect of the charging protocol on the cycle life of a Li-ion battery.* Journal of power sources, 2006. **161**(2): p. 1385-1391.

[99] Choa, J. and M.M. Thackeray, *Structural Changes of LiMn2 O 4 Spinel Electrodes during Electrochemical Cycling.* Journal of The Electrochemical Society, 1999. **146**(10): p. 3577-3581.

[100] Choi, N.-S., et al., *Degradation of spinel lithium manganese oxides by low oxidation durability of LiPF6-based electrolyte at 60 ℃.* Solid State Ionics, 2012. **219**(0): p. 41-48.

[101] Kawamura, T., S. Okada, and J.-i. Yamaki, *Decomposition reaction of LiPF< sub> 6</sub>-based electrolytes for lithium ion cells.* Journal of power sources, 2006. **156**(2): p. 547-554.

[102] Aifantis, K. and J. Dempsey, *Stable crack growth in nanostructured Li-batteries.* Journal of power sources, 2005. **143**(1): p. 203-211.

[103] Christensen, J. and J. Newman, *Stress generation and fracture in lithium insertion materials.* Journal of Solid State Electrochemistry, 2006. **10**(5): p. 293-319.

[104] Wang, E., et al., *Stability of Lithium Ion Spinel Cells. III. Improved Life of Charged Cells.* Journal of The Electrochemical Society, 2000. **147**(11): p. 4023-4028.

[105] Guyomard, D. and J.M. Tarascon, *Rechargeable Li1 + x Mn2 O 4 / Carbon Cells with a New Electrolyte Composition: Potentiostatic Studies and Application to Practical Cells.* Journal of The Electrochemical Society, 1993. **140**(11): p. 3071-3081.

[106] Kerlau, M., J.A. Reimer, and E.J. Cairns, *Investigation of particle isolation in Li-ion battery electrodes using< sup> 7</sup> Li NMR spectroscopy.* Electrochemistry communications, 2005. **7**(12): p. 1249-1251.

[107] Cai, L. and R.E. White, *Mathematical modeling of a lithium ion battery with thermal effects in COMSOL Inc. Multiphysics (MP) software.* Journal of Power Sources, 2011. **196**(14): p. 5985-5989.

[108] Shim, J., et al., *Electrochemical analysis for cycle performance and capacity fading of a lithium-ion battery cycled at elevated temperature.* Journal of power sources, 2002. **112**(1): p. 222-230.

[109] Zhang, D., et al., *Studies on capacity fade of lithium-ion batteries.* Journal of Power Sources, 2000. **91**(2): p. 122-129.

[110] Xia, Y., Y. Zhou, and M. Yoshio, *Capacity Fading on Cycling of 4 V Li/LiMn2 O 4 Cells.* Journal of The Electrochemical Society, 1997. **144**(8): p. 2593-2600.

[111] Peterson, S.B., J. Apt, and J. Whitacre, *Lithium-ion battery cell degradation resulting from realistic vehicle and vehicle-to-grid utilization.* Journal of Power Sources, 2010. **195**(8): p. 2385-2392.

[112] Aurbach, D., et al., *An analysis of rechargeable lithium-ion batteries after prolonged cycling.* Electrochimica Acta, 2002. **47**(12): p. 1899-1911.

[113] Zhao, K., et al., *Fracture of electrodes in lithium-ion batteries caused by fast charging.* Journal of Applied Physics, 2010. **108**(7): p. 073517-073517-6.

[114] Broussely, M., et al., *Main aging mechanisms in Li ion batteries.* Journal of Power Sources, 2005. **146**(1): p. 90-96.

[115] Amatucci, G.G., et al., *Failure Mechanism and Improvement of the Elevated Temperature Cycling of LiMn2 O 4 Compounds Through the Use of the LiAl x Mn2− x O 4− z F z Solid Solution.* Journal of The Electrochemical Society, 2001. **148**(2): p. A171-A182.

[116] Smith, A., et al., *A high precision coulometry study of the SEI growth in Li/graphite cells.* Journal of The Electrochemical Society, 2011. **158**(5): p. A447-A452.

[117] Di Domenico, D., A. Stefanopoulou, and G. Fiengo, *Lithium-ion battery state of charge and critical surface charge estimation using an electrochemical model-based extended Kalman filter.* Journal of dynamic systems, measurement, and control, 2010. **132**(6).

[118] Schlesinger, M. and M. Paunovic, *Modern electroplating*. Vol. 55. 2011: Wiley.

[119] Andricacos, P.C., et al., *Damascene copper electroplating for chip interconnections.* IBM Journal of Research and Development, 1998. **42**(5): p. 567-574.

[120] Surman, S., et al., *Comparison of microscope techniques for the examination of biofilms.* Journal of Microbiological Methods, 1996. **25**(1): p. 57-70.

[121] Yazami, R., *Surface chemistry and lithium storage capability of the graphite–lithium electrode.* Electrochimica acta, 1999. **45**(1): p. 87-97.

[122] Kong, F., et al., *In situ studies of SEI formation.* Journal of power sources, 2001. **97**: p. 58-66.

[123] Chung, G.C., et al., *Origin of Graphite Exfoliation An Investigation of the Important Role of Solvent Cointercalation.* Journal of The Electrochemical Society, 2000. **147**(12): p. 4391-4398.

[124] Spahr, M.E., et al., *Exfoliation of graphite during electrochemical lithium insertion in ethylene carbonate-containing electrolytes.* Journal of the Electrochemical Society, 2004. **151**(9): p. A1383-A1395.

[125] Inaba, M., et al., *STM study on graphite/electrolyte interface in lithium-ion batteries: solid electrolyte interface formation in trifluoropropylene carbonate solution.* Electrochimica acta, 1999. **45**(1): p. 99-105.

[126] Zhang, X., W. Shyy, and A.M. Sastry, *Numerical simulation of intercalation-induced stress in Li-ion battery electrode particles.* Journal of the Electrochemical Society, 2007. **154**(10): p. A910-A916.

[127] Amatucci, G., et al., *Materials' effects on the elevated and room temperature performance of CLiMn2O4 Li-ion batteries.* Journal of power sources, 1997. **69**(1): p. 11-25.

[128] David, W.I.F., et al., *Structure refinement of the spinel-related phases Li2Mn2O4 and Li0.2Mn2O4.* Journal of Solid State Chemistry, 1987. **67**(2): p. 316-323.

[129] Prussin, S., *Generation and distribution of dislocations by solute diffusion.* Journal of Applied Physics, 1961. **32**(10): p. 1876-1881.

[130] Timoshenko, S. and J. Goodier, *1970, Theory of Elasticity, McGraw-Hill, New York.*

[131] Yang, F., *Interaction between diffusion and chemical stresses.* Materials Science and Engineering: A, 2005. **409**(1): p. 153-159.

[132] Noda, N., R.B. Hetnarski, and Y. Tanigawa, *Thermal stresses*. 2003: Taylor & Francis.

[133] Zhang, X., A.M. Sastry, and W. Shyy, *Intercalation-induced stress and heat generation within single lithium-ion battery cathode particles.* Journal of The Electrochemical Society, 2008. **155**(7): p. A542-A552.

[134] Li, J., et al., *Crack pattern formation in thin film lithium-ion battery electrodes.* Journal of The Electrochemical Society, 2011. **158**(6): p. A689-A694.

[135] Zhu, M., J. Park, and A.M. Sastry, *Fracture Analysis of the Cathode in Li-Ion Batteries: A Simulation Study.* Journal of The Electrochemical Society, 2012. **159**(4): p. A492-A498.

[136] Less, G., et al., *Micro-scale modeling of Li-ion batteries: parameterization and validation.* Journal of The Electrochemical Society, 2012. **159**(6): p. A697-A704.

[137] Yamamura, S., et al., *In situ conductivity measurements of LiMn2O4 thin films during lithium insertion/extraction by using interdigitated microarray electrodes.* Journal of Solid State Electrochemistry, 1998. **2**(4): p. 211-215.

[138] Newman, J. and K.E. Thomas-Alyea, *Electrochemical systems*. 2012: John Wiley & Sons.

[139] Wang, C.-W. and A.M. Sastry, *Mesoscale modeling of a Li-ion polymer cell.* Journal of The Electrochemical Society, 2007. **154**(11): p. A1035-A1047.

[140] Marinho, B., et al., *Electrical conductivity of compacts of graphene, multi-wall carbon nanotubes, carbon black, and graphite powder.* Powder Technology, 2012. **221**: p. 351-358.

[141] Cho, J. and B. Park, *Preparation and electrochemical/thermal properties of LiNi< sub> 0.74</sub> Co< sub> 0.26</sub> O< sub> 2</sub> cathode material.* Journal of power sources, 2001. **92**(1): p. 35-39.

[142] Vallée, A., S. Besner, and J. Prud'Homme, *Comparative study of poly (ethylene oxide) electrolytes made with LiN (CF3SO2) 2, LiCF3SO3 and LiClO4: Thermal properties and conductivity behaviour.* Electrochimica acta, 1992. **37**(9): p. 1579-1583.

[143] Pesaran, A.A., et al., *Battery Requirements for Plug-in Hybrid Electric Vehicles--analysis and Rationale*. 2009: National Renewable Energy Laboratory.

[144] Axsen, J., A. Burke, and K.S. Kurani, *Batteries for plug-in hybrid electric Vehicles (PHEVs): goals and the state of technology circa 2008.* 2008.

[145] Liaw, B.Y. and M. Dubarry, *From driving cycle analysis to understanding battery performance in real-life electric hybrid vehicle operation.* Journal of power sources, 2007. **174**(1): p. 76-88.

[146] Wirasingha, S.G., N. Schofield, and A. Emadi. *Plug-in hybrid electric vehicle developments in the US: Trends, barriers, and economic feasibility*. in *Vehicle Power and Propulsion Conference, 2008. VPPC'08. IEEE*. 2008. IEEE.

[147] Rao, R. and S. Vrudhula. *Battery optimization vs energy optimization: Which to choose and when?* in *Computer-Aided Design, 2005. ICCAD-2005. IEEE/ACM International Conference on*. 2005. IEEE.

[148] Fuller, T.F., M. Doyle, and J. Newman, *Simulation and optimization of the dual lithium ion insertion cell.* Journal of the Electrochemical Society, 1994. **141**(1): p. 1-10.

[149] Sumitava, D., et al., *Model-based simultaneous optimization of multiple design parameters for lithium-ion batteries for maximization of energy density.* Journal of Power Sources, 2012.

[150] Moura, S.J., J.L. Stein, and H.K. Fathy, *Battery health-conscious power management for plug-in hybrid electric vehicles via stochastic control.* Proc. ASME Dyn. Syst. Control Conf, 2010: p. 1-2.

[151] Moura, S.J., J.L. Stein, and H.K. Fathy, *Battery-Health Conscious Power Managementin Plug-In Hybrid Electric Vehicles via Electrochemical Modeling and Stochastic Control.* 2012.

[152] Moura, S., et al., *Optimal Control of Film Growth in Lithium-Ion Battery Packs via Relay Switches.* Industrial Electronics, IEEE Transactions on, 2009(99): p. 1-1.

[153] Newman, J., *Optimization of Porosity and Thickness of a Battery Electrode by Means of a Reaction‐Zone Model.* Journal of the Electrochemical Society, 1995. **142**(1): p. 97-101.

[154] Ramadesigan, V., et al., *Optimal porosity distribution for minimized ohmic drop across a porous electrode.* Journal of The Electrochemical Society, 2010. **157**(12): p. A1328-A1334.

[155] Srinivasan, V. and J. Newman, *Design and optimization of a natural graphite/iron phosphate lithium-ion cell.* Journal of the Electrochemical Society, 2004. **151**(10): p. A1530-A1538.

[156] Christensen, J., V. Srinivasan, and J. Newman, *Optimization of lithium titanate electrodes for high-power cells.* Journal of The Electrochemical Society, 2006. **153**(3): p. A560-A565.

[157] Stewart, S., et al., *Optimizing the performance of lithium titanate spinel paired with activated carbon or iron phosphate.* Journal of The Electrochemical Society, 2008. **155**(3): p. A253-A261.

[158] Kiwiel, K.C., *Convergence and efficiency of subgradient methods for quasiconvex minimization.* Mathematical programming, 2001. **90**(1): p. 1-25.

[159] Boyd, S.P. and L. Vandenberghe, *Convex optimization*. 2004: Cambridge university press.

[160] Xue, N., et al., *Design of a lithium-ion battery pack for PHEV using a hybrid optimization method.* Applied Energy, 2014. **115**: p. 591-602.

[161] Horiba, T., et al., *Manganese type lithium ion battery for pure and hybrid electric vehicles.* Journal of power sources, 2001. **97**: p. 719-721.

[162] Howard, W.F. and R.M. Spotnitz, *Theoretical evaluation of high-energy lithium metal phosphate cathode materials in Li-ion batteries.* Journal of Power Sources, 2007. **165**(2): p. 887-891.